NASA Contractor Report 177946

NASA-CR-177946
19860006863

Study on Effects of Powder and Flake Chemistry and Morphology on the Properties of Al-Cu-Mg-X-X-X Powder Metallurgy Advanced Aluminum Alloys

P. J. Meschter, R. J. Lederich, J. E. O'Neal, and P. S. Pao

McDonnell Douglas Research Laboratories
St. Louis, Missouri

Contract NAS1-17107
November 1985

National Aeronautics and
Space Administration

Langley Research Center
Hampton, Virginia 23665

NASA Contractor Report 177946

Study on Effects of Powder and Flake Chemistry and Morphology on the Properties of Al-Cu-Mg-X-X-X Powder Metallurgy Advanced Aluminum Alloys

P. J. Meschter, R. J. Lederich, J. E. O'Neal, and P. S. Pao

McDonnell Douglas Research Laboratories
St. Louis, Missouri

Contract NAS1-17107
November 1985

National Aeronautics and
Space Administration

Langley Research Center
Hampton, Virginia 23665

PREFACE

This report presents the results of research performed from 21 September 1982 through 20 June 1984 by the McDonnell Douglas Research Laboratories under the National Aeronautics and Space Administration Contract NAS1-17107 entitled "Study of Effects of Powder and Flake Chemistry and Morphology on the Properties of Al-Cu-Mg-X-X-X Powder Metallurgy Advanced Aluminum Alloys." The objectives were to (1) investigate systematically the effects of alloy chemistry and control, and particulate morphology on the resultant consolidated product properties for the Al-Cu-Mg-X-X-X alloy family, and (2) to identify the principal contributing chemical/metallurgical/processing factors which affect each property of interest. The results provide a better fundamental understanding of the processing-structure-property relationships for this alloy class and a start for defining the degree of process control necessary to accomplish commercialization.

The research was performed in the Solid State Sciences Department, managed by Dr. C. R. Whitsett. The principal investigator was Dr. P. J. Meschter; co-investigators were Dr. P. S. Pao, Mr. J. E. O'Neal, and Mr. R. J. Lederich. The technical manager was Mr. W. Barry Lisagor, NASA, Langley Research Center.

This Page Intentionally Left Blank

CONTENTS

CONTENTS (Continued)

LIST OF ILLUSTRATIONS

LIST OF TABLES

1. INTRODUCTION

Recent research and development of wrought aluminum alloys through rapid solidification and powder-metallurgical (P/M) processing has shown that significant improvements in properties, relative to those of conventionally formed alloys, can be expected, particularly in alloys with novel compositions. Rapid solidification processing (RSP) of aluminum alloys has thus far been concerned with the development and screening of candidate alloy compositions. The effects of powder and flake chemistry, morphology, and metallurgical condition on the properties of consolidated alloys have not been adequately studied. Particulate cooling rate and shape, oxide film formation and breakup, phase relationships, and recrystallization and texturing all potentially affect final properties. These parameters must be systematically investigated to identify the extent of process control necessary to achieve commercialization and full exploitation of this promising new class of aluminum alloys.

2. RESEARCH OBJECTIVES AND APPROACH

This study is a systematic investigation of the effects of alloy chemistry and particulate morphology on consolidation behavior and consolidated product properties for the Al-Cu-Mg-X-X-X alloy family. The overall goal is to develop alloy chemistry design methods, particulate production methods, consolidation methods, and heat-treatment sequences so that rapid solidification processed (RSP) aluminum alloys in this class might realize their potential for room-temperature and elevated-temperature applications.

2.1 Objectives

1. Systematically investigate the effects of alloy chemistry in non-Li- and Li-containing Al-Cu-Mg-X-X-X alloys on the properties of heat-treated extrusions and forgings. Emphasis was placed on Al-3Li-1.5Cu-1Mg-0.5Co-0.2Zr for improved ambient-temperature properties, and on dispersoid-forming element additions to Al-4.4Cu-1.5Mg for improved properties to 150°C (300°F).

2. Systematically investigate the effects of particulate morphology and cooling rate on consolidated product microstructures and properties of Al-Cu-Mg-X-X-X alloys. The emphasis was on property differences between powder extrusions and forgings, between extrusions consolidated from powders and from flakes, and among extrusions consolidated from particulates solidified at different rates.

3. Identify contributing chemical, metallurgical, and processing factors that affect various properties of interest, e.g., the degree of improvement in 150°C properties of a dispersoid-containing RSP alloy compared with commercial 2024-Al, or the effect of Li and Co additions on the balance between room-temperature strength and ductility in an Al-Cu-Mg alloy.

4. Develop criteria for the design of chemistry/particulate-morphology/consolidation/heat-treatment combinations to enable powder-processed aluminum alloys to compete with commercial Al alloys in room-temperature applications and with titanium alloys in 150°C applications.

The contract was divided into four tasks, as follows:

Task 1: Preparation and Characterization of Rapidly Solidified Al-Cu-Mg-X-X-X Powder and Flakes;

Task 2: Consolidation and Post-Consolidation Processing of Particulates;

Task 3: Microstructure and Properties of Consolidated Forms; and

Task 4: Correlation of Process/Structure/Properties Relations.

2.2 Selection of Alloy Compositions

Two alloy types were chosen: an Al-Cu-Mg alloy modified by Fe and Ni additions for application to 150°C, and an Al-Li-Cu-Mg alloy intended primarily for ambient-temperature applications. An applications study **(1)** has shown that an advanced aluminum alloy must have a tensile strength of 480 MPa (70 ksi) at 150°C to match the specific strength of Ti-6Al-4V. If aluminum alloys can reach strength equivalency with titanium alloys at this temperature, their lower cost will encourage substitution in structural applications. The key to 150°C strength improvement in aluminum alloys lies in the introduction of significant volume fractions of thermally stable, incoherent dispersoids. Since RSP imposes microstructural refinement, wrought parts made from RSP powders can have finer dispersoids than equivalent ingot-metallurgical (I/M) alloy parts. Fine, closely spaced dispersoids interfere with dislocation motion and contribute to elevated-temperature strength without degradation of other properties **(2)**. In this study, dispersoid-forming element additions were made to the 2024-Al base system, Al-4.4Cu-1.5Mg. The addition of 0.2% Zr was expected to further improve properties by stabilization of a fine subgrain structure, as for the Li-containing alloy discussed below.

Two candidate dispersoid-forming systems, each calculated to produce 4-5 vol% dispersoids, were investigated: 1Fe-1Ni and 4Ti-1.8B. The former system produces Al_9FeNi dispersoids when Fe and Ni are added in equal quantities **(2)**. Durand et al. **(3)** demonstrated 100-120 MPa (14-17 ksi) improvements in yield and tensile strengths, with no loss in ductility, in 7075-Al + (1Fe-1Ni) extrusions made from roller-quenched flakes, compared to I/M 7075-Al. Thermodynamic calculations predict that the stable dispersoid phase in the Al-4Ti-1.8B system is TiB_2. Slaughter and Das **(4)** showed that additions of Ti and B to RSP iron-aluminum alloys produced fine TiB_2 dispersoids, which refined the grain size and were expected to significantly improve mechanical properties.

Aluminum-lithium alloys have lower densities and higher elastic moduli than commercial 2XXX and 7XXX alloys at attractive strength levels, enabling significant weight savings in aircraft structural members **(5,6)**. Conventional I/M Al-Li alloys are limited to $\leq$ 2.6 wt% Li by Li segregation to coarse intermetallics in cast ingots. RSP Al-Li alloys with $\geq$ 3 wt% Li show promise of being consolidated and heat treated to retain microstructural homogeneity and properties combinations superior to those of I/M alloys.

A promising class of Al-Li alloys contains 3% Li, 1.5-2% Cu, and about 1% Mg **(6)**. These alloys have 7-10% lower densities, 15-20% higher specific elastic moduli, and tensile properties comparable to those of 7075-Al, with 3-5% ductility. The (Li+Cu+Mg) level is sufficiently low that few insoluble constituent particles are present after solution-treatment to act as fracture initiation sites and impair ductility. Thus a base composition of Al-3Li-1.5Cu-1Mg appears promising if further alloying additions can be made to improve ductility and toughness.

Zr additions to Al-Li alloys are effective in increasing strength and ductility by preserving a dynamically recovered, unrecrystallized microstructure after solution treatment **(7,8)**. Recrystallization and grain growth are inhibited by a homogeneous distribution of coherent, metastable Al_3Zr dispersoids, which pin subgrain boundaries and stabilize the substructure formed during prior hot working (extrusion, forging, rolling).

Low ductility in Al-Li alloys has been attributed to planar slip, which causes localized stress concentrations at grain boundaries and leads to intergranular failure at low strains. Fine, incoherent dispersoids homogenize slip by forcing Orowan bypassing, thus reducing grain boundary stress concentrations. Dispersoid-forming elements such as Fe, Co, Cr, Mn, Cd, or Y produce significant increases in ductility when added to an RSP binary Al-Li alloy **(7,8)**. Cobalt is readily introduced to form a significant volume fraction of incoherent dispersoids, and was therefore selected for this study.

Based on the above considerations, the composition Al-3Li-1.5Cu-1Mg-0.5Co-0.2Zr was selected, to combine the low density and high specific modulus of an Al-3Li alloy with the solid-solution strengthening of Mg, ductility enhancement by Co-containing dispersoids, and resistance to recrystallization associated with Al_3Zr dispersoids.

3. EXPERIMENTAL PROCEDURE

3.1 Particulate Production

Aluminum alloy powders were produced by vacuum atomization (VA) at Homogeneous Metals, Inc. (HMI), Clayville, NY, using the apparatus shown in Figure 1. An 8-kg charge was induction melted in an argon-filled pressure chamber. Once the melt had been homogenized and heated to the desired temperature, the sealing door was opened and the melt was ejected through a transfer tube into the evacuated powder collection tank. The powder was solidified by the escape of the pressurizing gas and cascaded into a collection vessel which could be valved off from the chamber for transportation and further handling. Typical powder yields ranged from 4.5 to 6.8 kg. Further information on vacuum atomization is available in the literature **(9,10)**.

The MDRL ultrasonic gas atomization (USGA) apparatus, used to produce RSP Al-alloy powders with argon (USGA-Ar) or helium (USGA-He) as the atomizing gas, is shown in Figure 2. A pre-alloyed charge weighing up to 6.8 kg was induction melted in an inert atmosphere. When the desired melt temperature was reached, atomization was initiated by simultaneous activation of solenoids which opened the gas line and an orifice in the floor of the melting crucible. The molten metal was atomized and solidified by a pulsed (80-100 kHz), ultrasonic stream of inert gas emanating from an annular nozzle ring. The atomized powder was recovered from the main chamber collection container and from the cyclone through which the atomizing gas exhausted. Details of USGA are available in the literature **(9-13)**.

The MDRL twin-roller quenching (RQ) appratus, used to produce RSP Al-alloy flakes, is shown in Figure 3. A 900-g charge made from pure aluminum and master alloys was induction melted, homogenized by stirring, and heated to the desired temperature. A plunger sealing a 1.55-mm-diameter hole in the crucible floor was raised sufficiently to allow dropwise flow between two stainless-steel rollers rotating in opposite directions at 1725 rpm. The molten drops were solidified into flakes typically 5 to 10 cm long, 0.5 cm wide, and 125 μm thick. The flakes fell into a collection chamber, where they were retained under inert gas cover. Typical yields were 400 to 600 g per run. The apparatus has been described in detail elsewhere **(14)**.

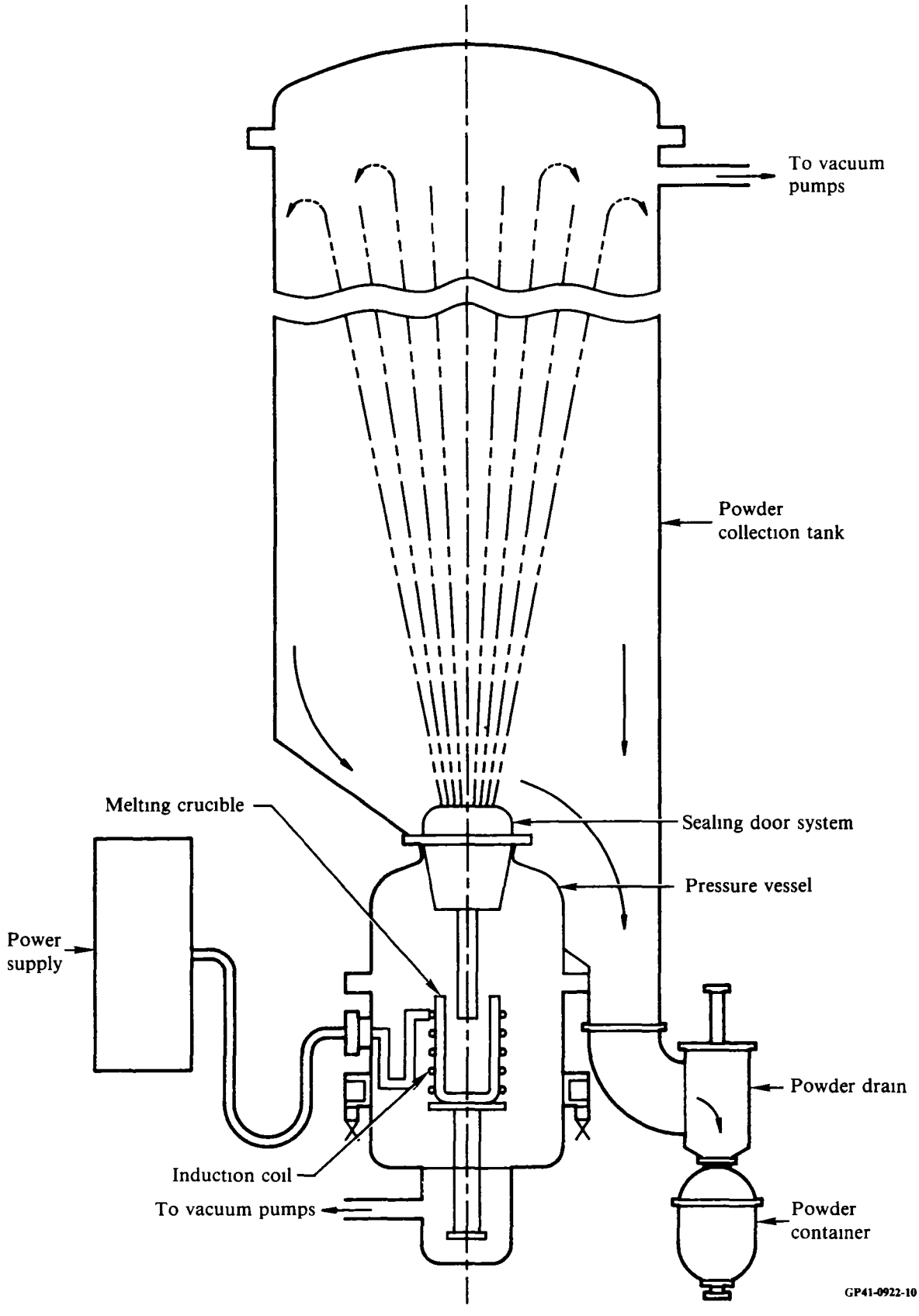

Figure 1. Homogeneous Metals, Inc. vacuum atomization apparatus.

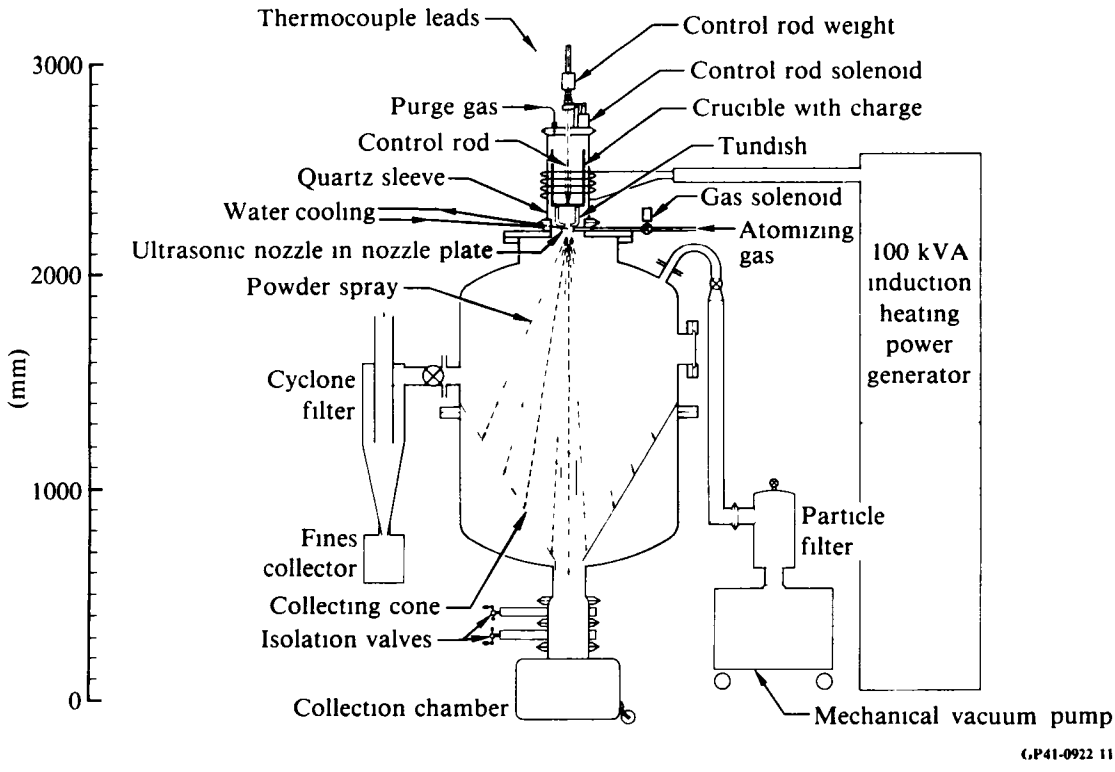

Figure 2. MDRL ultrasonic atomization apparatus.

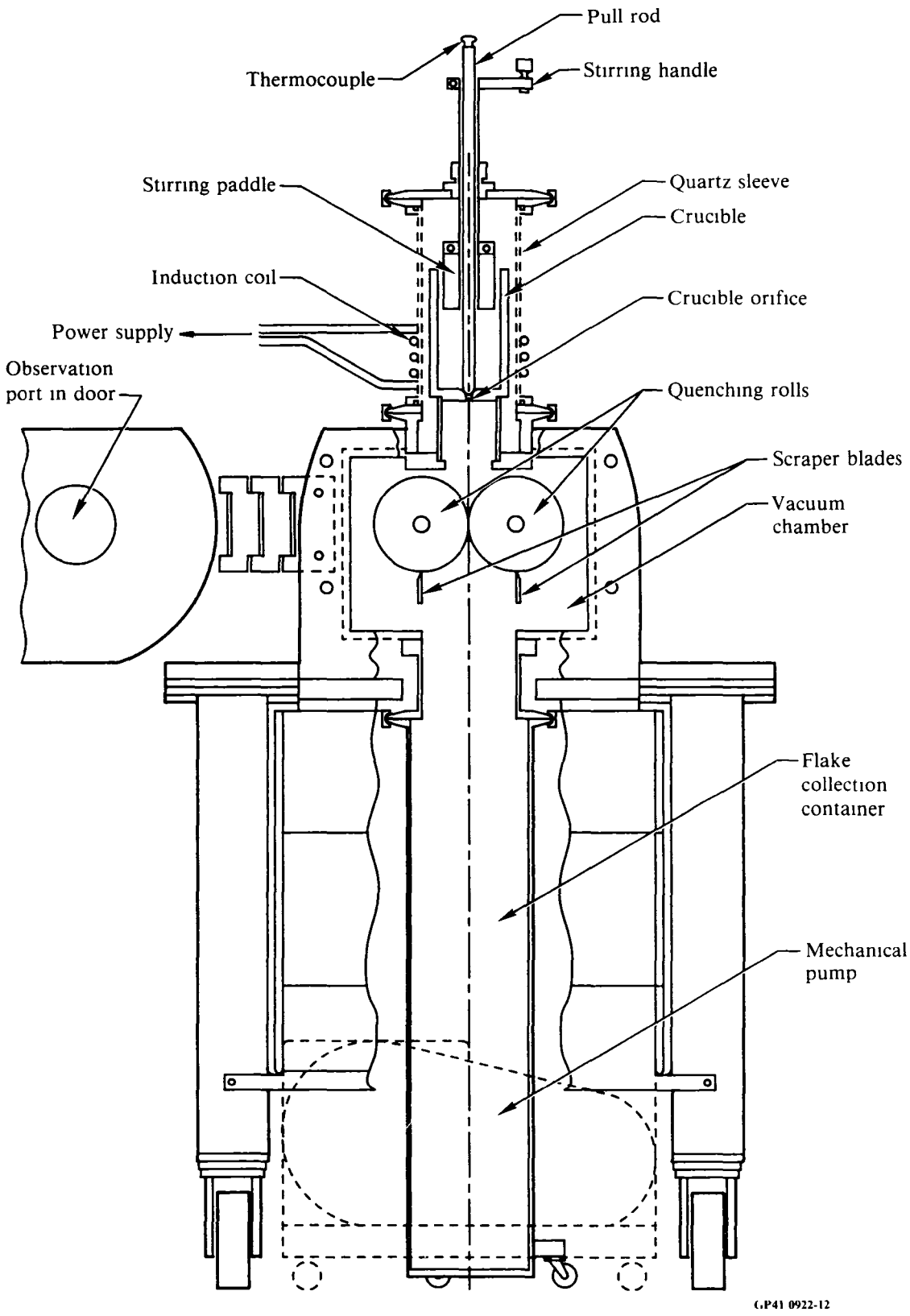

Figure 3. MDRL roller-quenching apparatus.

3.2 Particulate Characterization

As-solidified particulates were chemically analyzed at McDonnell Douglas Corporation for Cu, Mg, Li, Fe, Ni, Co, Cr, Ti, Si, and Zn. Particulates were analyzed for hydrogen and oxygen by a fusion method at Leco, Inc., St. Joseph, MI.

Microstructures of alloy powders and flakes were examined using optical microscopy and scanning electron microscopy (SEM). Optical microscopy was used for characterization of particulate shapes, as-solidified microstructures, and additional features such as porosity or splat caps. Scanning electron micrographs of individual particles were used for determination of dendrite-arm spacings.

Particle size distributions of powders were obtained by sieving 10-g samples according to ASTM E161-70, using electroformed sieves manufactured by the Buckbee-Mears Co., St. Paul, MN. Electroformed sieves have precise tolerances and are relatively free from clogging and particle entrapment; hence they produce particle size distribution data superior to those obtained using wire-woven sieves **(15,16)**. Screens with apertures between 180 and 20 μm were used.

Oxide film thicknesses on as-solidified and as-degassed powders were determined using the Perkin-Elmer Model 600 Scanning Auger Multiprobe at Physical Electronics Laboratories, Eden Prairie, MN. This instrument is capable of obtaining Auger electron spectra, and hence chemical information, over areas as small as 50 nm diameter and 0.5-2.0 nm deep. It can also be used to obtain depth profiles of concentrations of up to 20 individual elements by alternate argon ion sputtering and Auger spectrum determination. After obtaining an initial Auger electron spectrum of a particle surface, the surface was ion milled until the oxygen Auger signal had decreased to approximately 15% of its initial intensity. The oxide layer thickness was obtained from calibration curves determined on Ta_2O_5.

3.3 Consolidation and Post-Consolidation Processing

Approximately 10-g samples of both non-Li- and Li-containing alloy powders were tray degassed in a tube furnace evacuated to 0.13 Pa (10^{-3} Torr), heated rapidly to 400-530°C, and held at temperature for 2 h. Hydrogen and

oxygen analyses of degassed particulates were performed to determine the efficiency of degassing as a function of temperature.

Samples of Al-4.4Cu-1.5Mg-1Fe-1Ni-0.2Zr VA, USGA-Ar, and USGA-He; Al-4.4Cu-1.5Mg-2Fe-2Ni-0.2Zr VA; and Al-3Li-1.5Cu-1Mg-0.5Co-0.2Zr VA, USGA-Ar, USGA-He, and RQ particulates of 2.8 to 9.1-kg mass were consolidated into extrusions by Nuclear Metals, Inc., Concord, MA. The particulates were compacted at ambient temperature into 14-cm-o.d. x 13.3-cm-i.d. x 25.4-cm-long aluminum cans at 152 MPa (22 ksi). The cans were welded and evacuated at temperatures up to 500°C to < 0.1 Pa for degassing, then sealed. The billets were reheated to 400°C and extruded through a 1.27 x 3.81 cm (0.5 x 1.5-in.) rectangular die at 38 cm/min. The extrusion ratio was 29:1. Extrusion compositions were verified by chemical analysis, and hydrogen and oxygen analyses were performed to determine the effectiveness of degassing. Extrusions made from vacuum atomized powder, argon ultrasonically atomized powder, helium ultrasonically atomized powder, and roller-quenched flakes will be referred to by the acronyms VA, USGA-Ar, USGA-He, and RQ, respectively.

Approximately 9-kg lots of Al-4.4Cu-1.5Mg-1Fe-1Ni-0.2Zr and Al-3Li-1.5Cu-1Mg-0.5Co-0.2Zr VA powders were consolidated into forgings at Alcoa Technical Center, Alcoa Center, PA. The powders were canned, vacuum preheated and degassed to 500°C, and hot pressed to 100% dense billets at 500°C. The billets were upset forged on flat dies to approximately 55% reduction in thickness at 400°C.

The solidus temperature of Al-4.4Cu-1.5Mg lies slightly above 530°C **(17)**; thus 530 and 500°C were selected as solution-treatment temperatures for the non-Li-containing alloys. The Al-3Li-1.5Cu-1Mg solidus was estimated by extrapolation from the Al-Li, Al-Cu, and Al-Mg binary systems **(17)** to lie below 577°C; thus 560 and 530°C were chosen as solution-treatment temperatures for the Li-containing alloy.

Aging curves were determined for non-Li-containing alloy extrusions at 190°C by analogy with the known behavior of 2024-Al. Aging curves were determined for Li-containing alloy extrusions at 177°C to yield peak hardness in 8 to 16 h aging time. Natural aging is not applicable to the Li-containing alloy. The aging behavior of forgings was assumed to resemble that of the extrusions.

3.4 Microstructures and Properties of Consolidated Forms

3.4.1 Microstructure, Texture, and Density

Microstructures of extrusions and forgings were determined by OM and TEM. Optical micrographs of all alloys in the as-extruded, as-forged, and solution-treated conditions were obtained to characterize the as-consolidated microstructures and the extent of dissolution of major alloying elements and recrystallization upon solution treatment. TEM micrographs of extrusions and forgings in various tempers were obtained to follow precipitation and aging behavior as a function of particulate type and aging temperature and time, and to correlate microstructural variables with mechanical properties data. Since OM is not sensitive to changes in substructure, {111} pole figures of extrusions and forgings in the as-consolidated and solution-treated conditions were obtained to characterize changes in substructure during solution treatment.

Densities of all extrusions were determined using a two-liquid, density-matching technique developed at Rockwell International Science Center **(18)**. A small alloy sample was placed in a mixture of di-iodomethane (CH_2I_2, 3.32 g/cm^3) and Neothene (1.30 g/cm^3) of approximately the correct density. The appropriate liquid was added until the sample remained suspended. The density of the liquid mixture, equal to that of the sample, was then determined pycnometrically. This method is estimated to yield densities accurate to about ± 0.5%.

3.4.2 Mechanical Properties

The elastic moduli, yield strengths, ultimate tensile strengths, and ductilities of alloy extrusions and forgings in various tempers and orientations were determined at temperatures between 25 and 260°C. Determinations of tensile properties were made on subsize specimens of 3.18-mm diameter and 15.9-mm gage length according to ASTM E8-81. Most data on tensile properties reported here were based on triplicate tests.

Fracture toughnesses of peak-aged extrusions and forgings were determined in the LT and TL orientations using subsize compact-tension specimens. (The symbol L refers to the direction parallel to application of force during extrusion or rolling, and T and S refer to the long and short transverse directions, respectively. In LT and TL, the first letter refers to the

direction of application of force during testing, and the second letter to the direction of crack propagation.) Since the specimens were typically less than 1.27-cm thick, the measured toughness values generally did not meet the plane-strain criterion, and are properly referred to as K_Q rather than K_{IC} (plane-strain fracture toughness) values. K_Q values are not directly comparable with literature or handbook K_{IC} data.

Fatigue-crack-growth-rate (FCGR) data for peak-aged specimens from VA extrusions and forgings were determined in the LT and TL orientations using subsize compact-tension specimens. The test frequency was 5 Hz and the ratio of maximum to minimum load was 0.1.

Steady-state creep rates and stress-rupture data were determined for peak-aged specimens from VA Al-4.4Cu-1.5Mg-1Fe-1Ni-0.2Zr extrusions at 150°C using flat tensile specimens of 2.5-cm gauge length. Tests were conducted under loads corresponding to 70, 80, and 90% of the 150°C yield stress of each alloy.

The stress-corrosion-cracking (SCC) behavior of peak-aged VA extrusions and forgings was determined by alternate-immersion testing of bolt-loaded, subsize C-ring specimens in 3.5% NaCl solution according to ASTM G38-73 and G44-75. Forging samples were tested with crack growth in the S direction, but the extrusions were not thick enough to permit S-orientation testing and hence were tested with crack growth in the T direction. Loads applied to the specimens corresponded to 25, 50, and 75% of the ambient-temperature yield stresses.

4. TASK 1: PRODUCTION AND CHARACTERIZATION OF RAPIDLY SOLIDIFIED POWDERS AND FLAKES

4.1 Evaluation of Dispersoid-Forming Systems for Non-Li-Containing Alloy

Roller-quenched flakes were prepared from 1-kg heats of the prototype dispersoid-forming systems Al-1Fe-1Ni and Al-4Ti-1.8B. Flakes of Al-1Fe-1Ni were successfully prepared at a pouring temperature of 730°C (75°C superheat). Chemical analysis of the flakes yielded an actual composition of Al-0.96Fe-1.02Ni. Optical microscopy of etched surfaces of as-solidified flakes (Figure 4) shows a cellular/dendritic structure with 10- to 30-μm diameter cells and an average dendrite-arm spacing (DAS) of 0.6 μm. Using the correlation of Matyja et al. **(19)** between DAS and cooling rate, the solidification rate was estimated to be ~ 4 x 10^5 K/s.

Figure 4. Optical micrograph of Al-1Fe-1Ni flake.

GP41-0922-13

The evolution of the as-solidified microstructure into one more nearly typical of a consolidated form was approximated by heat treating the flakes for 1 h at 400, 500, and 550°C. TEM micrographs of as-solidified and as-heat

treated flakes (Figure 5) show progressive spheroidization as the temperature is raised, to a final distribution of approximately 0.2- x 0.3-μm oblate dispersoids at the boundaries of 1-μm-diameter subgrains (Figures 5c and 5d). Spheroidization is essentially complete at 500°C. The final distribution of dispersoids is promising for significant dispersion strengthening.

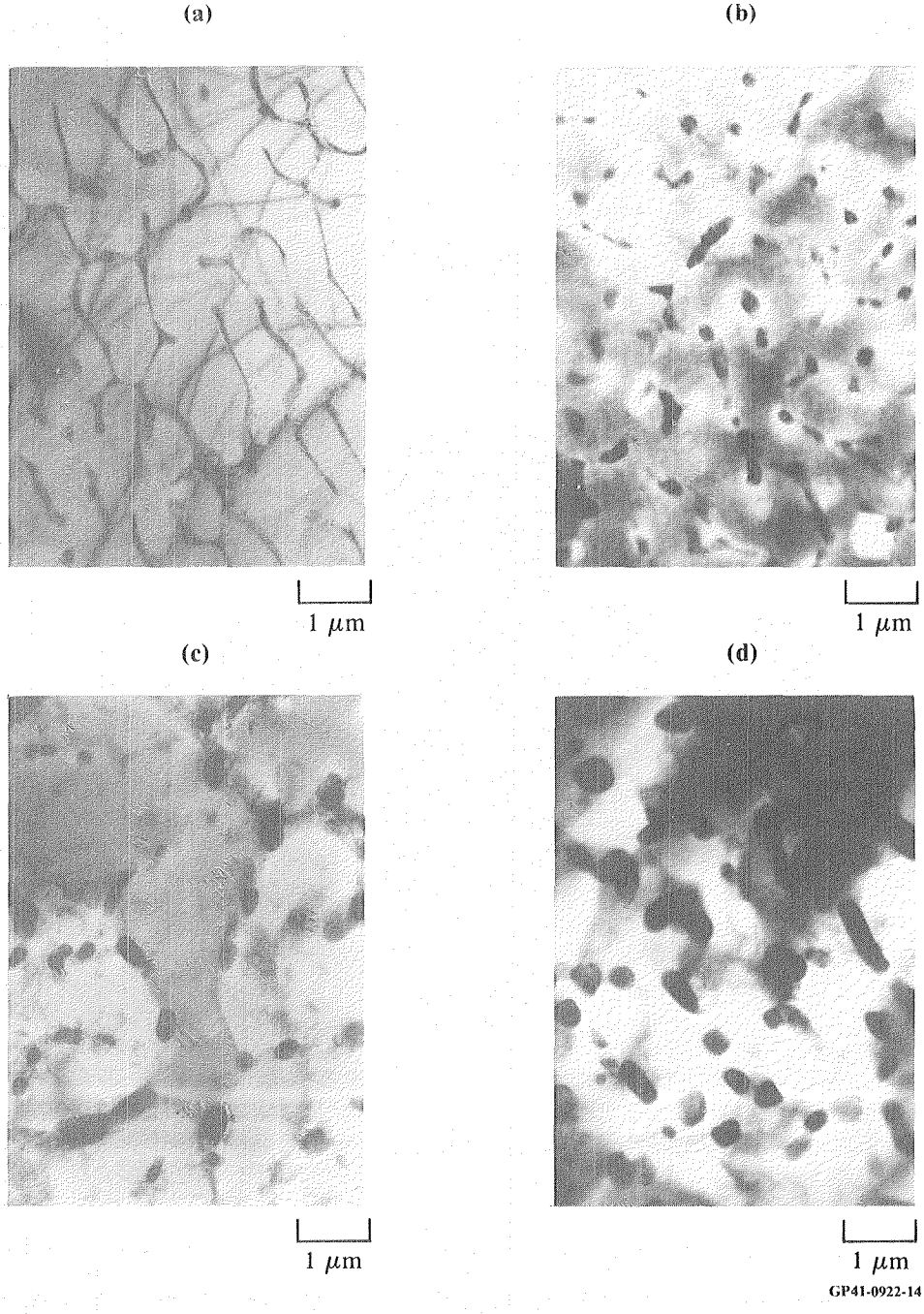

Figure 5. Microstructures of roller-quenched Al-1Fe-1Ni flakes; (a) as-quenched and heat treated for 1 h at (b) 400°C, (c) 500°C, and (d) 550°C.

X-ray and electron diffraction were used to identify the dispersoids in Al-1Fe-1Ni flakes. Results of X-ray diffraction scans show that the dispersoids in both as-solidified and as-heat-treated flakes are predominantly Al_9FeNi, which has the monoclinic Al_9Co_2 structure. Identification of TEM electron diffraction spots and comparison of measured and predicted angles between various directions in the reciprocal lattice support the identification of dispersoids as Al_9Co_2-type. Both X-ray and electron diffraction patterns suggest that traces of other phases may be present in as-solidified flakes.

Reference to the Al-Ti and Al-B phase diagrams **(17)** suggests that a temperature of 1000°C is required to dissolve 4Ti and 1.8B in an aluminum melt. Droplets of Al-4Ti-1.8B heated to a pour temperature of 1000°C in the roller-quenching apparatus, were not quenched to solid flakes by the rolls. Attempting to pour at a melt temperature of 750 to 800°C resulted in retention of unmelted master alloy in the bottom of the crucible which blocked the crucible orifice and prevented flake formation. Since the Al-1Fe-1Ni system produced satisfactory results, no further tests of the Al-Ti-B system were made, and the Fe-Ni system was selected as the dispersoid-forming additive for the non-Li-containing alloys.

4.2 Production of Rapidly Solidified Particulates

4.2.1 Vacuum Atomization

Ingots of 33 kg mass of both Al-4.4Cu-1.5Mg-1Fe-1Ni-0.2Zr and Al-3Li-1.5Cu-1Mg-0.5Co-0.2Zr were vacuum atomized in eight heats. The yield of -80 mesh powder was 18.9 kg for the non-Li-containing alloy and 17.7 kg for the Li-containing alloy; these were sufficient to manufacture extrusions and forgings large enough to perform all required microstructure and mechanical properties evaluations. HMI also produced 5.9 kg of -80 mesh Al-4.4Cu-1.5Mg-2Fe-2Ni-0.2Zr powder.

4.2.2 Ultrasonic Atomization

Sufficient quantities of Al-4.4Cu-1.5Mg-1Fe-1Ni-0.2Zr and Al-3Li-1.5Cu-1Mg-0.5Co-0.2Zr powders for producing extrusions were manufactured by ultrasonic atomization in argon and in helium. Operating parameters for atomiza-

tion, and powder yields, are summarized in Table 1. Although no systematic study of powder characteristics as a function of operating parameters was attempted, a combination of 100°C superheat and 9.7 MPa (1400 psig) delivery pressure yielded satisfactory results. The yield of usable powder was limited by formation of a sintered powder mass at the bottom of the atomization chamber, and attempts to reduce the sintering problem by decreasing the melt temperature from 820 to 730-750°C were only partially successful. The powders were sieved to -80 mesh to eliminate splats and stored in sealed containers under argon pending further processing.

TABLE 1. OPERATING PARAMETERS FOR ULTRASONIC ATOMIZATION OF Al ALLOY POWDERS.

Composition	Atomizing gas	Run no.	Initial melt temperature (°C)	Gas delivery pressure (MPa[psig])	−80 mesh (−180 μm) powder yield, (kg [lb], % of ingot weight)
Al-3Li-1 5Cu-1Mg-0 5Co-0 2Zr	Ar	1	820	8 3 [1200]	
		2	770	9 7 [1400]	5 4 [11 9], 36
		3	750	9 7 [1400]	
Al-3Li-1 5Cu-1Mg-0.5Co-0.2Zr	He	1	750	9 7 [1400]	
		2	750	9 7 [1400]	2 8 [6 2], 19
		3	750	9 7 [1400]	
Al-4 4Cu-1 5Mg-1Fe-1Ni-0 2Zr	Ar	1	750	9 7 [1400]	
		2	750	9 7 [1400]	4 2 [9 2], 37
Al-4 4Cu-1 5Mg-1Fe-1Ni-0 2Zr	He	1	730	9 7 [1400]	
		2	730	9 7 [1400]	3 0 [6 5], 27

GP41-0922 1

4.2.3 Twin Roller Quenching

Approximately 5.1 kg of roller-quenched Al-3Li-1.5Cu-1Mg-0.5Co-0.2Zr flakes were produced for manufacturing extrusions. The flakes were chopped to particulates approximately 0.2-cm x 0.2-m x 125-μm thick in a commercial paper shredder and blended to ensure compositional uniformity in the final extrusion. Attempts to produce large quantities of Al-4.4Cu-1.5Mg-1Fe-1Ni-0.2Zr flakes for extrusions resulted in low yields because of excessive roll pitting and degradation. Production of flakes for extrusions was abandoned in favor of production of Al-4.4Cu-1.5Mg-2Fe-2Ni-0.2Zr vacuum atomized powder.

4.3 Particulate Characterization

4.3.1 Chemical Analyses

Chemical analyses of all particulates are listed in Tables 2 and 3, and hydrogen and oxygen analyses in Table 4. Vacuum-atomized powders are generally clean, with no evidence of cross contamination with Ni-base powders (which

TABLE 2. CHEMICAL ANALYSES OF NON-Li-CONTAINING ALLOY PARTICULATES.

Designation	Composition (wt %)						
	Cu	Mg	Fe	Ni	Zr	Cr	Ti
Nominal composition	4.4	1.5	1.0	1.0	0.2	—	—
Vacuum atomized powder, Lot A	3 86	1 50	0.94	0 98	0.23	0 015	0.004
Vacuum atomized powder, Lot B	4.28	1.56	0.92	0.94	0.20	0.003	0 002
Vacuum atomized powder, Lot C	4 09	1.45	0.94	0.86	0.18	0.003	0.003
Vacuum atomized powder, Lot D	3.91	1.50	0.92	0.95	0.20	0 004	0.002
Ultrasonically atomized powder - argon	4.16	0 88	0.96	0 95	0.18	0 004	0.002
Ultrasonically atomized powder - helium	4.24	0 95	0.92	0 94	0.20	0 004	0.003
Roller-quenched flakes	4.29	1 51	0.82	1 03	0.18	N A	N.A.
Nominal composition	4.4	1.5	2 0	2.0	0.2	—	—
Vacuum atomized powder	4.21	1 03	1.76	1 81	0.22	0 006	0.003

Si, Zn $<$ 0 1 in all particulates

GP41 0922-2

TABLE 3. CHEMICAL ANALYSES OF Li-CONTAINING ALLOY PARTICULATES.

Designation	Composition (wt %)						
	Li	Cu	Mg	Co	Zr	Fe	Ni
Nominal composition	3 0	1 5	1 0	0 5	0 2	—	—
Vacuum atomized powder, Lot A	3 10	1.46	1 06	0 49	0 19	0 018	0 005
Vacuum atomized powder, Lot B	3 08	1 46	1 04	0 49	0 19	0 021	0 007
Vacuum atomized powder, Lot C	3 20	1 46	1 03	0 50	0 19	0 021	0 030
Vacuum atomized powder, Lot D	3 18	1 43	1 03	0 52	0 19	0 041	0 24
Ultrasonically atomized powder - argon	2 76	1 54	0 72	0 47	0 25	0 008	0 011
Ultrasonically atomized powder - helium	2.72	1 44	0 62	0.47	0 17	0 003	0 008
Roller-quenched flakes	3 10	1 59	1 07	0 40	0 10	0 06	0 011

Cr, $<$ 0 014 (VA Lot D, 0 053), Ti, $<$ 0 015 (VA Lot D, 0 020), Si, $<$ 0 05, Zn $<$ 0 10 in all particulates

GP41-0922 3

TABLE 4. HYDROGEN AND OXYGEN ANALYSES OF PARTICULATES AND EXTRUSIONS.

Alloy composition and atomization method	Hydrogen concentration (wppm)		Oxygen concentration (wppm)	
	Particulates	Extrusions	Particulates	Extrusions
Al-4.4Cu-1.5Mg-1Fe-1Ni-0.2Zr				
Vacuum atomization	27 ± 2	2	370 ± 130	910 ± 30
Ultrasonic atomization - argon	43 ± 2	4	440 ± 120	570 ± 60
Ultrasonic atomization - helium	35 ± 2	1	350 ± 110	760 ± 60
Roller quenching (flakes)	5 ± 1	—	—	—
Al-4.4Cu-1.5Mg-2Fe-2Ni-0.2Zr				
Vacuum atomization	—	5	—	1280 ± 10
Al-3Li-1.5Cu-1Mg-0.5Co-0.2Zr				
Vacuum atomization	164 ± 2	< 20	200 ± 60	480 ± 60
Ultrasonic atomization - argon	234 ± 2	2	280 ± 110	650 ± 140
Ultrasonic atomization - helium	197 ± 5	18	280 ± 130	1320 ± 300
Roller quenching (flakes)	31 ± 1	4	15 ± 10	160 ± 40

GP41 0922 4

are made at HMI in the same apparatus) except for significant, but not deleterious, concentrations of Ni, Cr, and Ti in Lot D of the Li-containing alloy. Compositions of vacuum-atomized powders are close to nominal, except for approximately 10% low Cu concentrations in the non-Li-containing alloy.

Both USGA and RQ particulates made at MDRL have low contaminant levels. The ingots supplied by HMI for ultrasonic atomization did not have sufficiently high Li and Mg concentrations to compensate for the 10% Li and 30% Mg losses caused by vaporization or oxidation in the conversion to powder. For roller-quenched flakes, Li and Mg concentrations in the initial melts were increased by 5 to 7% over nominal to produce the correct concentrations of these elements in the flakes.

Hydrogen concentrations in as-solidified Li-containing alloy particulates are consistently 5.5-6 times larger than those in the non-Li-containing alloy, regardless of particulate type. This result has been attributed to the high reactivity of lithium with water vapor. Hydrogen concentrations in as-solidified roller-quenched flakes are about one-sixth as large as those in powders, because of the smaller surface area per unit volume of the flakes. Oxygen contents of the particulates are low compared to similar alloys produced under MDRL Independent Research and Development **(20)**, which had initial

concentrations as high as 4000 ppm, and surprisingly slightly lower in the Li-containing than in the non-Li-containing alloy.

4.3.2 Particle Size Distribution

Particle size distributions of Al-alloy powders are plotted in Figures 6 and 7. All the distributions follow log-normal behavior. Weight-averaged particle diameters corresponding to 5, 50, and 95% smaller than a given diameter are summarized for each composition and atomization method in Tables 5 and 6.

Particle size distributions of both alloys are similar for both VA and USGA-Ar. The vacuum atomized powder has a smaller mean particle size (38 to 40 μm) than the argon atomized powder (62 to 70 μm), and a narrower size distribution. The USGA-He powder has the widest size distribution, and a smaller average particulate diameter in the Li-containing alloy (29 μm) than in the non-Li-containing alloy (52 μm). This size difference probably results from a higher melt temperature for the Li-containing alloy (see Table 1), consistent

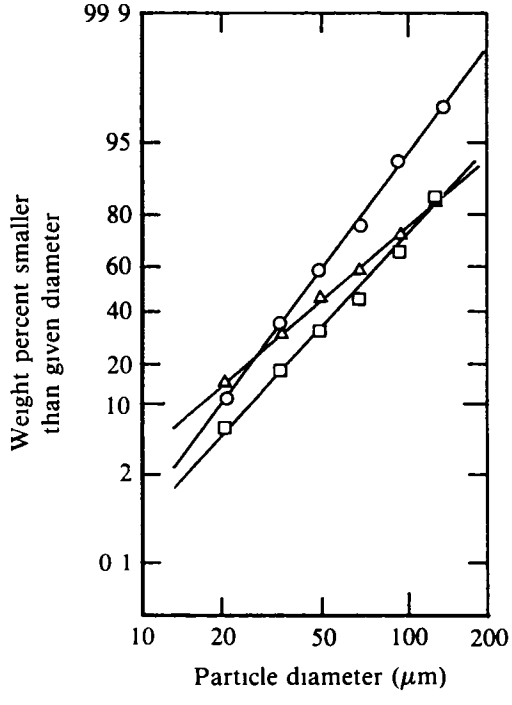

Figure 6. Particle size distributions of Al-4.4Cu-1.5Mg-1Fe-1Ni-0.2Zr powders: (○) Vacuum atomized, (□) argon ultrasonically atomized, and (△) helium ultrasonically atomized.

GP41-0922 15

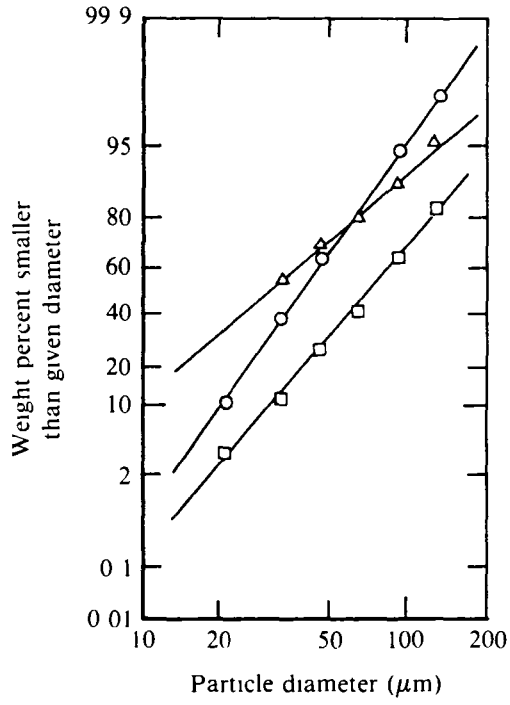

Figure 7 Particle size distributions of Al-3Li-1.5Cu-1Mg-0.5Co-0.2Zr powders: (○) Vacuum atomized, (□) argon ultrasonically atomized, and (△) helium ultrasonically atomized.

GP41 0922 16

TABLE 5. MEAN PARTICLE DIAMETERS, DENDRITE ARM SPACINGS, AND SOLIDIFICATION RATES FOR Al-4.4Cu-1.5Mg-1Fe-1Ni-0.2Zr PARTICLES.

	Atomization method		
	Vacuum atomization	**Ultrasonic atomization - argon**	**Ultrasonic atomization - helium**
Geometric mean particle diameter (μm)	40	64	52
Standard deviation	1 74	2 03	2 44
Dendrite arm spacings for mean and ± one standard deviation particle sizes (μm)	2 57, 3 30, 1 72	2 55, 3 63, 1.38	1 29, 2 53, 0 63
Approximate solidification rates for mean and ± one standard deviation particle sizes (K/s)	$8\ 1\times10^{3}$ $3\ 9\times10^{3}$, $2\ 7\times10^{4}$,	$8\ 3\times10^{3}$ $2\ 9\times10^{3}$, $5\ 1\times10^{4}$,	$6\ 3\times10^{4}$ $8\ 5\times10^{3}$, $5\ 3\times10^{5}$,

GP41-0922 5

TABLE 6. MEAN PARTICLE DIAMETERS, DENDRITE ARM SPACINGS, AND SOLIDIFICATION RATES FOR Al-3Li-1.5Cu-1Mg-0.5Co-0.2Zr PARTICLES.

	Atomization method		
	Vacuum atomization	**Ultrasonic atomization - argon**	**Ultrasonic atomization - helium**
Geometric mean particle diameter (μm)	38	70	29
Standard deviation	1 70	1.92	2.43
Dendrite arm spacings for mean and ± one standard deviation particle sizes (μm)	2 41, 3 51, 1 56	3 09, 3 66, 1 93	0 84, 1 57, 0 45
Approximate solidification rates for mean and ± one standard deviation particle sizes (K/s)	$9\,8\times10^{3}$, $3\,2\times10^{3}$, $3\,6\times10^{4}$	$4\,7\times10^{3}$, $2\,8\times10^{3}$, $1\,9\times10^{4}$	$2\,2\times10^{5}$, $3\,5\times10^{4}$, 1.4×10^{6}

GP41-0922 6

with observations by Grant **(9)**. The results also suggest that particulate size distributions in rapidly solidified aluminum alloys are primarily functions of atomization method, atomizing gas pressure, and melt superheat, but not of compositional differences.

4.3.3 Metallographic Powder Characterization

Optical micrographs of as-atomized alloy powders are shown in Figures 8 and 9. All powders are predominantly spherical, regardless of composition or atomization method, and have dendritic or cellular microstructures. The VA powders (Figures 8a and 9a) have larger numbers of satellites (small particles bonded to larger ones, top center Figure 8a) and splat caps (resulting from collision of a solid particle with a liquid droplet, right center Figure 9a) than do USGA powders, in agreement with previous observations **(9)**. The presence of satellites and splat caps can impair particle packing during consolidation and decrease microstructural homogeneity in consolidated forms, thus degrading mechanical properties **(9)**.

All the powders have occasional porous particles (upper right in Figure 9b). Such particles are rare except in USGA-He Al-3Li-1.5Cu-1Mg-0.5Co-

0.2Zr, where most particles contain internal voids. Completely contained gas bubbles are undesirable because they may lead to high concentrations of H and O in consolidated forms.

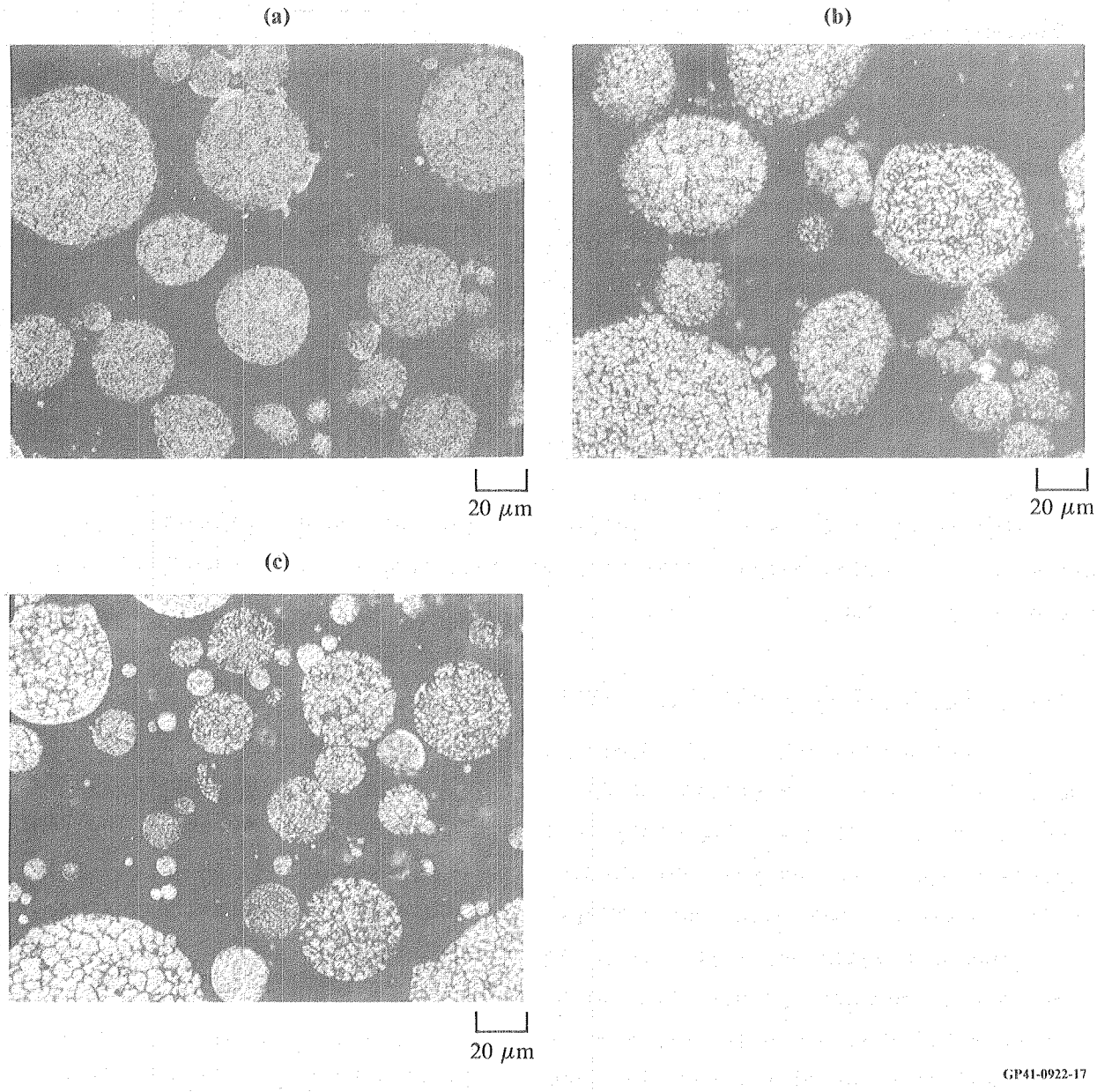

Figure 8. Optical micrographs of Al-4.4Cu-1.5Mg-1Fe-1Ni-0.2Zr powders: (a) vacuum atomized, (b) ultrasonically atomized in argon, and (c) ultrasonically atomized in helium.

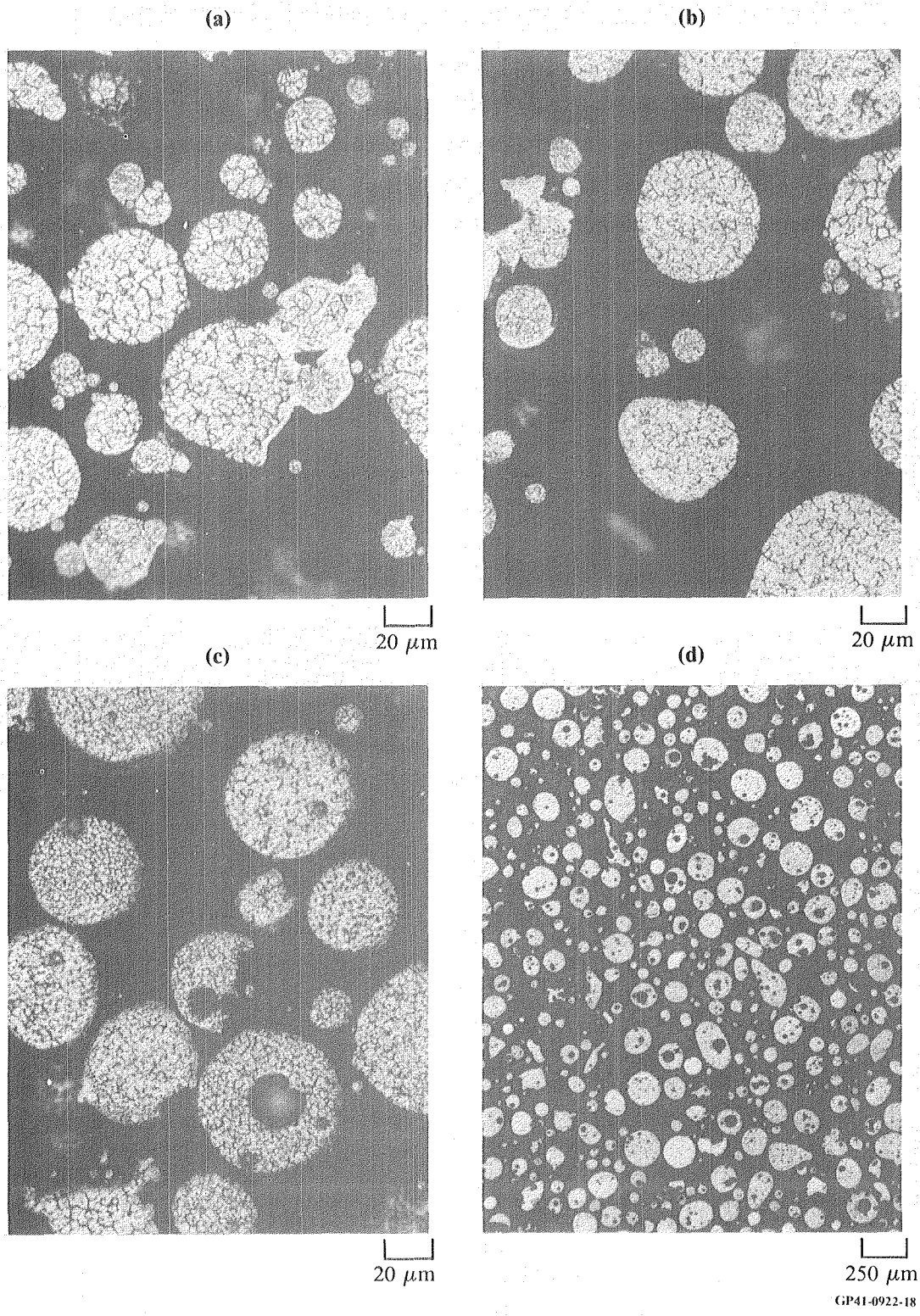

Figure 9. Optical micrographs of Al-3Li-1.5Cu-1Mg-0.5Co-0.2Zr powders: (a) vacuum atomized, (b) ultrasonically atomized in argon, (c) and (d) ultrasonically atomized in helium.

4.3.4 SEM Characterization and Dendrite Arm Spacing Measurements

SEM micrographs of typical VA, USGA-Ar, and USGA-He particles are shown in Figure 10. Cellular microstructures are clearly visible on the unetched particle surfaces. Major microstructural features are similar to those observed optically (Figures 8 and 9), but since the full particle diameter is visible in the SEM micrographs, dendrite-arm spacings and particle diameters can be unambiguously related.

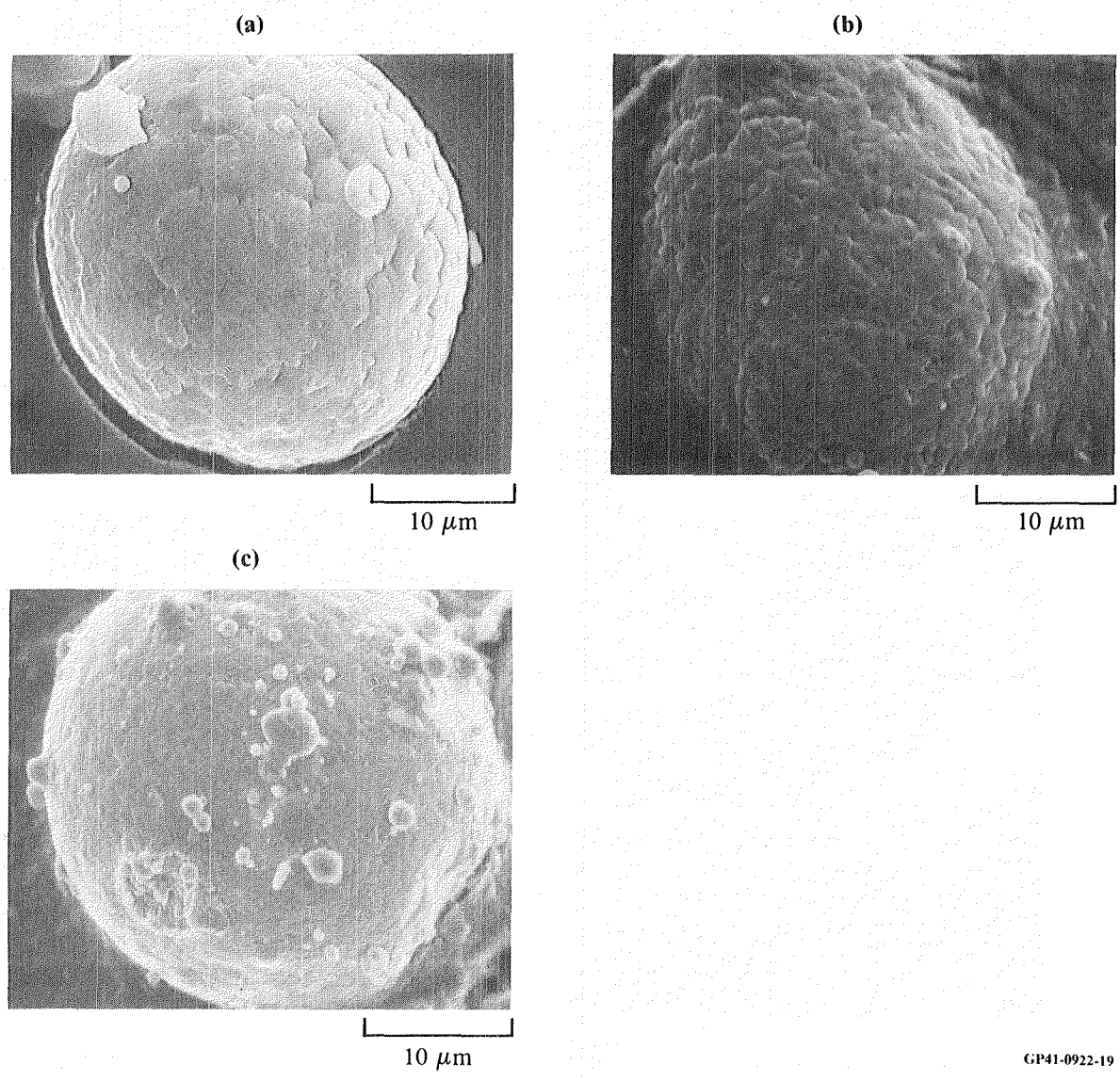

Figure 10. Scanning electron micrographs of Al-4.4Cu-1.5Mg-1Fe-1Ni-0.2Zr particles prepared by (a) vacuum atomization, (b) ultrasonic atomization in argon, and (c) ultrasonic atomization in helium.

Plots of dendrite-arm spacing (DAS) as a function of particle diameter for each alloy composition and atomization method are shown in Figures 11-16. Each data point represents the average of 12-20 DAS measurements on a single particle, and the solid curve on each graph is the best three-parameter polynomial fit to the data. Similar curves have been obtained for aluminum alloy powders by Grant **(9)**.

For each alloy composition, the DAS curve for helium ultrasonic atomization falls well below that for argon ultrasonic atomization, which in turn falls somewhat below that for vacuum atomization. Thus a USGA-He powder particle of mean diameter has been solidified more rapidly than a similar USGA-Ar particle, and the mean USGA-Ar particle has been solidified more rapidly than a similar VA particle. This progression is in accord with the expected solidification rates based on the relative efficiencies of helium, argon, and reduced-pressure argon (in "vacuum" atomization) as heat-transfer media.

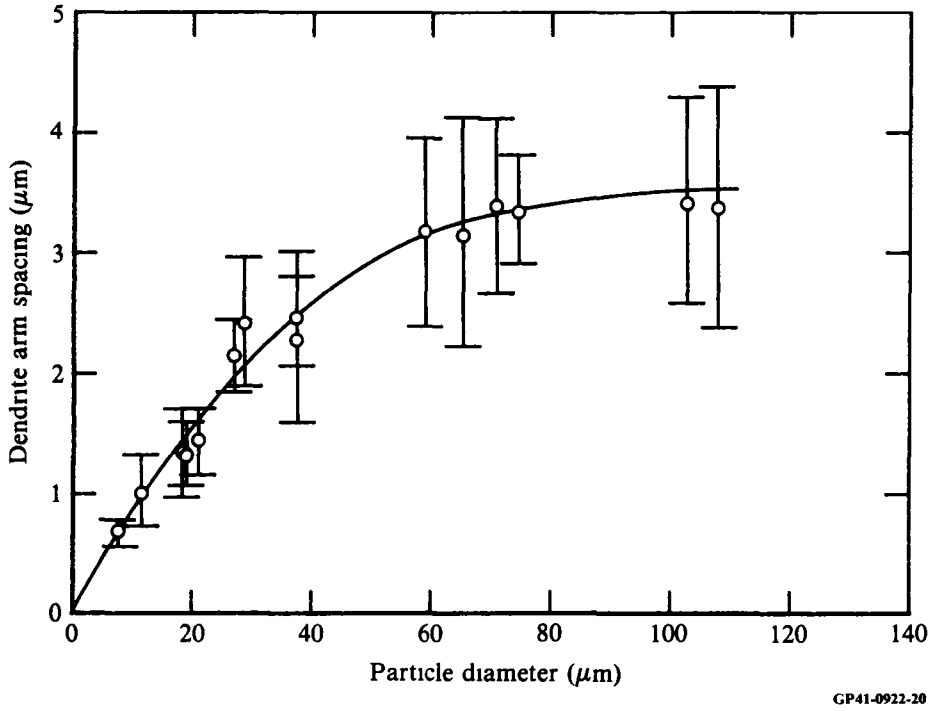

Figure 11. Dendrite arm spacing as a function of particle diameter for Al-4.4Cu-1.5Mg-1Fe-1Ni-0.2Zr vacuum atomized powder.

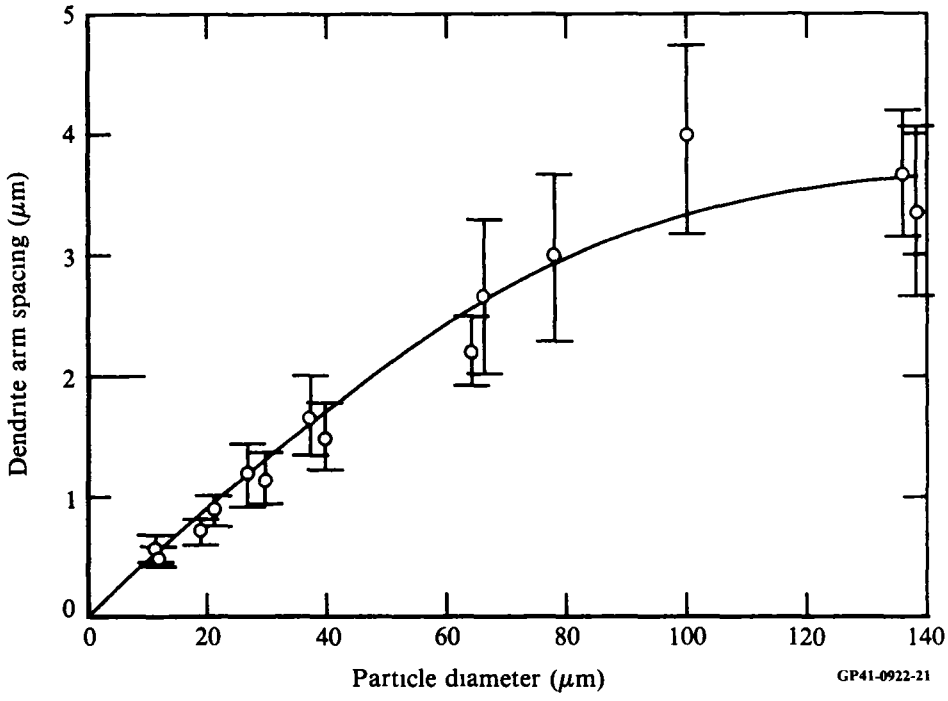

Figure 12. Dendrite arm spacing as a function of particle diameter for Al-4.4Cu-1.5Mg-1Fe-1Ni-0.2Zr argon ultrasonically atomized powder.

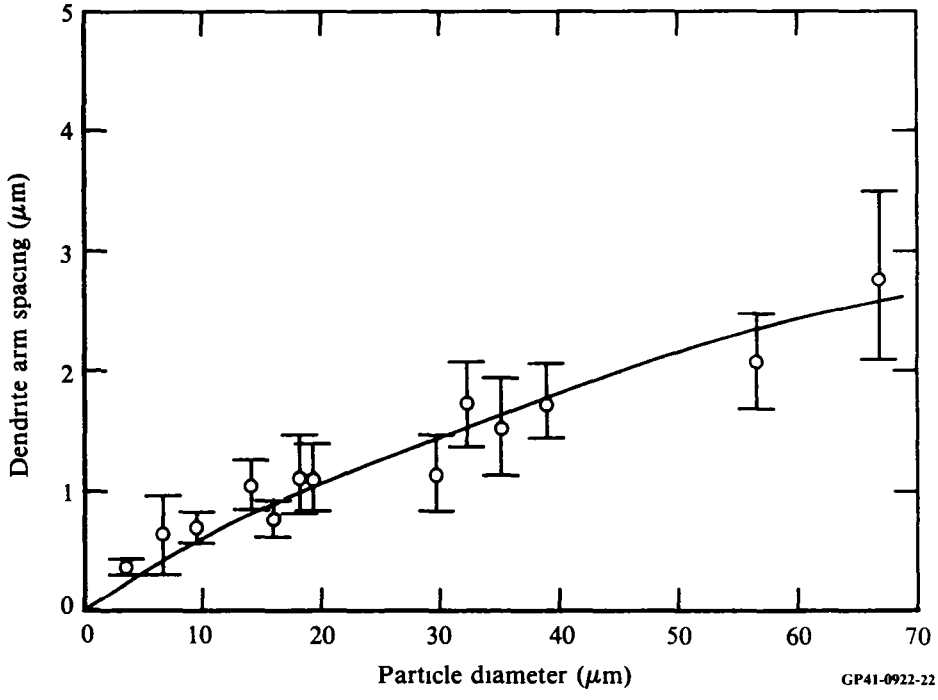

Figure 13. Dendrite arm spacing as a function of particle diameter for Al-4.4Cu-1.5Mg-1Fe-1Ni-0.2Zr helium ultrasonically atomized powder.

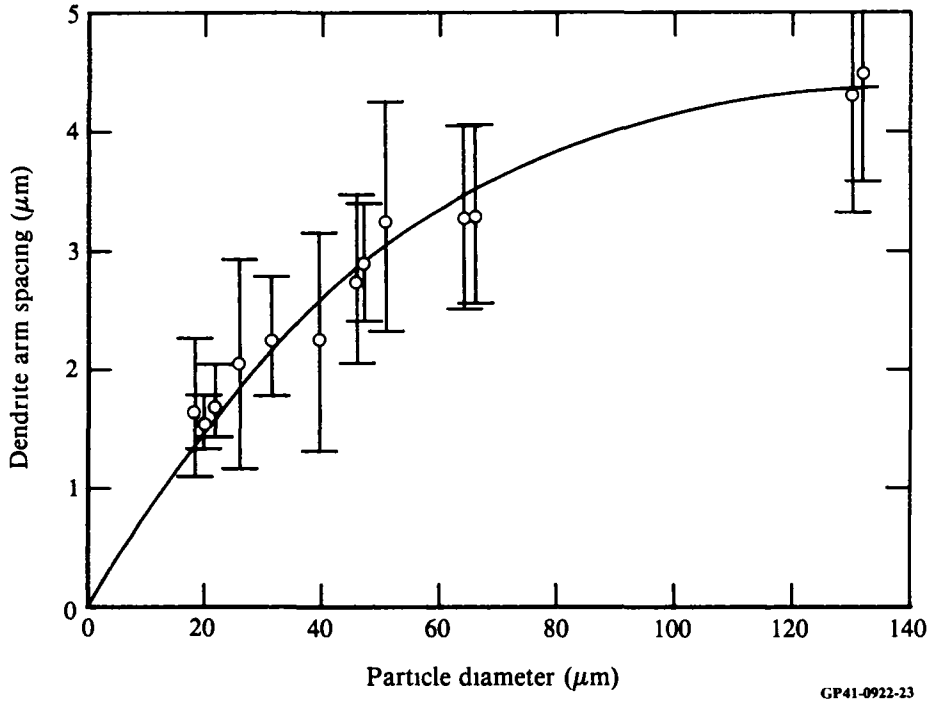

Figure 14. Dendrite arm spacing as a function of particle diameter for Al-3Li-1.5Cu-1Mg-0.5Co-0.2Zr vacuum atomized powder.

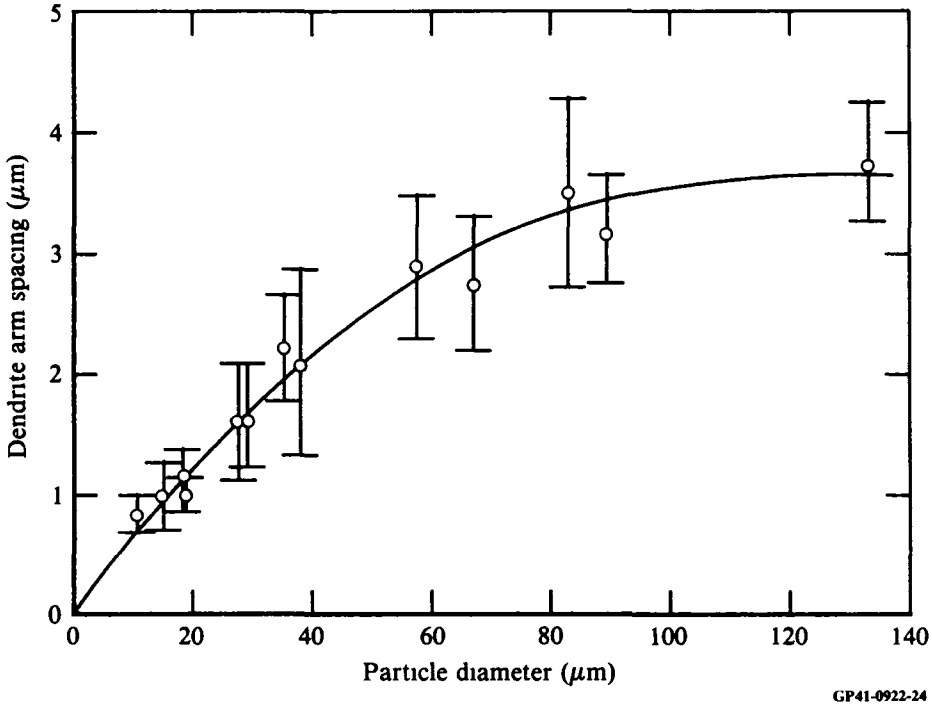

Figure 15. Dendrite arm spacing as a function of particle diameter for Al-3Li-1.5Cu-1Mg-0.5Co-0.2Zr argon ultrasonically atomized powder.

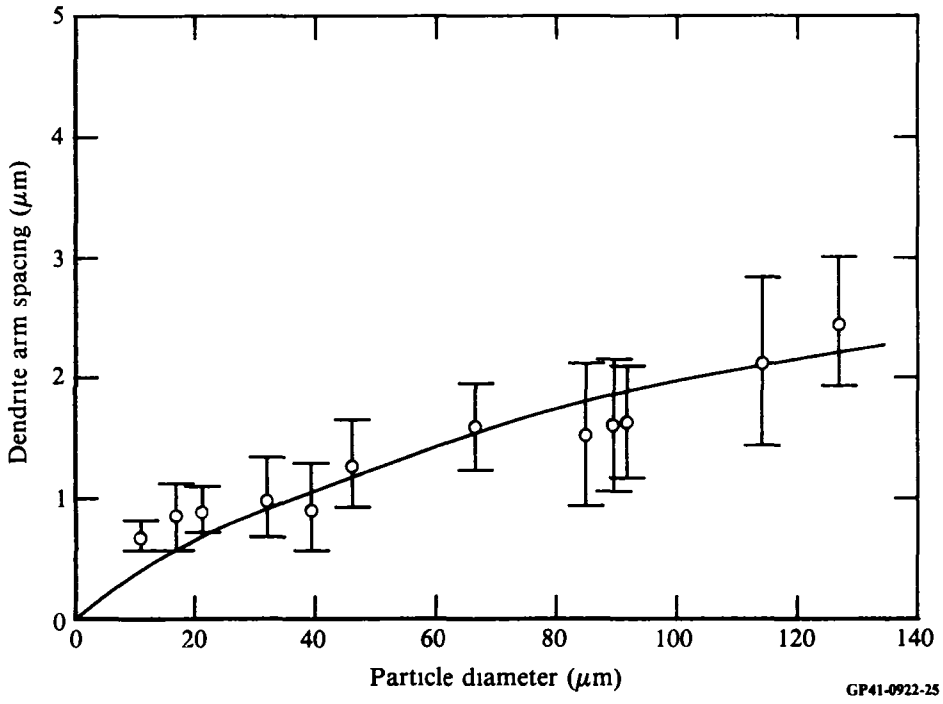

Figure 16. Dendrite arm spacing as a function of particle diameter for Al-3Li-1.5Cu-1Mg-0.5Co-0.2Zr helium ultrasonically atomized powder.

Average dendrite-arm spacings for particles of mean diameter and one standard deviation larger or smaller than the mean diameter are tabulated in Tables 5 and 6. (A factor of one standard deviation around the mean covers the range between 16 and 84% smaller than a given diameter.) These dendrite-arm spacings have been converted to approximate solidification rates using the correlation developed by Matyja et al. **(19)**. For Al-4.4Cu-1.5Mg-1Fe-1Ni-0.2Zr (Table 5), average particle sizes for powders atomized by all three methods are roughly similar. The inherently larger solidification rate obtainable from USGA-He causes the average USGA-He particle to have a solidification rate almost an order of magnitude larger than that for USGA-Ar or VA powders (60 000 K/s vs. 8000 K/s). This difference is more pronounced for fine and less pronounced for coarse powders, owing to the wide size distribution of USGA-He powder. The smaller average diameter of VA powder is compensated for by the higher solidification rate of USGA-Ar powder to yield approximately equivalent solidification rates for particles of mean diameter prepared by these two methods.

For Al-3Li-1.5Cu-1Mg-0.5Co-0.2Zr, the USGA-He powder has both a smaller average particle size and a larger inherent solidification rate than do the other powders, and hence has an average solidification rate for particles of mean diameter about 20 times larger than that of VA powder and about 50 times larger than that of USGA-Ar powder. The smaller average diameter of VA powder more than compensates for the larger inherent solidification rate of USGA-Ar powder to yield a weight-averaged solidification rate about twice as large for the former.

4.3.5 Oxide Layer Thickness Characterization

An Auger electron spectrum of the surface of an as-received VA Al-4.4Cu-1.5Mg-1Fe-1Ni-0.2Zr particle (Figure 17a) shows significant carbon contamination from handling and atmospheric exposure, and an oxide rich in Mg and Al and relatively poor in Cu (compare the relative Mg and Cu heights in Figure 18a with the nominal composition of the alloy). After obtaining the initial spectrum on this particle, the surface was argon ion sputtered at an approximate rate of 0.7 nm/min, and Auger peak intensities for Al, Cu, Mg, O, and C were obtained after each 30 s exposure. The plot of peak intensity as a function of depth (Figure 17b) shows that the oxide film is about 1.7 nm thick and is strongly enriched in Mg. (Also compare Figures 17a and 17c.) This thin oxide layer corresponds well to the < 0.04 wt% oxygen concentration in the powder (Table 4). Copper is rejected from the film, in accord with the relative thermodynamic stabilities of copper and magnesium oxides. After extended sputtering, the Auger spectrum of the matrix (Figure 17c) shows strong Al and Cu peaks, a weak Mg peak near 1200 eV, and virtually no C or O. (The indium signal originates from In atoms from the substrate, deposited onto the particle during sputtering.)

The initial spectrum of an as-received VA Al-3Li-1.5Cu-1Mg-0.5Co-0.2Zr particle (Figure 18a) is similar to that of as-received VA Al-4.4Cu-1.5Mg-1Fe-1Ni-0.2Zr (Figure 17a), with a strongly Mg-enriched oxide on the surface. The depth profile (Figure 18b) shows that the oxide is about 3.5 nm thick. The oxide is enriched in Mg throughout and may be enriched in Li, although the major Auger peak for Li is weak and difficult to evaluate quantitatively. The matrix spectrum (Figure 18c) resembles that of the non-Li-containing matrix (Figure 17c) except for a larger residual oxygen concentration.

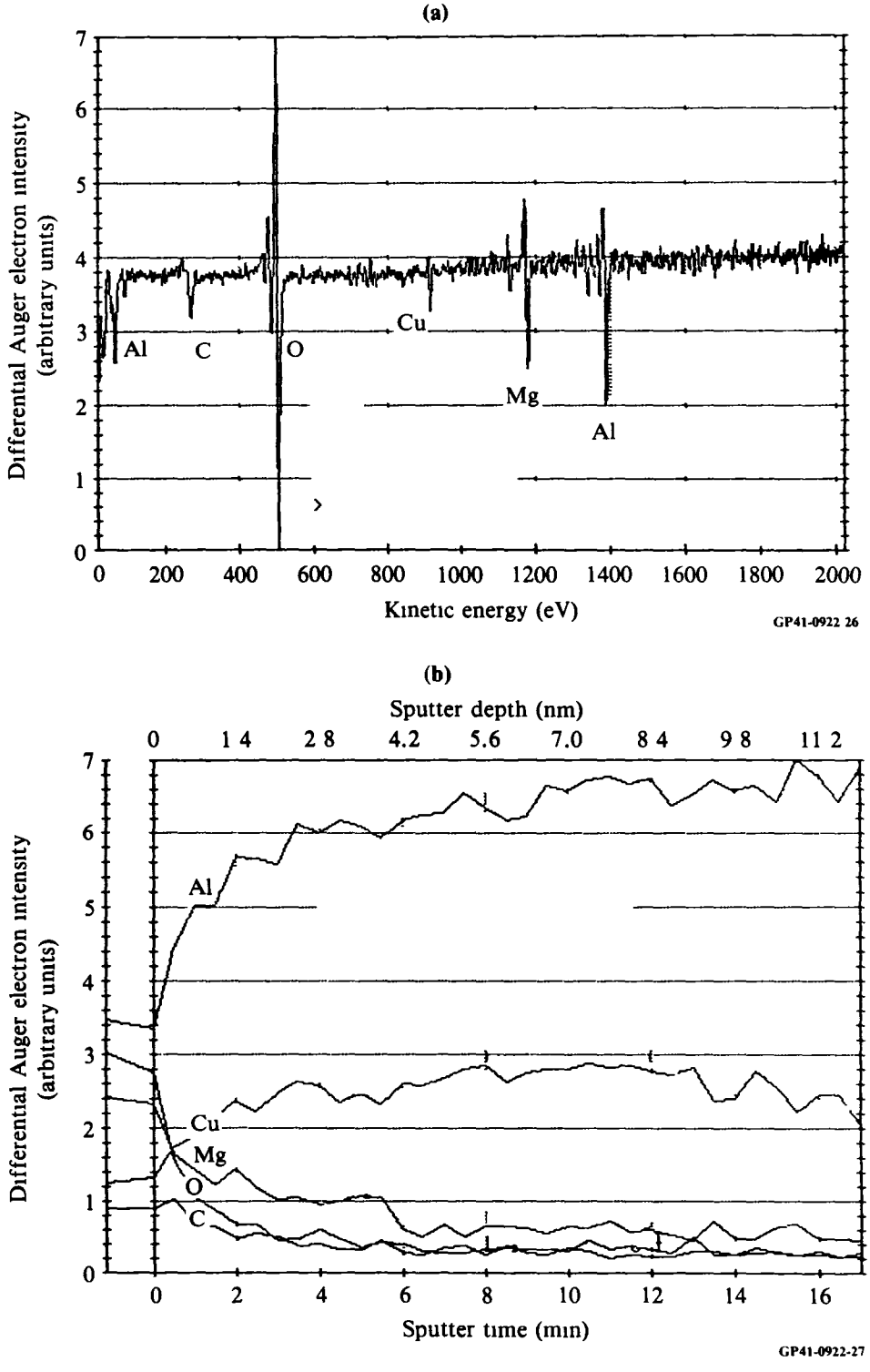

Figure 17. Scanning Auger Microscope (SAM) results for as-vacuum-atomized Al-4.4Cu-1.5Mg-1Fe-1Ni-0.2Zr particle: (a) Auger electron spectrum of as-received particle, (b) depth profile of Al, Cu, Mg, O, and C concentrations, sputtering rate 0.7 nm/min, and (c) Auger electron spectrum of underlying matrix.

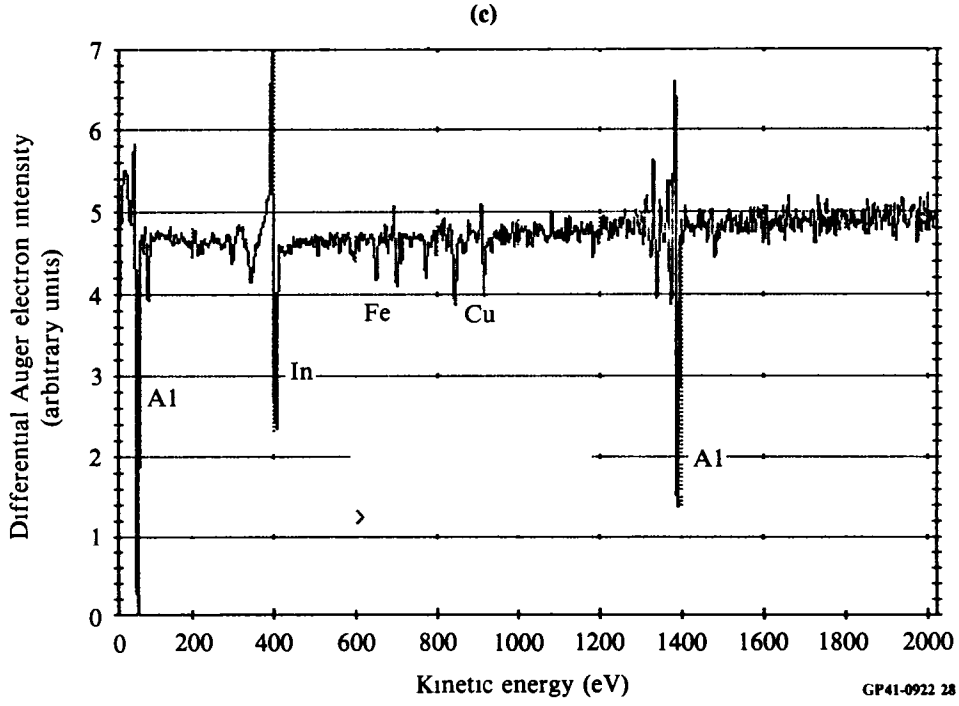

Figure 17. (Concluded)

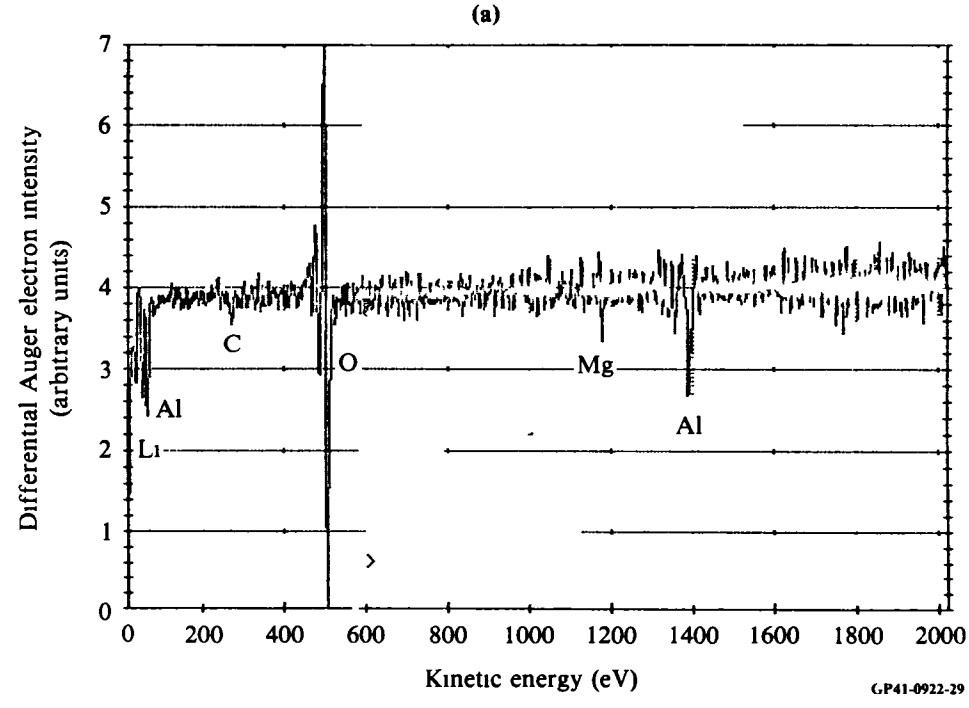

Figure 18. SAM results for as-vacuum-atomized Al-3Li-1.5Cu-1Mg-0.5Co-0.2Zr particle: (a) Auger electron spectrum of as-received particle, (b) depth profile of Al, Cu, Mg, Li, O, and C concentrations, sputtering rate 0.7 nm/min, and (c) Auger electron spectrum of underlying matrix.

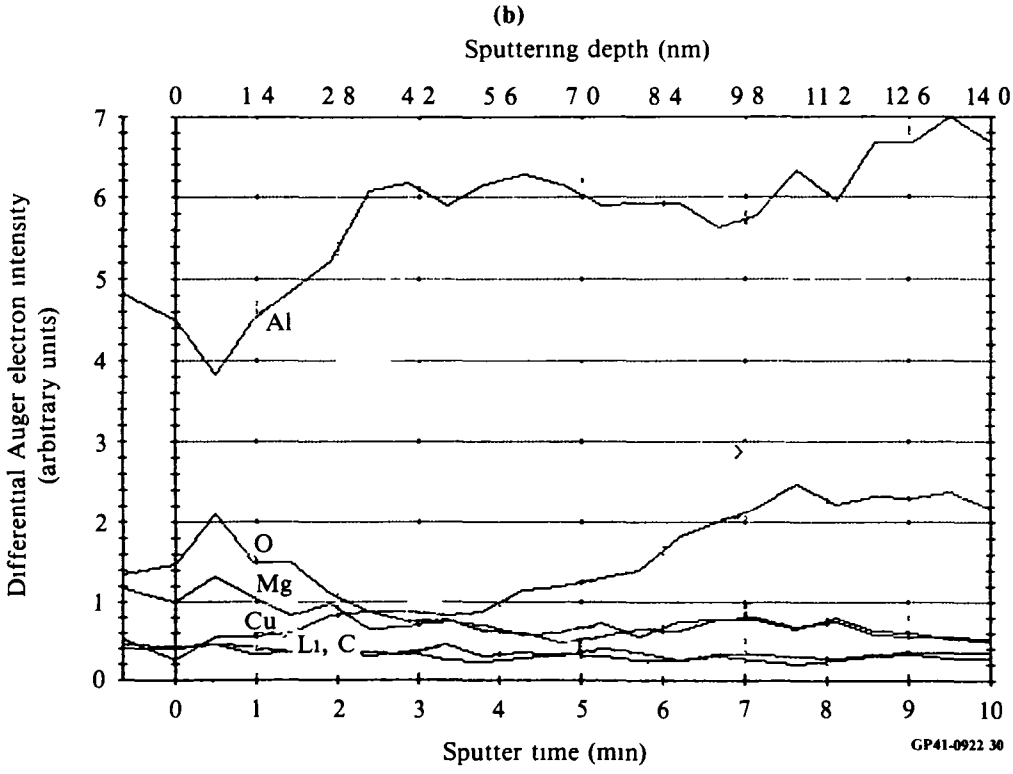

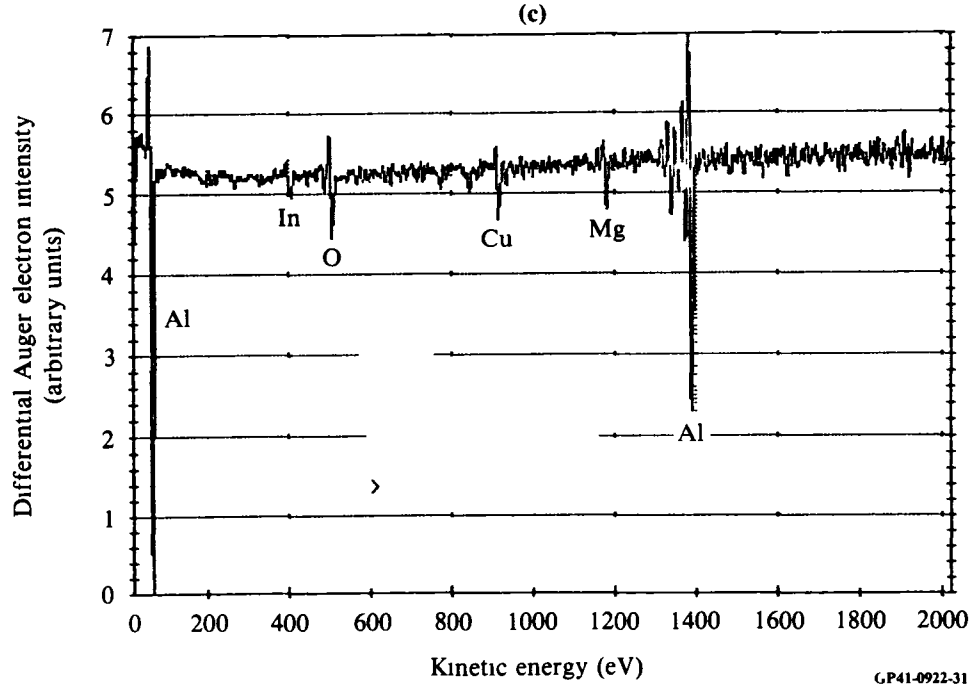

Figure 18. (Concluded).

Depth profiles of oxide films on USGA-He alloy particles are shown in Figure 19. The oxide layers are about 3 nm thick for Al-4Cu-1.5Mg-1Fe-1Ni-

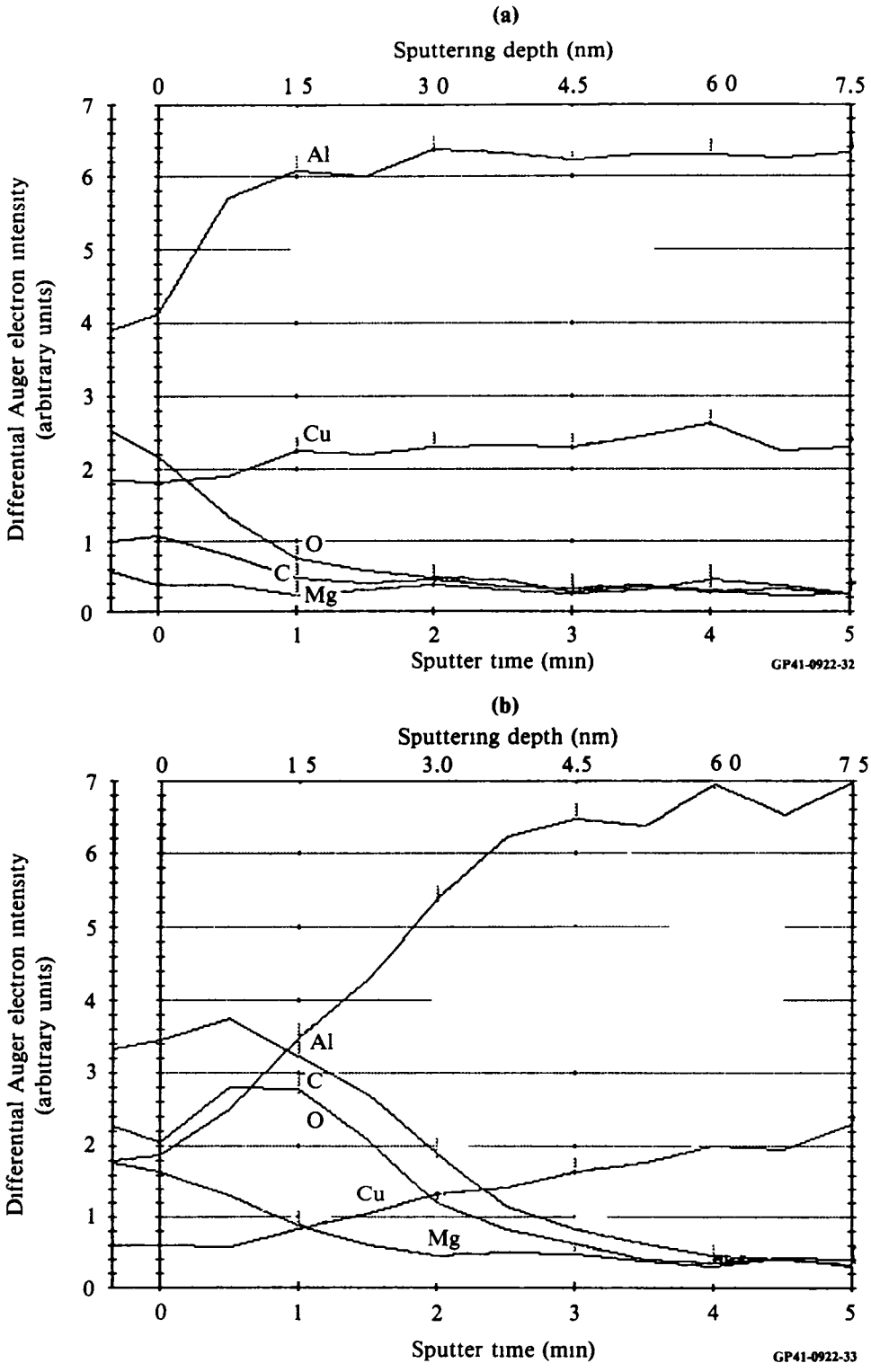

Figure 19. Depth profiles of oxide films on helium atomized particles. Sputter rate 1.5 nm/min: (a) Al-4.4Cu-1.5Mg-1Fe-1Ni-0.2Zr and (b) Al-3Li-1.5Cu-1Mg-0.5Co-0.2Zr.

0.2Zr and 4.2 nm thick for Al-3Li-1.5Cu-1Mg-0.5Co-0.2Zr. Oxide film thicknesses are only slightly greater in Li-containing than in non-Li-containing alloy powders, suggesting that the initially formed oxide layer is passive and does not grow rapidly at ambient temperature, even when the reactive element Li is present.

5. TASK 2: CONSOLIDATION AND POST-CONSOLIDATION PROCESSING OF PARTICULATES

5.1 Particulate Degassing Experiments

5.1.1 Removal of Hydrogen and Oxygen

Hydrogen and oxygen concentrations in powder samples, tray degassed in vacuum at 400-530°C, are shown in Figures 20 and 21. Efficiency of hydrogen removal from the non-Li-containing alloy increases with increasing degassing temperature, but residual hydrogen concentrations in the Li-containing alloy pass through a minimum and increase sharply above 450°C (Figure 21). This result suggests competition between two processes in vacuum degassing of the Al-3Li-1.5Cu-1Mg-0.5Co-0.2Zr alloy: removal of initially adsorbed hydrogen-bearing species by the vacuum, and reaction of such species with Li in the alloy to chemically fix hydrogen. If the temperature dependence of the rate of the hydrogen-fixing chemical reaction exceeds that of physical degassing, the latter reaction is more rapid at lower temperatures and the H concentration decreases as the degassing temperature is raised. At still higher temperatures, more of the hydrogen is chemically fixed than physically removed, and the H concentration increases with increasing temperature. The non-Li-containing alloy lacks a reactive chemical species to fix H, and degassing becomes continuously more efficient as the temperature is raised.

Oxygen concentration data (Figure 21) show that oxygen is not effectively removed in tray degassing of either alloy powder. Within large uncertainty limits, the final O content of the non-Li-containing alloy is independent of degassing temperature and somewhat larger than that in the original powder. This result is consistent with scanning Auger microscopy (SAM) studies discussed in Section 5.1.2. Degassing at temperatures below 500°C approximately doubles the oxygen content in the Li-containing alloy powder. The sharp increase in oxygen concentration during 530°C degassing suggests that the powder reacts rapidly with oxygen at this temperature, leading to a rapid increase in the oxide layer thickness, a result in agreement with the SAM findings discussed below.

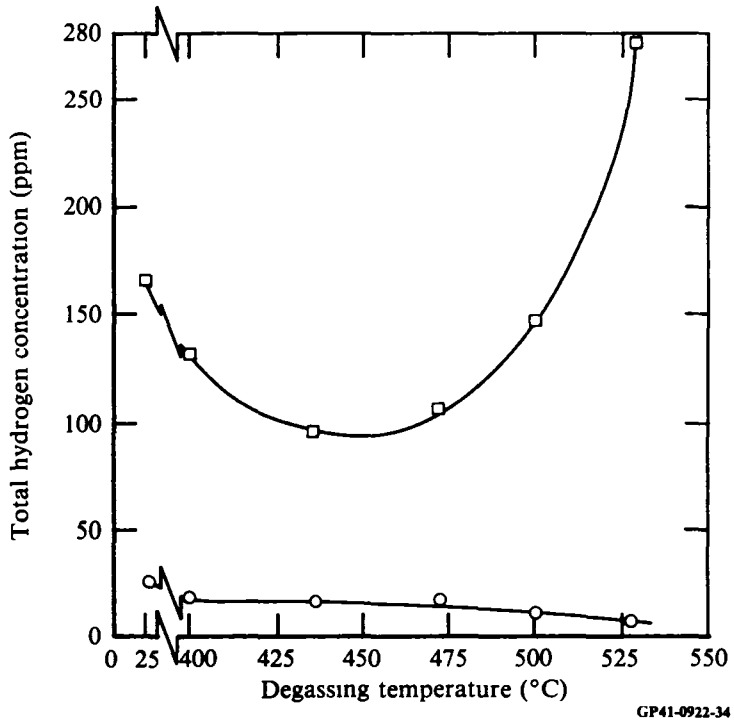

Figure 20. Variation with degassing temperature of hydrogen concentration in vacuum-atomized alloy powders: (○) Al-4.4Cu-1.5Mg-1Fe-1Ni-0.2Zr and (□) Al-3Li-1.5Cu-1Mg-0.5Co-0.2Zr.

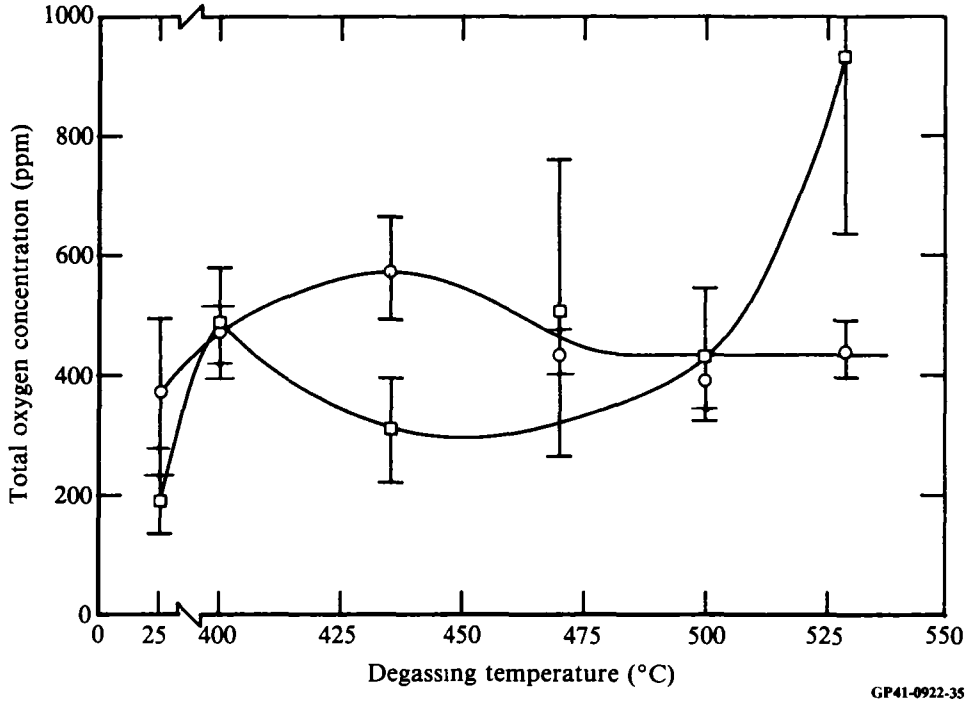

Figure 21. Variation with degassing temperature of oxygen concentration in vacuum-atomized alloy powders: (○) Al-4.4Cu-1.5Mg-1Fe-1Ni-0.2Zr and (□) Al-3Li-1.5Cu-1Mg-0.5Co-0.2Zr.

5.1.2 Oxide Layer Modification During Degassing

Depth profiles of oxide films on non-Li- and Li-containing VA particles, degassed for 2 h at 530°C, are shown in Figures 22a and 22b. Comparison of the depth profile of a degassed non-Li-containing alloy particle (Figure 22a) with that of a corresponding as-received particle (Figure 17b) shows that the oxide layer thickness has increased from about 1.7 nm to about 2.3 nm, presumably by chemical reaction of oxygen from adsorbed water vapor. This result is in agreement with the modest increase in oxygen concentration upon 530°C degassing shown in Figure 21.

The Li-containing particle shows an increase in oxide thickness upon degassing from ~ 3.5 to ~ 19 nm (compare Figure 22b with Figure 18b). This result is in agreement with the large rise in oxygen concentration in the 530°C-degassed powder shown in Figure 21. Although no Li signal was obtained in the depth profile, the greater reactivity of the Li-containing alloy is presumably the result of the high chemical affinity of Li for oxygen and the high mobility of the Li ion in diffusing through an oxide layer to the free surface to enable further oxidation. In both alloys, the oxide layer after degassing remains rich in Mg, while Cu is rejected into the matrix.

Oxygen and hydrogen concentration results and the SAM data have important implications for powder degassing. It is important, and vital in the Li-containing alloy, to remove as much adsorbed gas at as low a temperature as possible. Rapid heating of the powder to the degassing temperature results in reaction of significant amounts of adsorbed gases such as H_2O with the powders, liberating H_2 and increasing the oxide layer thickness. The resulting thick oxide layers are difficult to fracture during consolidation, thus increasing the probability of poor interparticulate bonding. Degassing cycles should thus include extensive exposure to vacuum at 25-300°C, where desorption rather than chemical reaction can be expected to occur.

5.2 Characterization of Extrusions and Forgings

5.2.1 Chemical Analyses

Chemical analyses of extrusions made from various particulate types are consistent with analyses of the corresponding powders (Tables 2 and 3), indicating little additional loss of volatile or reactive elements and negligible

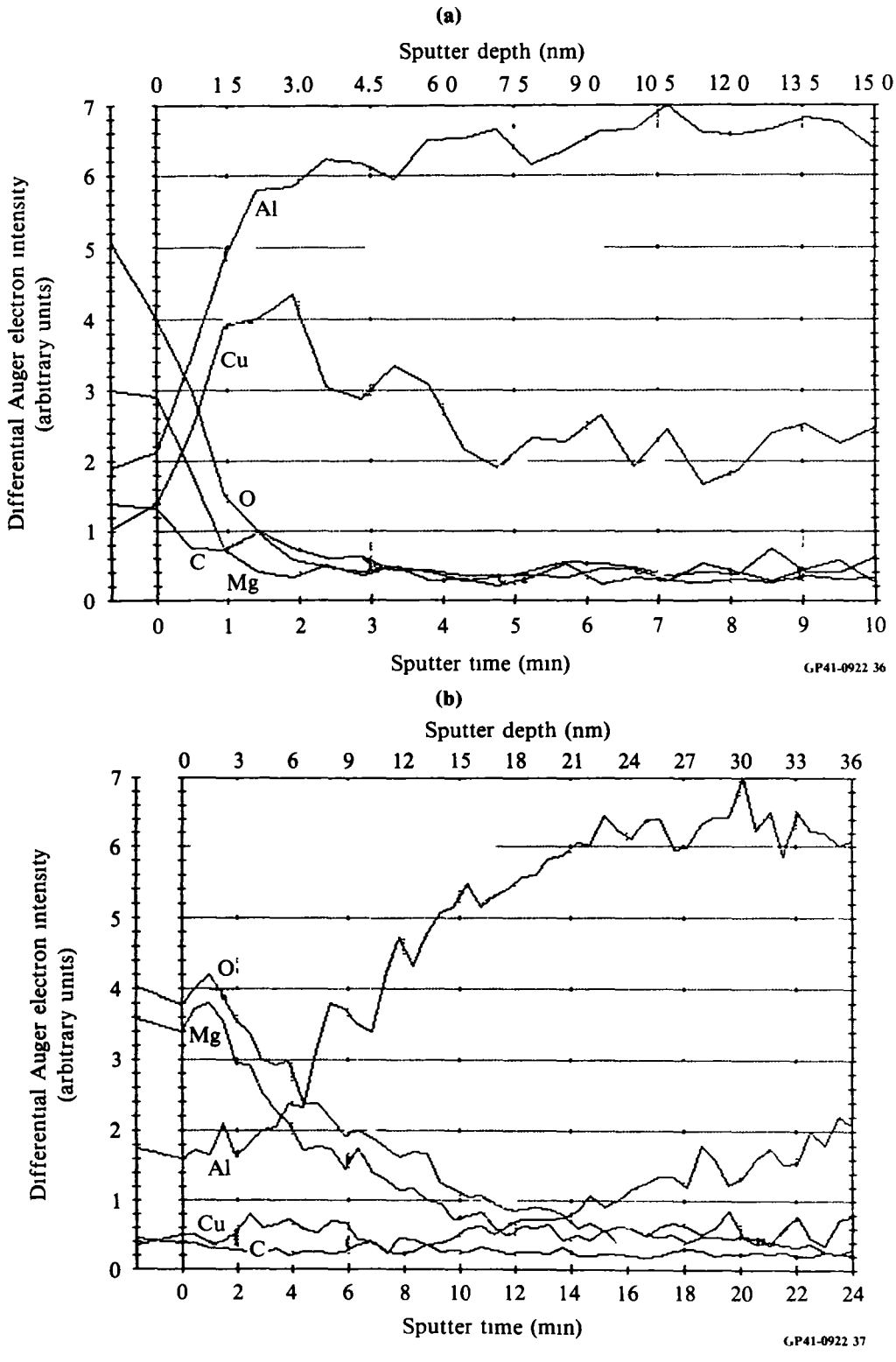

Figure 22. Depth profiles of oxide films on vacuum-atomized particles, degassed 530°C/2 h in vacuum. Sputter rate 1.5 nm/min: (a) Al-4.4Cu-1.5Mg-1Fe-1Ni-0.2Zr and (b) Al-3Li-1.5Cu-1Mg-0.5Co-0.2Zr.

introduction of impurities during the consolidation process. The chemical analyses shown in Tables 2 and 3 are thus valid for the extrusions as well as the particulates.

Hydrogen analyses of the extrusions (Table 4) show that degassing was generally efficient and reduced hydrogen concentrations to acceptable levels except in the case of the extrusion made from the USGA-He Li-containing alloy. The average particle size of the latter alloy was smaller and the weight percent of < 10-μm-diameter particles was larger (12% versus 1% for the VA and USGA-Ar powders, see Figure 7) than in any other alloy. The large surface-to-volume ratio in the USGA-He powder may have fixed larger amounts of hydrogen- and oxygen-bearing species than for other alloy powders prior to consolidation, leading in turn to larger concentrations of H and O after degassing. Oxygen contents in the extrusions were generally larger than those in the powders, suggesting that some chemical fixing of oxygen occurred during degassing. Oxygen levels were comparable to those in other RSP Al-Li alloys produced at MDRL **(21)**, and considerably lower than the typical value of 4000 ppm found in commercial 7091-Al, which is consolidated from air-atomized powder.

5.2.2 Microstructure

Optical micrographs of as-received Al-4.4Cu-1.5Mg-1Fe-1Ni-0.2Zr and Al-3Li-1.5Cu-1Mg-0.5Co-0.2Zr extrusions and forgings (Figures 23-25) show microstructural refinement with respect to I/M alloys, unrecrystallized grain structures, and microstructural features not exceeding 10 μm in diameter. Differences among microstructures of as-extruded non-Li-containing alloys (Figure 23) parallel differences in composition. The 1- to 3-μm-diameter particles commonly observed in the Al-4.4Cu-1.5Mg-1Fe-1Ni-0.2Zr VA extrusion, and occasionally observed in the USGA extrusions, are larger than the Al_9FeNi dispersoids (compare with Figure 5), and therefore must be Al_2Cu or Al_2CuMg constituent particles. The phase in equilibrium with the matrix in Al-3.94Cu-1.54Mg, the analyzed composition of the VA extrusion, is Al_2CuMg **(17)**. This phase is known to be strongly etched by Keller's reagent in 2XXX series alloys **(22)**; thus the 1- to 3-μm constituent particles are identified as Al_2CuMg. As the Mg concentration is reduced, as in the USGA extrusions and in the Al-4.4Cu-1.5Mg-2Fe-2Ni-0.2Zr extrusion, Al_2CuMg is predicted by the phase diagram **(17)** to be replaced by Al_2Cu, which is not strongly attacked by the etch

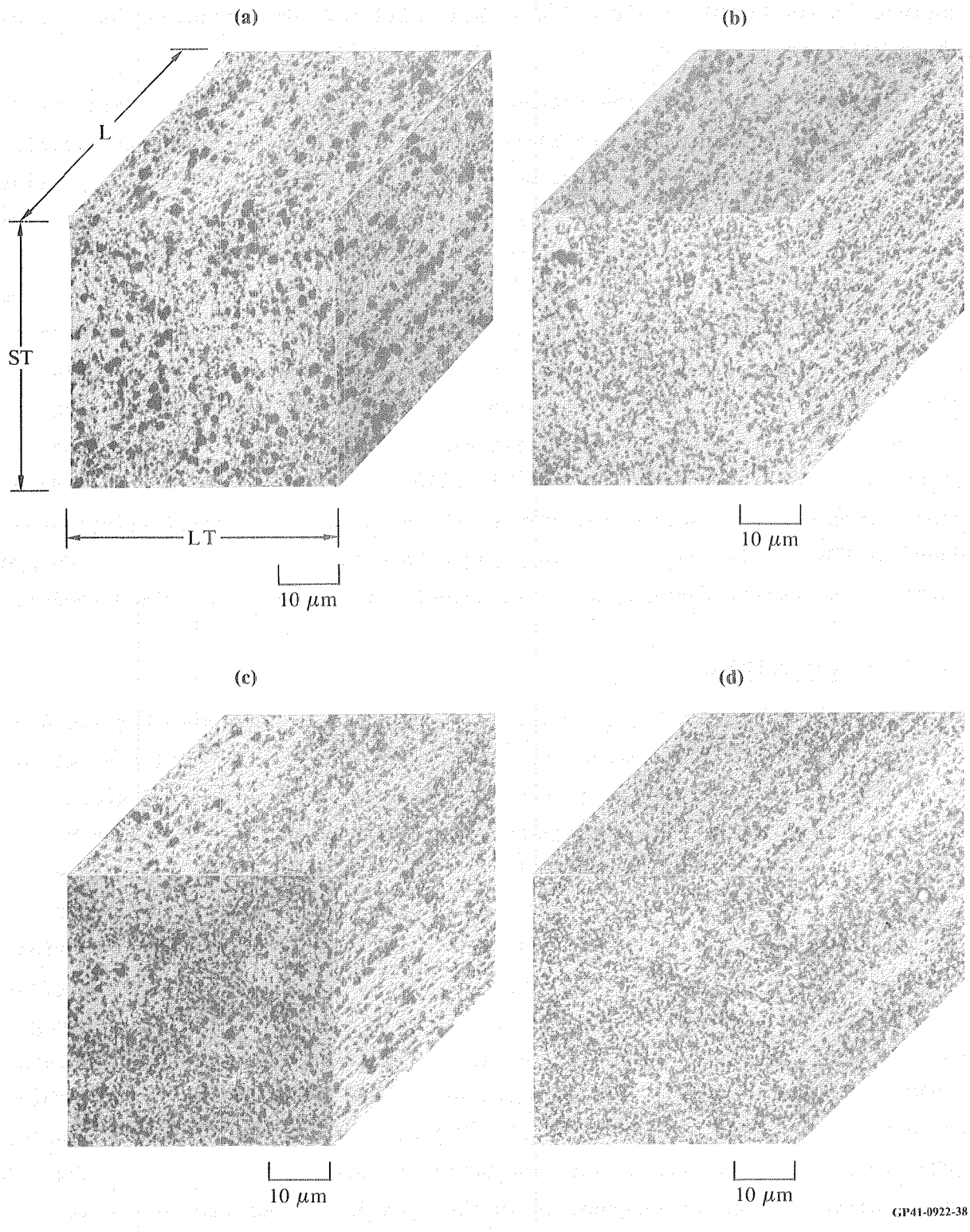

Figure 23. Optical micrographs of non-Li-containing alloy extrusions: (a)-(c) Al-4.4Cu-1.5Mg-1Fe-1Ni-0.2Zr made from (a) VA powder, (b) USGA-Ar powder, (c) USGA-He powder, (d) Al-4.4Cu-1.5Mg-2Fe-2Ni-0.2Zr made from VA powder.

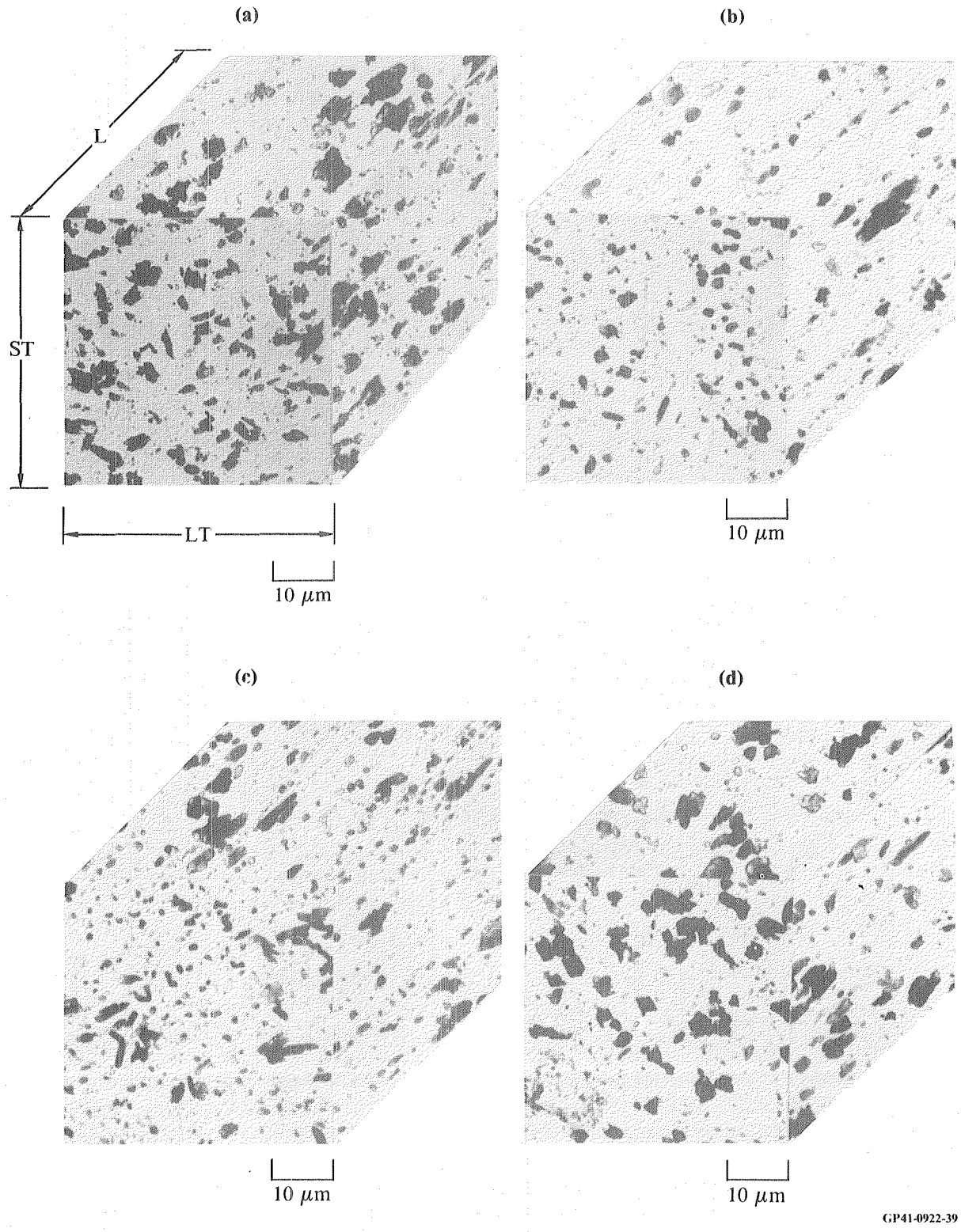

Figure 24.Optical micrographs of Al-3Li-1.5Cu-1Mg-0.5Co-0.2Zr extrusions made from (a) VA powder, (b) USGA-Ar powder, (c) USGA-He powder, and (d) RQ flakes.

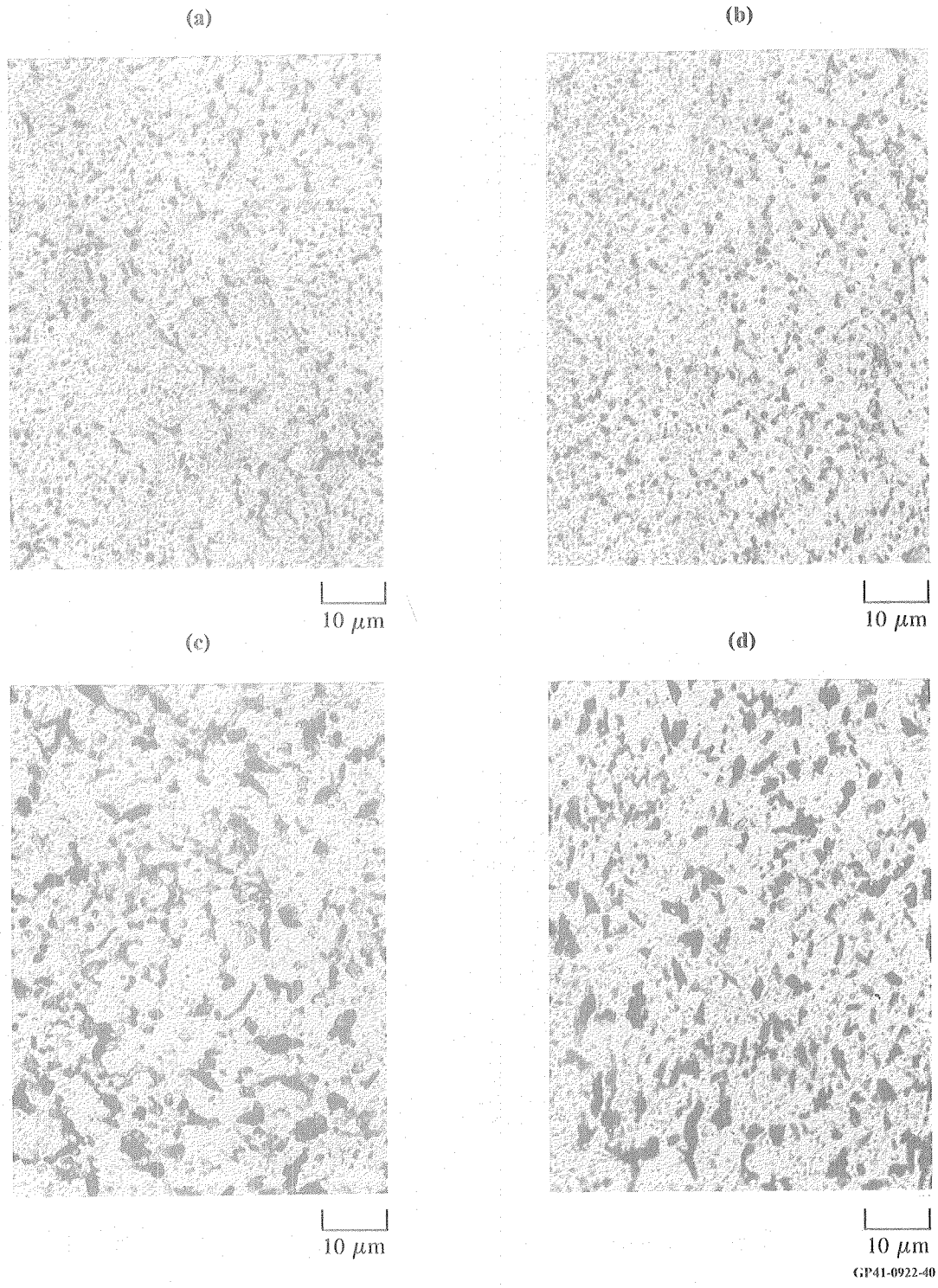

Figure 25. Optical micrographs of forgings: (a), (b) Al-4.4Cu-1.5Mg-1Fe-1Ni-0.2Zr, (a) transverse, (b) longitudinal; (c), (d) Al-3Li-1.5Cu-1Mg-0.5Co-0.2Zr, (c) transverse, (d) longitudinal.

medium and appears as smaller, outlined light particles **(22)**. These predictions are consistent with the appearance of Figures 23b-d in comparison with 23a. Finally, the Al_9FeNi dispersoids are not strongly attacked by the etch medium and appear as numerous fine, light particles in all the micrographs in Figure 23. The dispersoid density is noticeably greater in Figure 23d, consistent with the larger volume fraction of dispersoids in the 2Fe-2Ni alloy.

Major microstructural features of as-extruded Al-3Li-1.5Cu-1Mg-0.5Co-0.2Zr are 3- to 8-μm-diameter, jagged constituent particles (Figure 24). The phases in equilibrium with the matrix for the overall composition Al-3Li-1.5Cu are δ (AlLi) and T_2 (Al_5Li_3Cu). Prior experience at MDRL **(20)** has shown that δ is not strongly attacked by the Keller's reagent used to etch the metallographic samples, so the dark constituent particles here are probably T_2. The USGA extrusions contain 2.7Li and 0.7Mg and should therefore have smaller volume fractions of Al-Li-Cu-Mg constituent phases than the VA or RQ extrusions, which contain 3Li and 1Mg. Comparing Figures 24b and 24c with 24a and 24d shows this to be the case. The smaller particles, which are not strongly etched, may be Al_9Co_2 dispersoids, or in the case of dispersoids along prior particulate boundaries (e.g., longitudinal sections of Figures 24b and 24c), may be oxides.

Optical micrographs of forgings (Figure 25) resemble those of the corresponding VA extrusions except for the weaker texture. Distributions of constituent particles reflect prior segregation within individual particles. The non-Li-containing forging shows particle-to-particle variation of concentration of fine, lightly etched dispersoids, probably Al_9FeNi (Figures 25a and 25b).

5.2.3 Texture

Figures 26-28 show {111} pole figures of extrusions and forgings. Pole figures of extrusions are typical of a hot-worked material which is fully recovered but not recrystallized. The forgings have a weaker fiber texture typical of axisymmetric deformation.

The pole figure of the Al-4.4Cu-1.5Mg-1Fe-1Ni-0.2Zr VA extrusion (Figure 26a) is also typical of the USGA extrusions. As the subgrain size decreases and the subgrain density increases in a fully-recovered microstructure of this type, the variation in subgrain orientation from those

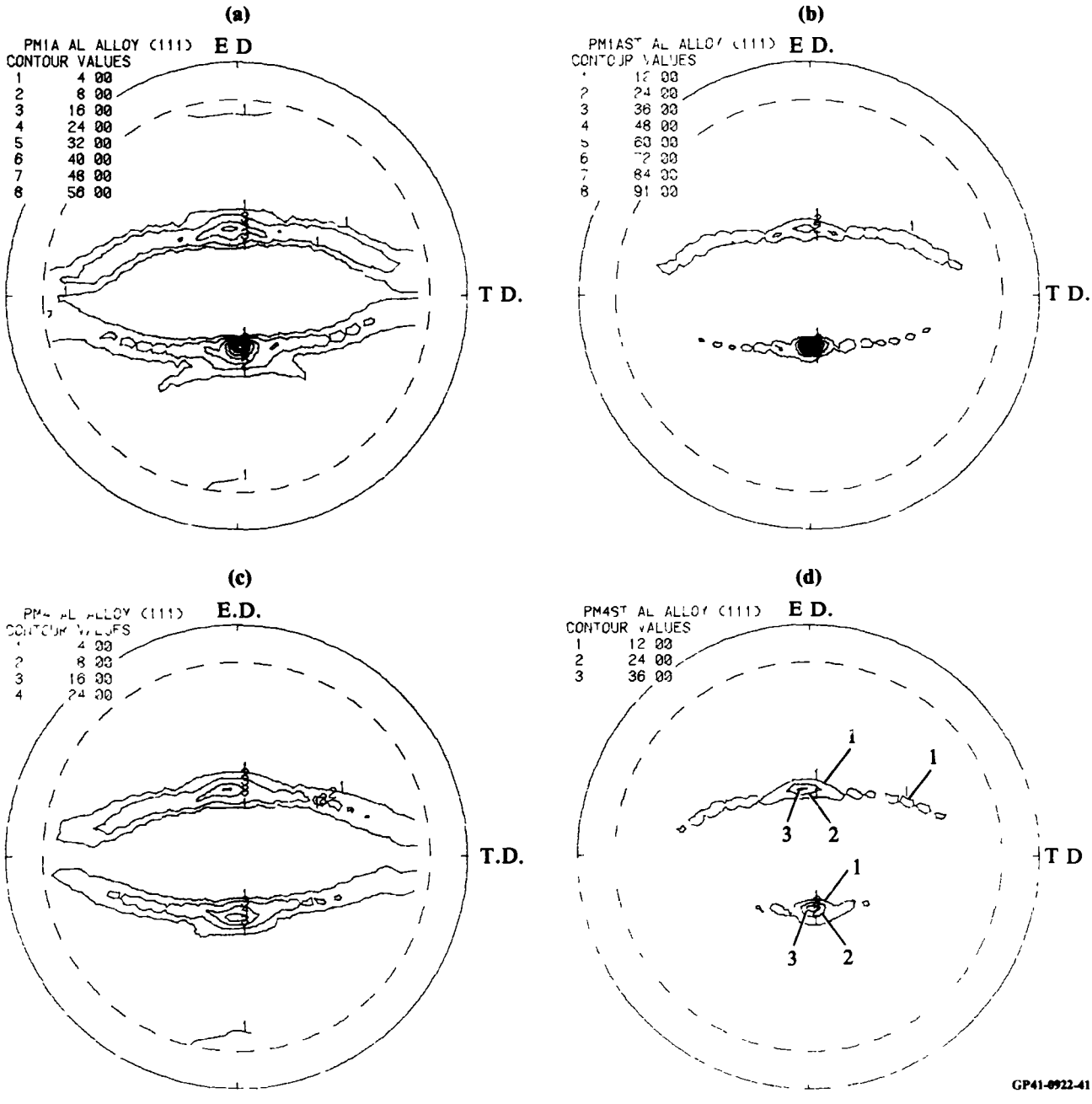

Figure 26. (111) pole figures of VA extrusions: (a), (b) Al-4.4Cu-1.5Mg-1Fe-1Ni-0.2Zr, (a) as-extruded, (b) solution-treated 530°C/1 h; (c), (d) Al-4.4Cu-1.5Mg-2Fe-2Ni, (c) as-extruded, (d) solution-treated 530°C/1 h.

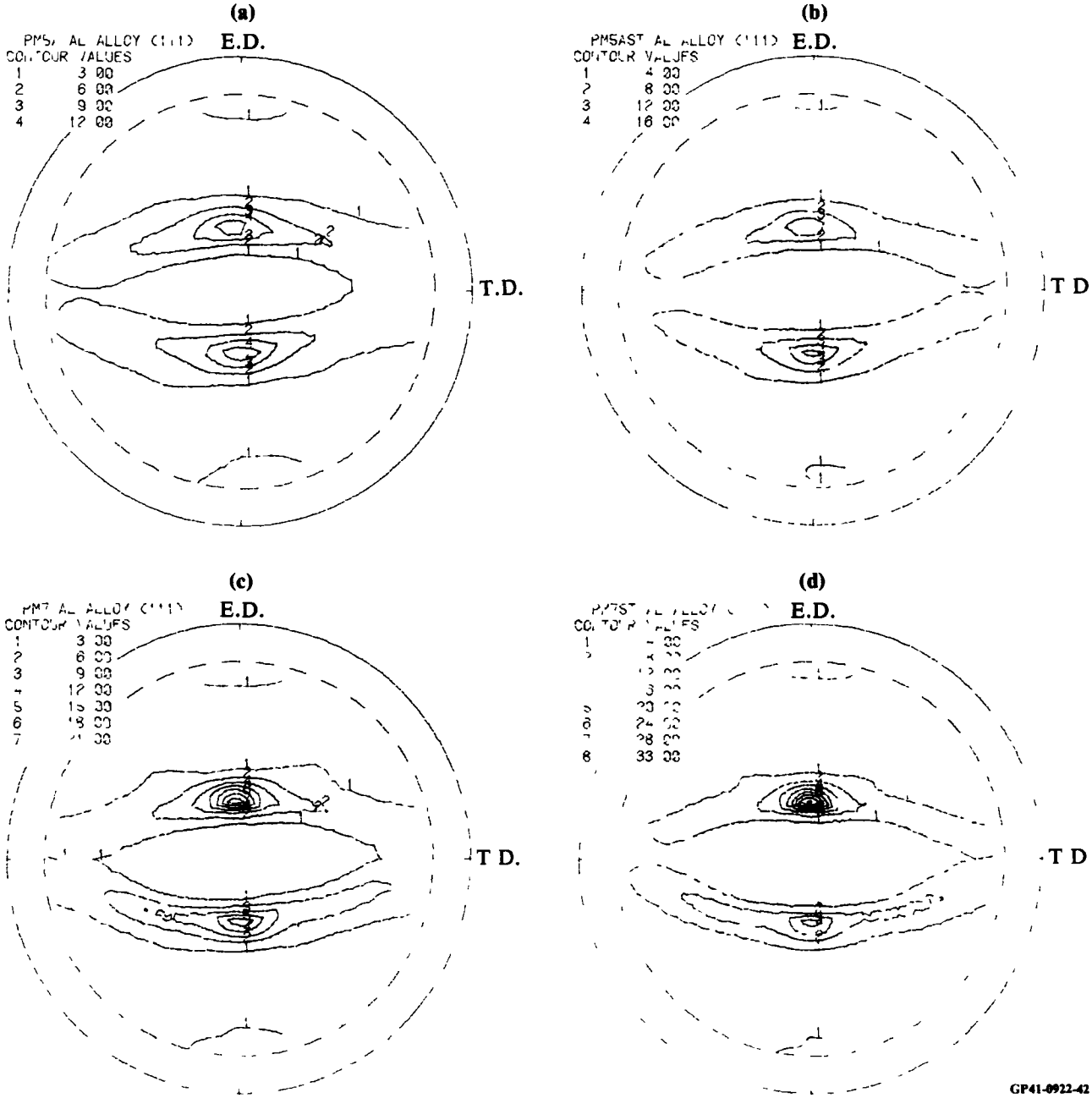

Figure 27. (111) pole figures of Al-3Li-1.5Cu-1Mg-0.5Co-0.2Zr extrusions: (a), (b) VA extrusion, (a) as-extruded, (b) solution-treated 530°C/1 h; (c), (d) USGA-He extrusion, (c) as-extruded, (d) solution-treated 530°C/1 h.

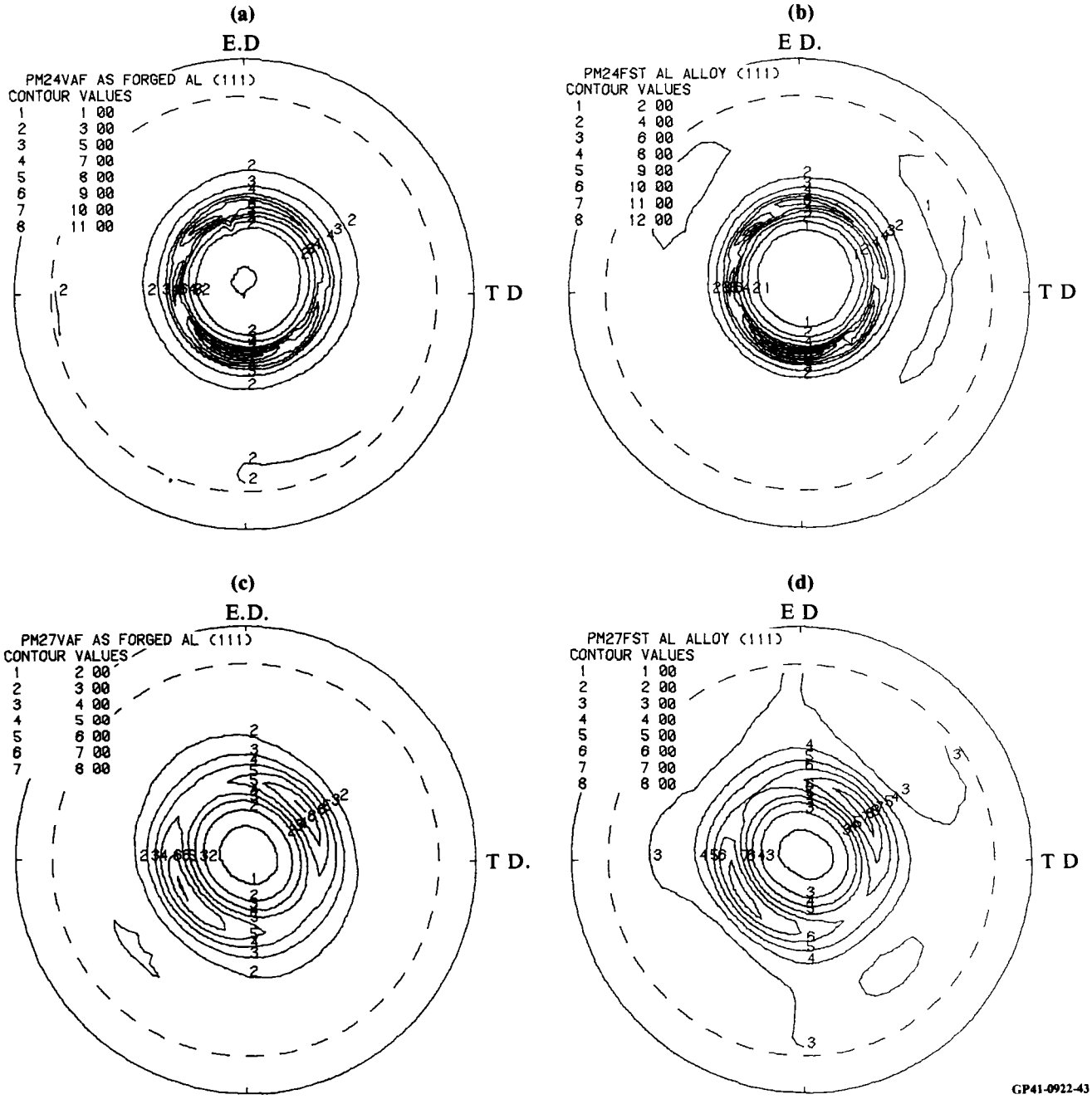

Figure 28. (111) pole figures of forgings: (a), (b) Al-4.4Cu-1.5Mg-1Fe-1Ni-0.2Zr, (a) as-forged, (b) solution-treated 530°C/1 h; (c), (d) Al-3Li-1.5Cu-1Mg-0.5Co-0.2Zr, (c) as-forged, (d) solution-treated 530°C/1 h.

orientations typical of the extrusion increases, and the maximum pole density or X-ray intensity decreases. The texture of the Al-4.4Cu-1.5Mg-2Fe-2Ni-0.2Zr alloy (Figure 26c) is relatively diffuse, suggesting that the larger density of Al_9FeNi dispersoids stabilizes a finer substructure than in the 1Fe-1Ni extrusions.

Pole figures of the Al-3Li-1.5Cu-1Mg-0.5Co-0.2Zr extrusions (Figure 27) resemble those in Figure 26, but the maximum intensity is smaller, indicating a smaller subgrain size and a larger variation in subgrain orientation. The general appearance of the pole figures is also typical of USGA-Ar and RQ extensions, showing that the as-extruded subgrain microstructure is influenced primarily by extrusion parameters and not by particulate type.

Pole figures of the forgings (Figure 28) all show weak textures resulting from the relatively small deformations required to produce the forgings. The texture in the Al-4.4Cu-1.5Mg-1Fe-1Ni-0.2Zr forging is somewhat sharper than that in the Al-3Li-1.5Cu-1Mg-0.5Co-0.2Zr forging.

5.3 Heat Treatment of Extrusions and Forgings

Aging curves of all extrusions, solution treated and aged at various temperatures, are shown in Figures 29-31. Two solution-treatment temperatures were chosen for each alloy: the estimated highest safe temperature, and a temperature 30°C lower. Hardness curves were obtained for 190°C aging of the non-Li-containing alloys and 177°C aging of the Li-containing alloy. The aging behavior of forgings was assumed to resemble that of VA extrusions.

The non-Li-containing VA extrusions attain maximum hardness in 8 to 16 h at 190°C as expected, followed by a sharp decrease (Figure 29). Increasing the solution-treatment temperature of Al-4.4Cu-1.5Mg-1Fe-1Ni-0.2Zr from 500 to 530°C solutionizes larger amounts of Cu and Mg, permitting a larger density of strengthening precipitates and increasing the hardness. The effect of increasing the dispersoid-forming element addition from 1Fe-1Ni to 2Fe-2Ni is to increase the hardness by 6 to 7 Rockwell B (RB) points. Aging curves of USGA extrusions are similar to those in Figure 29, but peak hardnesses are 72 to 74 RB, compared with 81 RB for the VA extrusion, probably as a result of the lower Mg content in the VA extrusions and the resulting lower volume fraction of Al-Cu-(Mg) precipitates. No variations in hardness or aging behavior traceable to particulate type were noted.

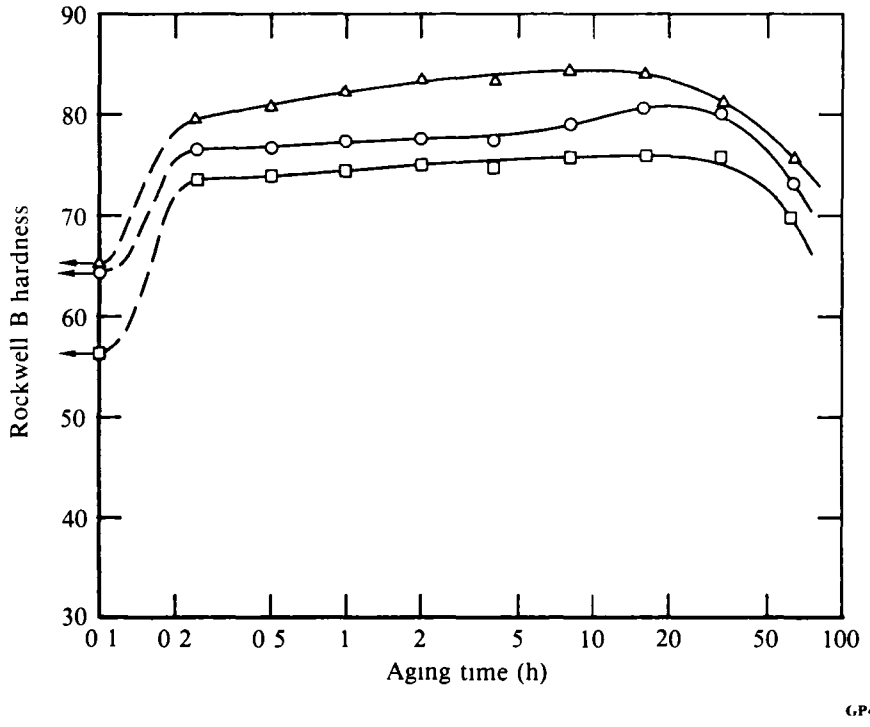

Figure 29. Aging behavior at 190°C of non-Li-containing VA extrusions: (○, □) Al-4.4Cu-1.5Mg-1Fe-1Ni-0.2Zr; (○) solution-treated 530°C/1 h, (□) solution-treated 500°C/1 h, (△) Al-4.4Cu-1.5Mg-2Fe-2Ni-0.2 Zr, solution-treated 530°C/1 h.

Figures 30 and 31 show typical aging behavior of the Al-3Li-1.5Cu-1Mg-0.5Co-0.2Zr extrusions. Hardness curves of samples previously solution treated at 530 and 560°C were virtually identical for each particulate type. Peak hardness was uniformly reached in 8 to 16 h, and little variation in hardness was noted in the vicinity of the maximum. The peak-aged hardness of VA and RQ extrusions, which contained 3Li-1Mg, was 87 to 88 RB (Figure 30); while those of USGA extrusions, which contained 2.7Li-0.6Mg, was 83-85 RB (Figure 31). These results suggest that the ultimate tensile strengths of the VA and RQ extrusions as peak aged should be somewhat higher than those of USGA extrusions.

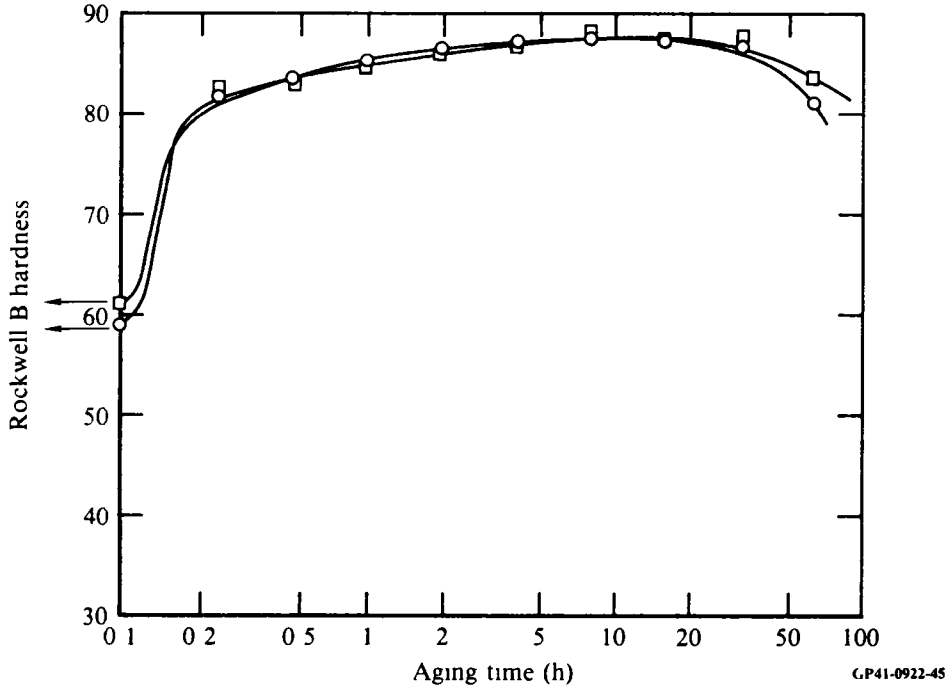

Figure 30. Aging behavior at 177°C of Al-3Li-1.5Cu-1Mg-0.5Co-0.2Zr VA extrusions, solution-treated at (○) 530°C/1 h and (□) 560°C/1 h.

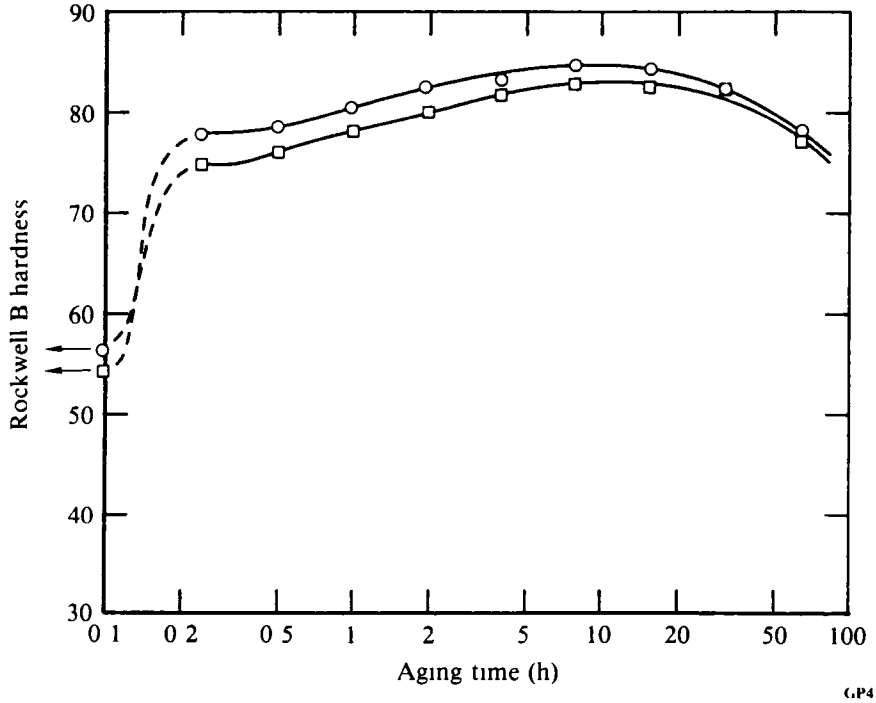

Figure 31. Aging behavior at 177°C of Al-3Li-1.5Cu-1Mg-0.5Co-0.2Zr USGA-He extrusions: (○) solution-treated 530°C/1 h and (□) solution-treated 560°C/1 h.

6. TASK 3: MICROSTRUCTURE AND PROPERTIES OF CONSOLIDATED FORMS

6.1 Microstructure

6.1.1 Solution-Treated Condition

Optical micrographs of non-Li-containing alloy extrusions and forgings, solution treated at 500 and 530°C, are shown in Figures 32-34. In accord with the Al-Cu-Mg phase diagram **(17)**, the Al_2CuMg and Al_2Cu constituent particles visible in the extrusions (Figure 23) have dissolved, except in the Al-4.4Cu-1.5Mg-1Fe-1Ni-0.2Zr extrusion solution treated at 500°C (Figure 32b). The extrusions have not recrystallized, and show a pronounced "pancake" grain structure. The Al_9FeNi dispersoids are present in greater density in the 2Fe-2Ni alloy (Figure 32c) than in the 1Fe-1Ni alloy. Minor microstructural differences are attributable to compositional variations rather than differences in particulate type. The forging (Figure 34a) shows evidence of prior particulate boundaries and an unrecrystallized grain structure, as in the as-received condition.

Optical micrographs of Li-containing alloy extrusions and forgings, solution treated at 530 and 560°C, are shown in Figures 34-36. The Al-Li-Cu phase diagram **(17)** predicts that 2.7Li-1.5Cu (the actual composition of USGA extrusions) should be almost completely dissolved at 530°C, while 3Li-1.5Cu (the actual composition of VA and RQ extrusions) should be dissolved at 560°C. The appearance and volume fractions of Al-Li-Cu-(Mg) constituent particles in Figures 34-36 are in accord with these predictions and the chemical analyses (Table 3). The concentrations of Li, Cu, and Mg in solid solution, and hence available for precipitation, are greater for the VA and RQ extrusions than for USGA extrusions (Section 4.3.1), particularly after 560°C solution treatment. Thus, it is expected that the former extrusions will be stronger and have a greater variation of strength with prior solution-treatment temperature than the latter.

Also visible in the extrusions are fine, lightly etched particles on (highly distorted) prior particulate boundaries, most of which must be oxides. They are less numerous in the RQ extrusion (Figures 35d and 36d) than in the other extrusions, in accord with the smaller particulate surface area and lower oxygen content of this extrusion (Table 4). Some of the lightly etched

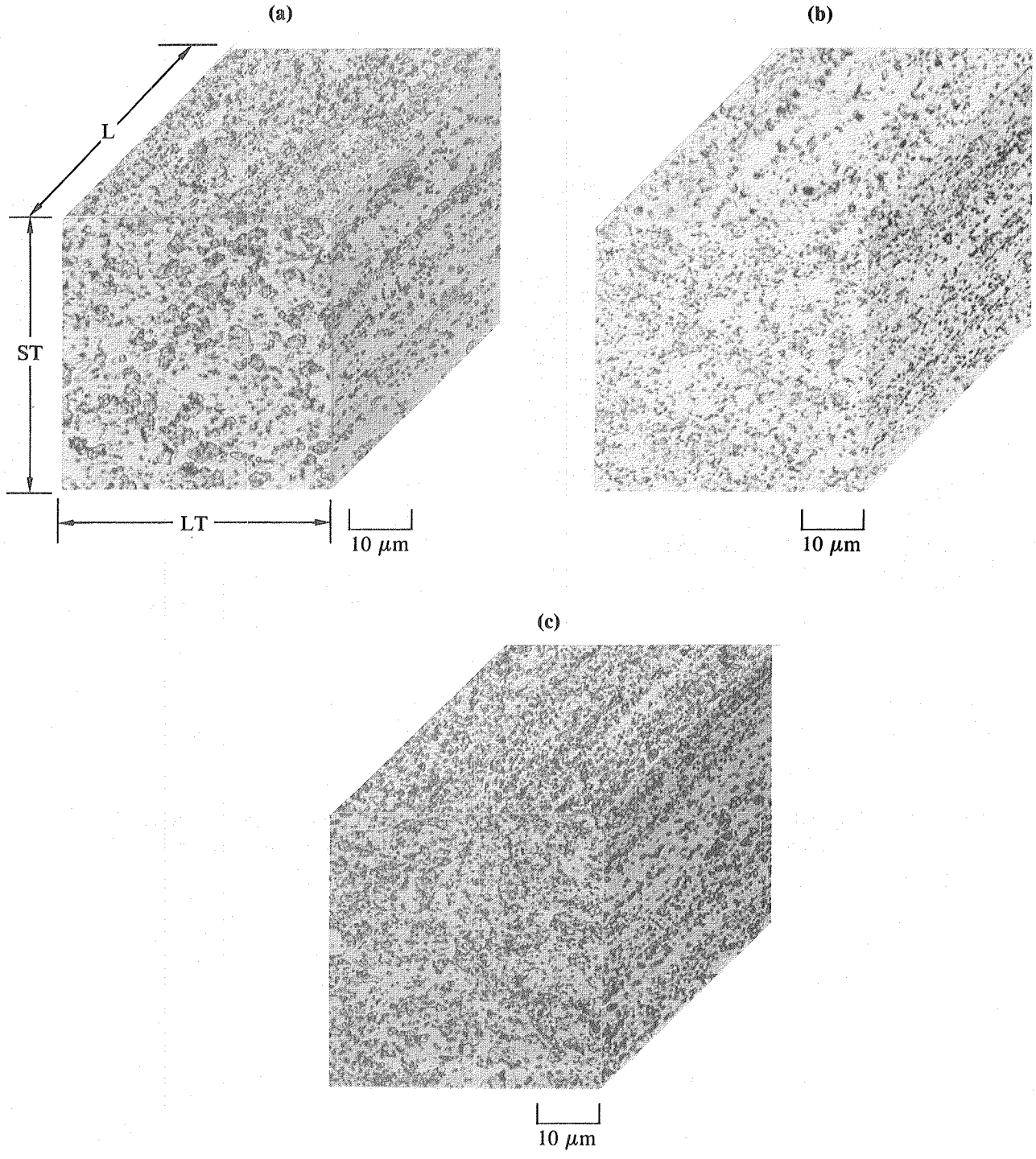

Figure 32. Optical micrographs of solution-treated extrusions: (a), (b) Al-4.4Cu-1.5Mg-1Fe-1Ni-0.2Zr, (a) 530°C/1 h, (b) 500°C/1 h; (c) Al-4.4Cu-1.5Mg-2Fe-2Ni-0.2Zr, 530°C/1 h.

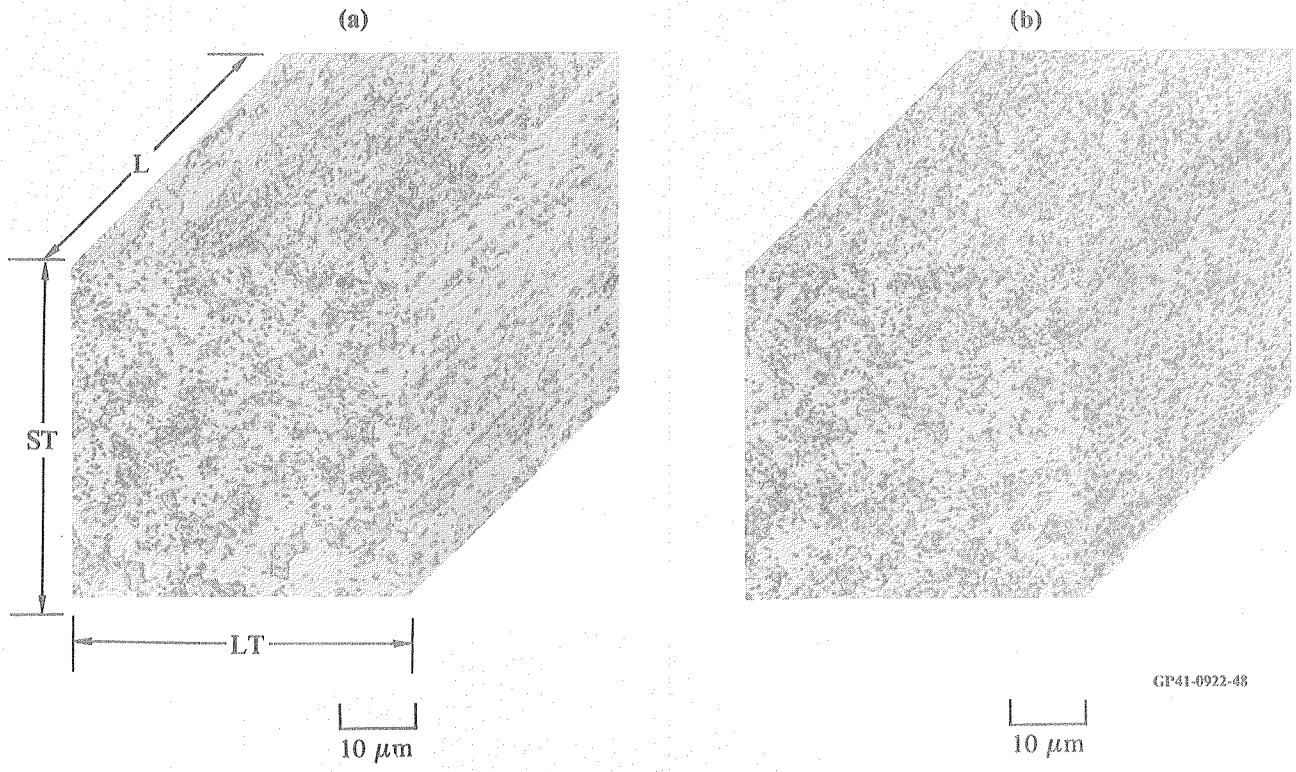

Figure 33. Optical micrographs of Al-4.4Cu-1.5Mg-1Fe-1Ni-0.2Zr extrusions from powders ultrasonically atomized in (a) argon, (b) helium, and solution-treated 530°C/1 h.

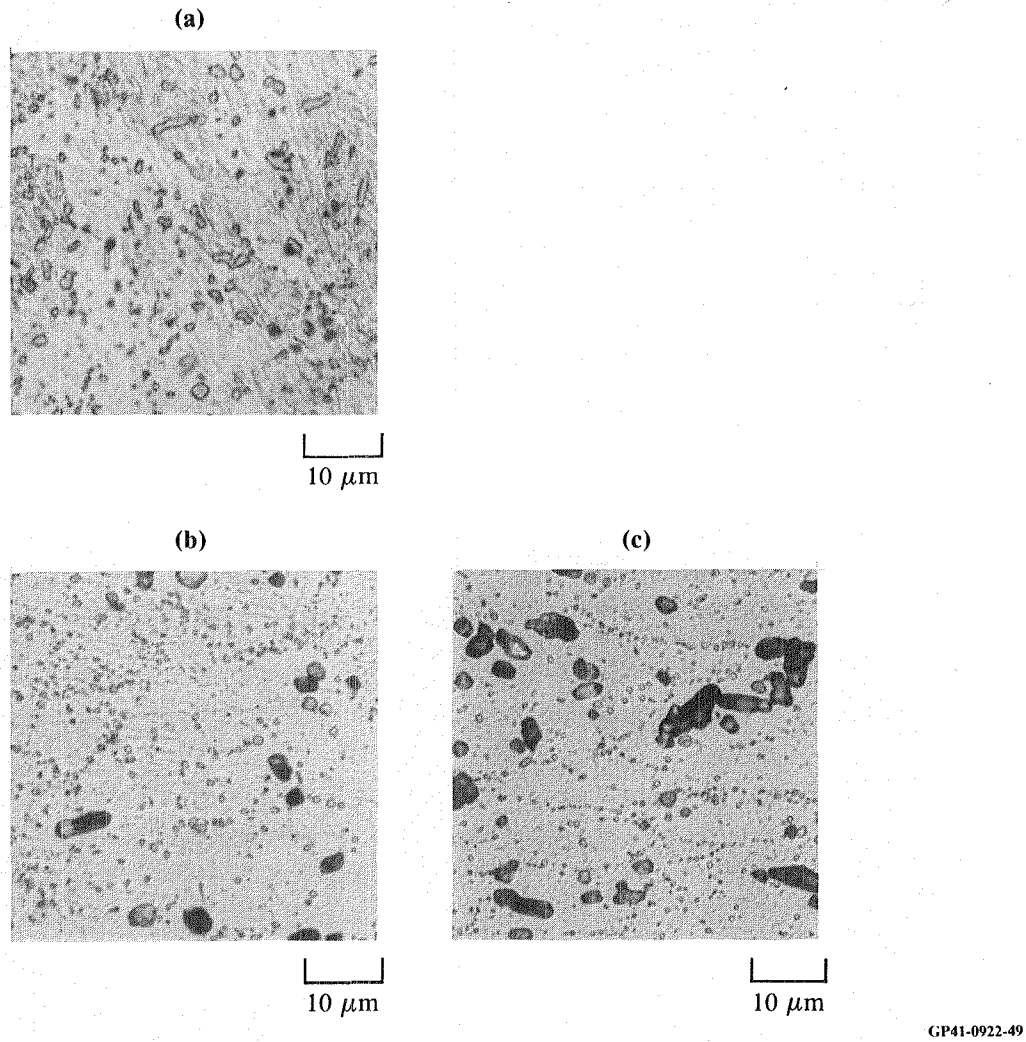

Figure 34. Optical micrographs of forgings; solution-annealed 530°C/1h: (a) Al-4.4Cu-1.5Mg-1Fe-1Ni-0.2Zr, perpendicular to forgings direction, (b), (c) Al-3Li-1.5Cu-1Mg-0.5Co-0.2Zr, (b) perpendicular to forging direction and (c) parallel to forging direction.

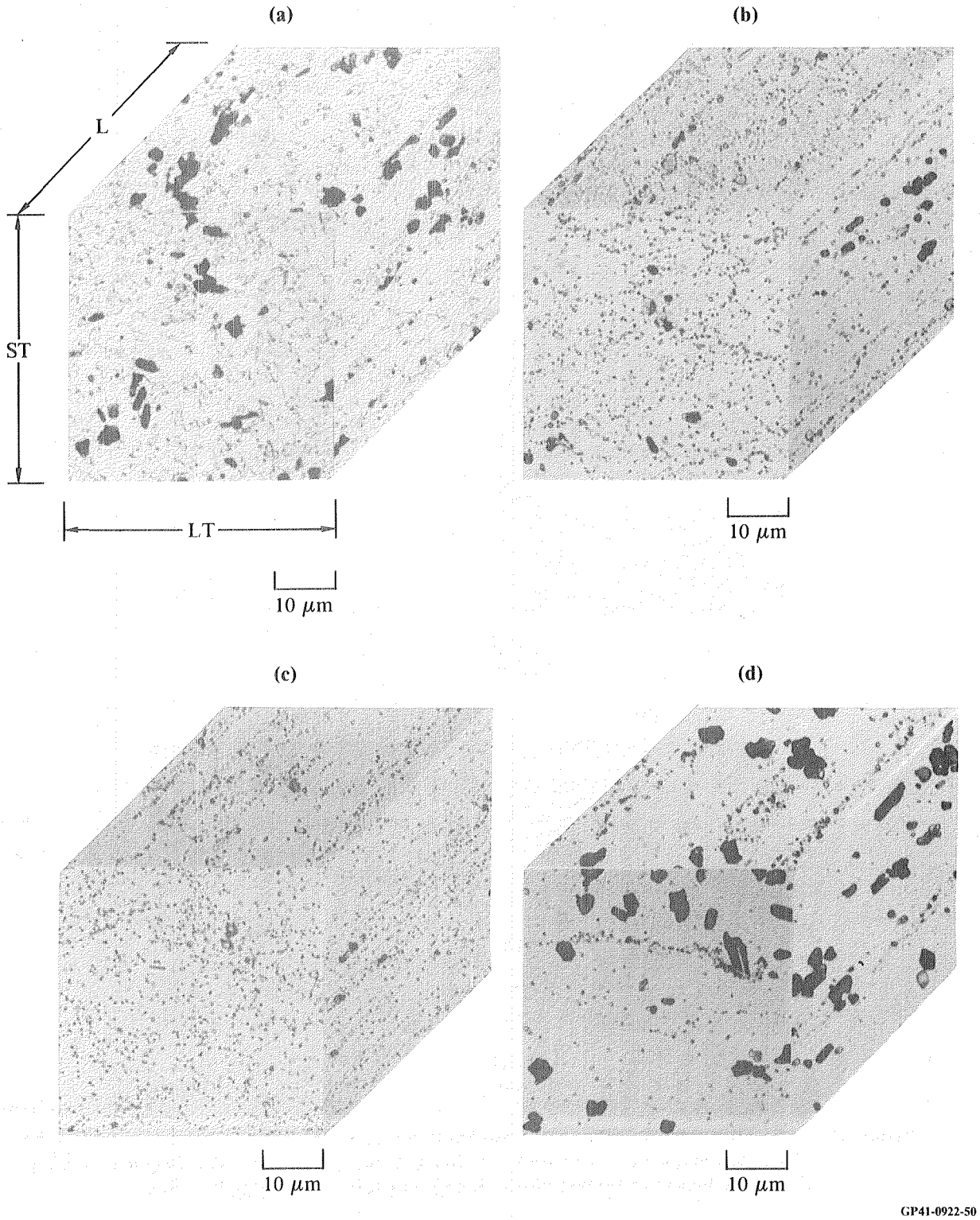

Figure 35. Optical micrographs of Al-3Li-1.5Cu-1Mg-0.5Co-0.2Zr extrusions, solution-treated 530°C/1 h, prepared from (a) vacuum-atomized powder, (b) argon ultrasonically atomized powder, (c) helium ultrasonically atomized powder, and (d) roller-quenched flakes.

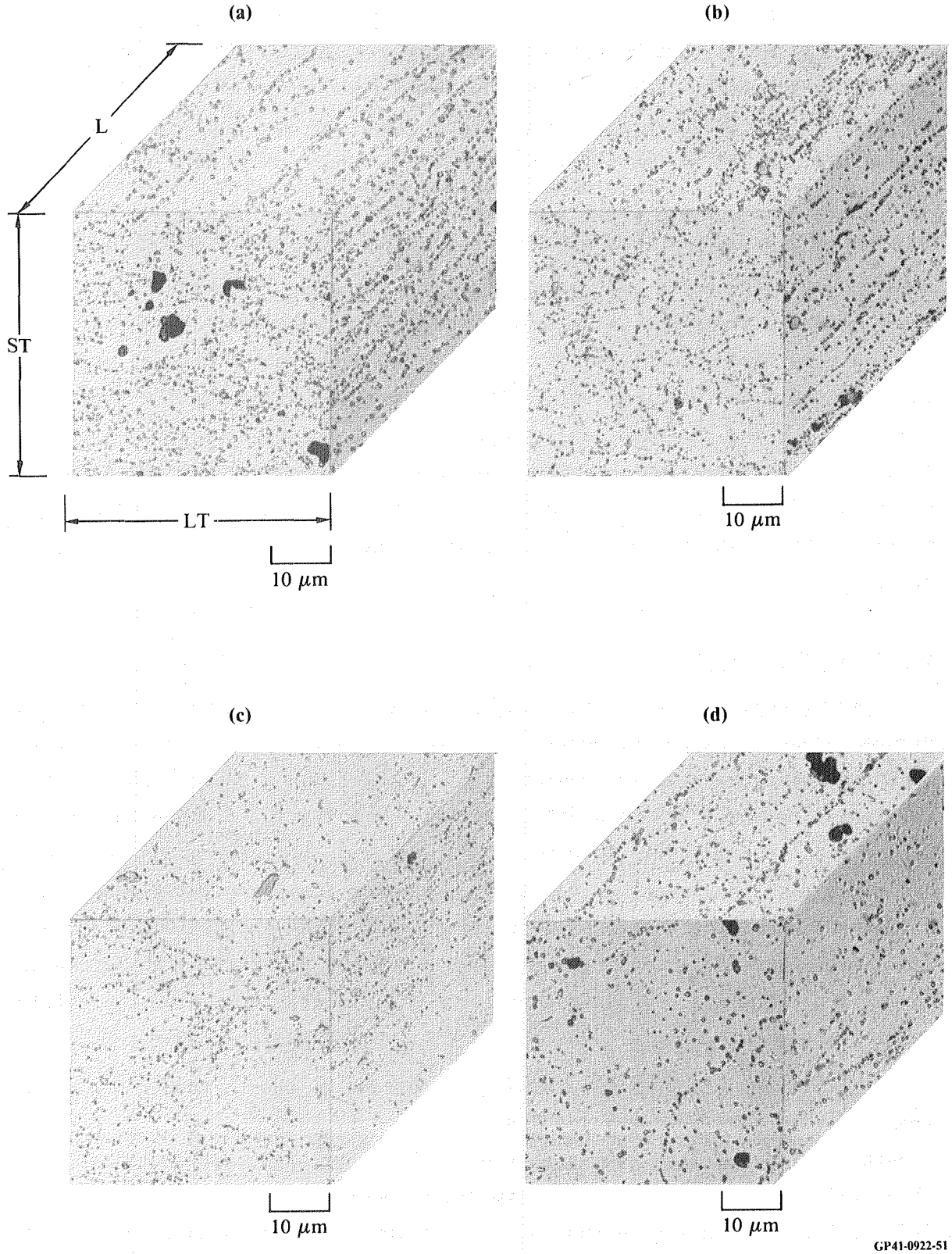

Figure 36. Optical micrographs of Al-3Li-1.5Cu-1Mg-0.5Co-0.2Zr extrusions, solution-treated 560°C/1 h, prepared from (a) vacuum-atomized powder, (b) argon ultrasonically atomized powder, (c) helium ultrasonically atomized powder, and (d) roller-quenched flakes.

particles at prior particulate boundaries may be Al_9Co_2 dispersoids. The Li-containing forging (Figure 34b) shows constituent particles and oxides similar to those in the extrusions. Former powder particle boundaries are outlined by oxides as a result of the smaller degree of deformation in the forging than in the extrusions.

Typical {111} pole figures of solution-treated extrusions and forgings are shown in Figures 26-28. None of the consolidated forms has recrystallized after solution treatment, consistent with the microstructural observations, and the pole figures are still typical of the extrusion or forging processes. The textures have sharpened noticeably compared with those in the consolidated forms, indicating subgrain coalescence and motion of high-energy subboundaries during solution-treatment. Texture sharpening is particularly noticeable in the Al-4.4Cu-1.5Mg-1Fe-1Ni-0.2Zr extrusion (compare Figures 26a and 26b), and in the Al-3Li-1.5Cu-1Mg-0.5Co-0.2Zr USGA-He extrusion (compare Figures 27c and 27d).

6.1.2 Aged Condition

TEM micrographs of variously aged extrusions and forgings are shown in Figures 37-40. The non-Li-containing alloy extrusions (Figures 37-39) have modified mosaic structures consisting of 1.8- to 2.5- x 3- to 4-μm, unrecrystallized subgrains. The Al_9FeNi dispersoids are fairly homogeneously dispersed and typically 0.4- to 0.5-μm in diameter. Subgrain boundaries are decorated with incoherent θ (Al_2Cu) precipitates in artificially aged samples. All extrusion microstructures are similar, regardless of particulate type (compare Figures 37a-c and Figures 38a-b), further confirming that microstructures of aged alloys are not dependent on the microstructures of the original particulates.

Micrographs of non-Li-containing extrusions in the T6 temper (solution treated at 530°C/1 h + aged 190°C/8 h, Figure 37) show coarse (1 μm in length) θ′ precipitates, owing to the small number of nucleation sites for this semi-coherent phase. The microstructure of the 2Fe-2Ni alloy (Figure 37d) is similar to that of the 1Fe-1Ni alloy (Figures 37a-c), the added Fe+Ni being accommodated by an increase in the density of Al_9FeNi dispersoids.

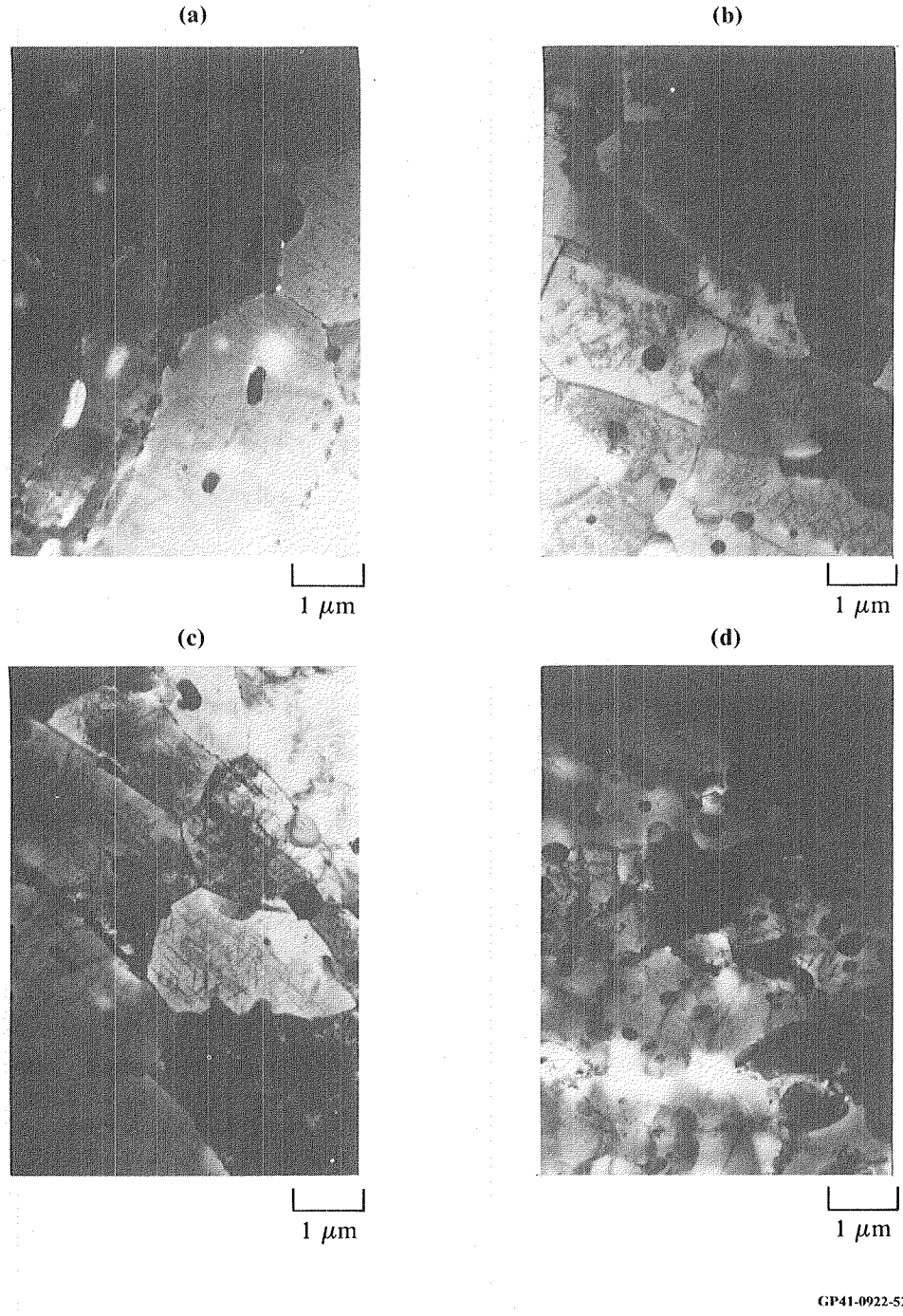

Figure 37. TEM micrographs of non-Li containing extrusions, T6 temper (solution-treated 530°C/1 h + aged 190°C/8 h): (a) - (c) Al-4.4Cu-1.5Mg-1Fe-1Ni-0.2Zr from (a) vacuum atomized powder, (b) argon ultrasonically atomized powder, (c) helium ultrasonically atomized powder; (d) Al-4.4Cu-1.5Mg-2Fe-2Ni-0.2Zr from vacuum atomized powder.

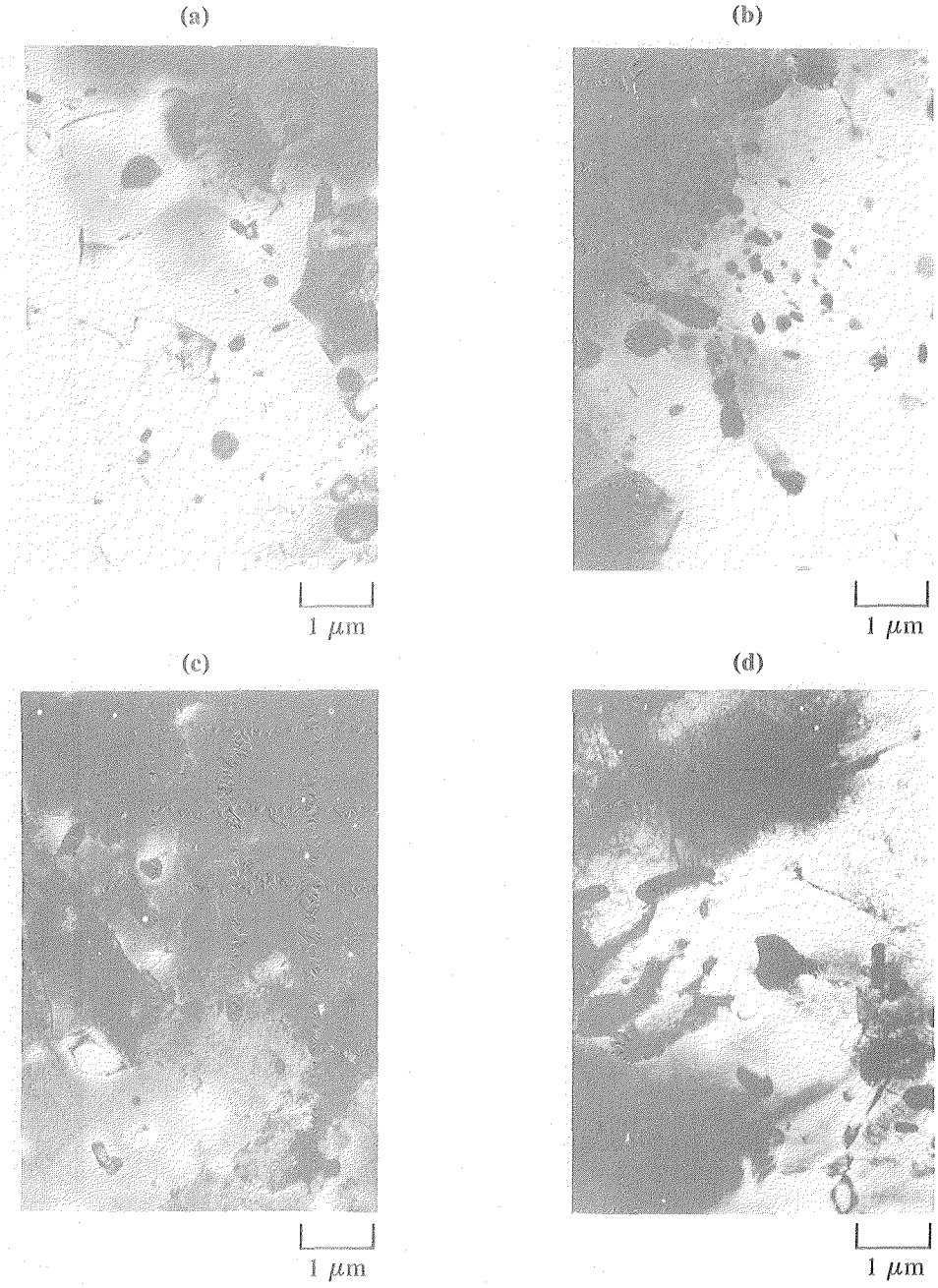

Figure 38.TEM micrographs of Al-4.4Cu-1.5Mg-1Fe-1Ni-0.2Zr extrusions and forgings: (a), (b) extrusion, vacuum atomized powder: (a) T351 temper (solution-treated 530°C/1 h + 2% stretch + aged 25°C/168 h), (b) T851 temper (solution-treated 530°C/1 h + 2% stretch + aged 190°C/8 h); (c) extrusion, argon ultrasonically atomized powder, T851 temper; (d) forging, vacuum atomized powder, T851 temper.

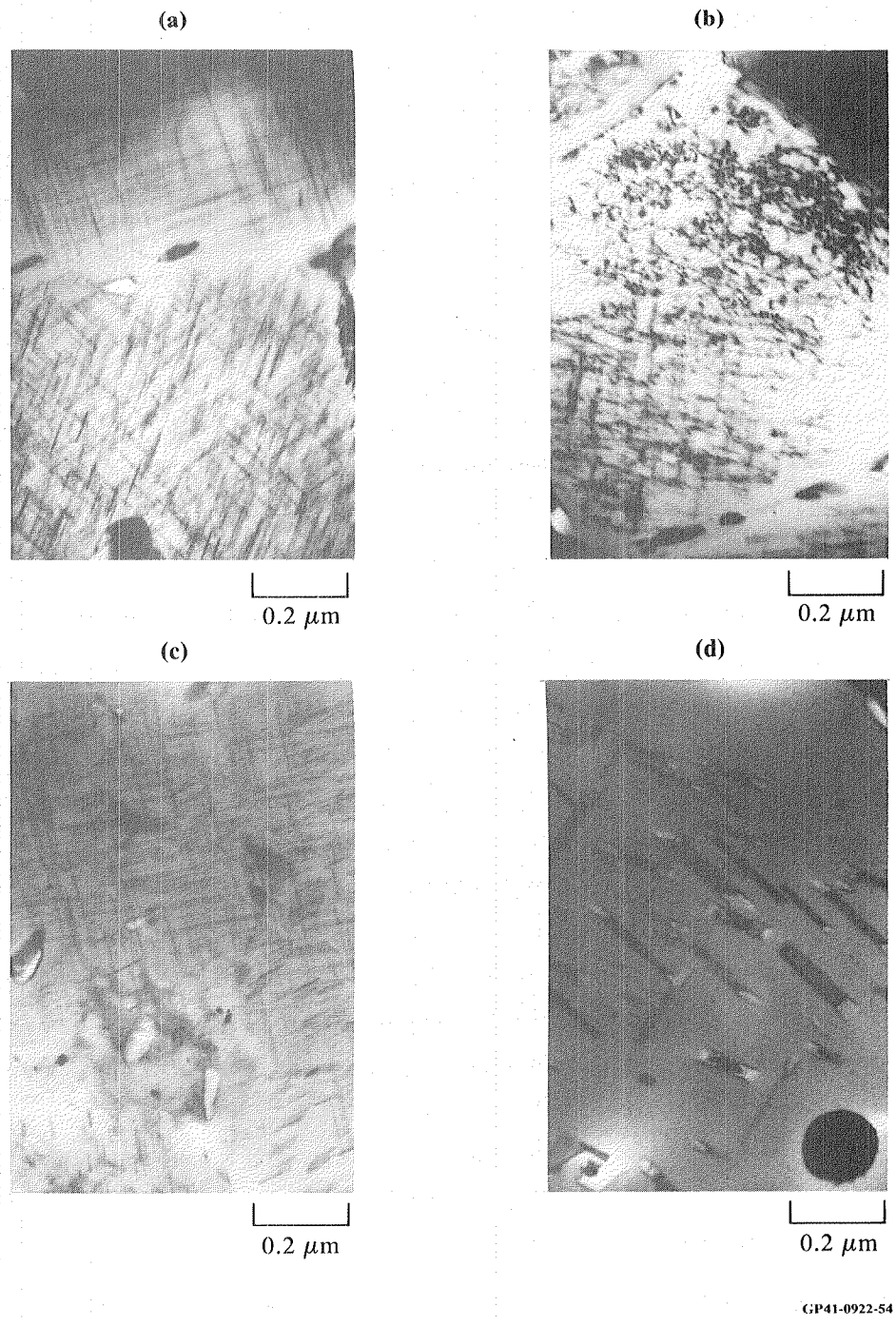

Figure 39. TEM micrographs of Al-4.4Cu-1.5Mg-1Fe-1Ni-0.2Zr VA extrusions, T851 temper, exposed for 100 h at (a) 25°C, (b) 150°C, (c) 204°C, and (d) 260°C.

Microstructures of non-Li-containing extrusions and forgings in the T851 (solution treated at 530°C/1 h + 2% stretch + 190°C/8 h) and T351 (solution treated at 530°C/1 h + 2% stretch + 25°C/168 h) tempers are shown in Figure 38. Guinier-Preston (GP1) zones in the naturally aged alloy are too small to be imaged in Figure 38a. The effect of inserting a 2% stretch between solution treatment and aging is to refine and increase the density and homogeneity of θ′ precipitates (compare Figures 38b-c with 37a-b, respectively). The increase in precipitate density is expected to produce a substantial increase in strength in the T851 temper, compared with T6. The forging microstructure (Figure 38d) is similar to that of the extrusions except for the uniform 4- to 5-μm subgrain diameter, compared with 2- to 3-μm in the extrusions.

High-magnification micrographs of Al-4.4Cu-1.5Mg-1Fe-1Ni-0.2Zr VA extrusions, T851 temper, exposed to 150, 204, and 260°C for 100 h, are shown in Figure 39. Exposure to 150°C/100 h (Figure 39b) has little effect on precipitate size, but promotes growth of subgrain-boundary θ and formation of a PFZ ~ 0.2 μm wide. After 100 h at 204°C, θ plates (thicker plates in Figure 39c) have begun to form at the expense of θ′. As the temperature is raised, these plates grow faster with concomitant dissolution of θ′, until after 100 h at 260°C only coarse θ plates are visible. Microstructural changes with increasing exposure temperature suggest that noticeable decreases in strength should be apparent at 204°C, and that the precipitation strengthening contribution should be absent after 260°C exposure. Microstructural development upon aging and high-temperature exposure in the non-Li-containing alloys resembles that in I/M 2024-Al. Thus, any increase in strength of the RSP alloys, compared with their I/M counterparts, is the result of Hall-Petch strengthening from the fine subgrain size or dispersion strengthening from the Al_9FeNi dispersoids.

General microstructural features of peak-aged Al-3Li-1.5Cu-1Mg-0.5Co-0.2Zr are revealed in Figure 40a. The structure is unrecrystallized, with 2- to 4-μm diameter subgrains. Numerous low-angle and several high-angle boundaries among subgrains are observed, as well as a sparse distribution of 0.3- to 0.4-μm diameter Al_9Co_2 dispersoids. Rows of fine, well-separated oxide particles outline the prior particle boundaries. Subgrain boundaries sometimes coincide with the oxides, but they have more often migrated from the

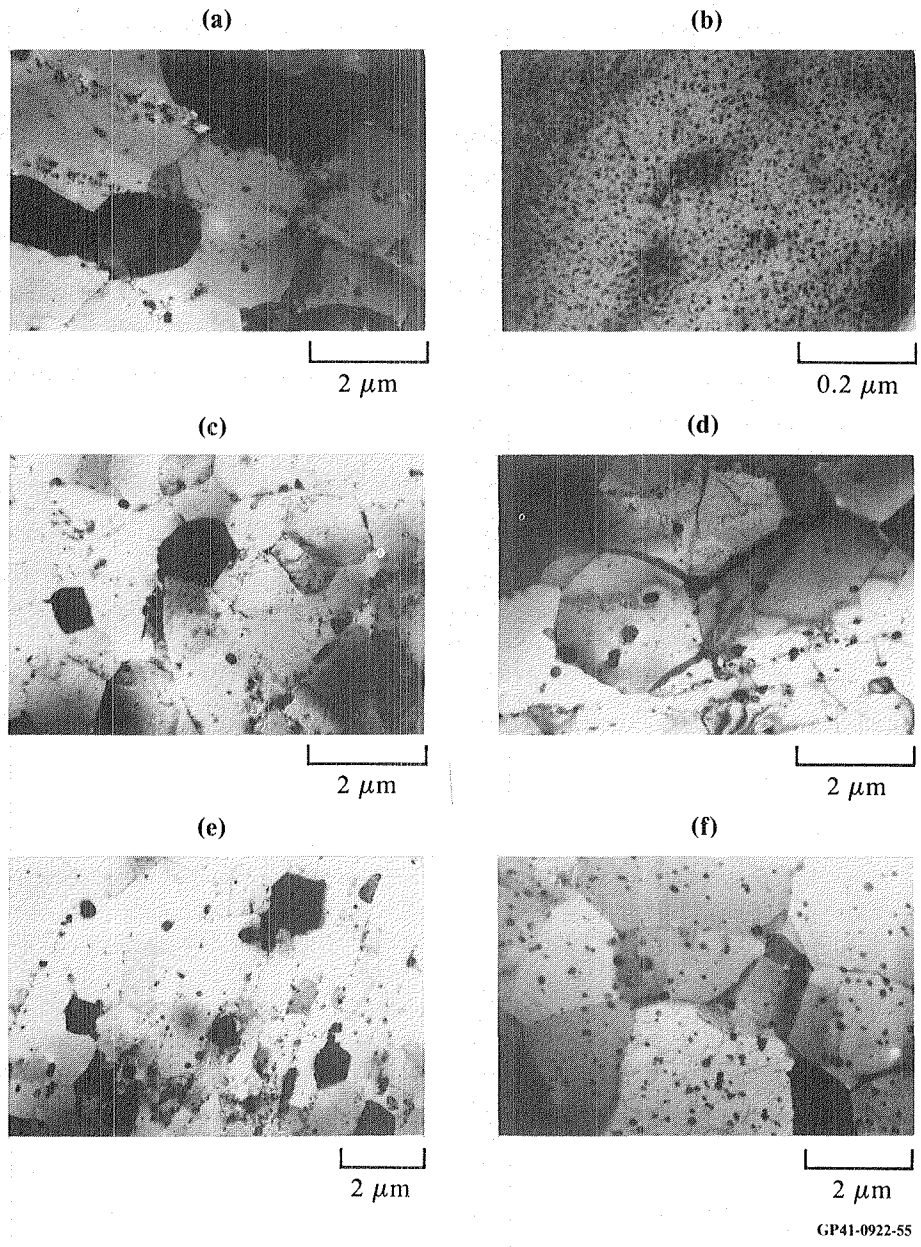

Figure 40. TEM micrographs of Al-3Li-1.5Cu-1Mg-0.5Co-0.2Zr extrusions: (a) - (c) from vacuum atomized powder, (a), (b) T6-530 temper (solution-treated 530°C/1 h + aged 177°C/8 h), (c) T6-560 temper (solution-treated 560°C/1 h + aged 177°C/8 h); (d) from argon ultrasonically atomized powder, T6-530 temper; (e) from helium ultrasonically atomized powder, T6-560 temper; (f) from roller-quenched flakes, T6-530 temper.

oxides during extrusion, solution treatment, or both. Rows of oxides are less frequently observed in the non-Li-containing alloy. At higher magnification (Figure 40b), a homogeneous distribution of 15- to 20-nm diameter δ' precipitates is observed.

Microstructures of USGA extrusions are similar to that of the VA extrusion (compare Figures 40d and 40e with 40a). The RQ extrusion (Figure 40f) has a larger average subgrain size, a more homogeneous distribution of Al_9Co_2 dispersoids, and fewer oxides (owing to the greater thickness of the original particulates) than the powder extrusions. This extrusion is the only one in which differences in particulate type produce significant differences in the peak-aged microstructure.

Upon solution treatment at 560°C, the Al-3Li-1.5Cu-1Mg-0.5Co-0.2Zr extrusion exhibits equiaxed subgrains rather than the mosaic structure observed after 530°C solution treatment (compare Figure 40c with Figure 40a). Since both structures have subgrains of similar diameter, microstructural modification has probably occurred by subgrain boundary motion at the higher solution-treatment temperature, rather than by recrystallization. The subtle change in microstructure is unlikely to significantly affect mechanical properties.

6.2 Properties

6.2.1 Density

Densities of extrusions are listed in Table 7. Increases in density of the non-Li-containing alloys relative to 2024-Al are in good agreement with predictions based on density contributions from the Al_9FeNi dispersoids. Density decreases of the Li-containing alloys relative to that of 7075-Al are in accord with those expected from alloys containing 2.7-3Li. Densities of Li-containing USGA extrusions are slightly greater than those of VA or RQ extrusions, in accord with their lower Li and Mg concentrations.

TABLE 7. DENSITIES OF RSP ALLOY EXTRUSIONS.

Alloy and particulate type	Density (g/cm^3)	% increase relative to 2024-Al	% decrease relative to 7075-Al
Al-4.4Cu-1.5Mg-1Fe-1Ni-0.2Zr			
Vacuum atomized powder	2 806	1 3	
Argon ultrasonically atomized powder	2 813	1 6	
Helium ultrasonically atomized powder	2 823	1 9	
Al-4.4Cu-1.5Mg-2Fe-2Ni-0.2Zr			
Vacuum atomized powder	2 861	3 3	
2024-Al (I/M)	2 77	—	
Al-3Li-1 5Cu-1Mg-0.5Co-0.2Zr			
Vacuum atomized powder	2 489		11 1
Argon ultrasonically atomized powder	2 530		9 6
Helium ultrasonically atomized powder	2 530		9 6
Roller-quenched flakes	2 492		11 0
7075-Al (I/M)	2 80		—

GP41 0922 7

6.2.2 Elastic Modulus

Elastic moduli of heat-treated extrusions are given in Table 8. The relatively small volume fractions of incoherent dispersoids in the non-Li-containing alloy increase its elastic modulus by only 2 to 3% relative to that

TABLE 8. ELASTIC MODULI OF RSP ALUMINUM ALLOY EXTRUSIONS.

Alloy composition and particulate type	Heat treatment	Elastic modulus, (GPa[10^6 psi])	% increase relative to 2024-Al	% increase relative to 7075-Al
Al-4.4Cu-1.5Mg-1Fe-1Ni-0.2Zr				
Vacuum atomized powder	T851	73 9 (10.72)	2.1	
Argon Ultrasonically atomized powder	T851	74 7 (10 85)	3 3	
Helium ultrasonically atomized powder	T851	73 7 (10 68)	1 8	
2024-Al(I/M)	—	72 4 (10 50)	—	
Al-3Li-1.5Cu-1Mg-0.5Co-0.2Zr				
Vacuum atomized powder	T6/530	78.5 (11 39)		10 6
Argon ultrasonically atomized powder	T6/530	76 0 (11 02)		7 0
Helium ultrasonically atomized powder	T6/560	76 3 (11 06)		7 5
Roller-quenched flakes	T6/530	80 1 (11 62)		12 8
7075-Al (I/M)	—	71 0 (10 30)		—

GP41 0922 8

of 2024-Al. The percent modulus increase in Al-Li alloys, compared with I/M 7075-Al, has been found in previous work to be approximately equal to the percent density decrease, and this empirical rule is followed for the data reported here. The moduli of Al-3Li-1.5Cu-1Mg-0.5Co-0.2Zr VA and RQ extrusions are 17 to 20% larger than that of pure aluminum [67 GPa [9.7 x 10^6 psi] (22)], in accord with the rule-of-mixtures calculation that the modulus in Al-Li alloys should increase by about 6% for every wt% Li added.

6.2.3 Tensile Mechanical Properties

6.2.3.1 Non-Li-Containing Alloys

Mechanical properties of non-Li-containing alloy extrusions and forgings at temperatures between 25 and 260°C are shown in Figures 41-48. Comparisons between results for the RSP alloys and those for commercial 2XXX alloys such as 2024, 2124, and 2219 (Figures 46-48) illustrate the improvements in properties obtained by RSP and addition of fine, incoherent dispersoids to an Al-4.4Cu-1.5Mg matrix.

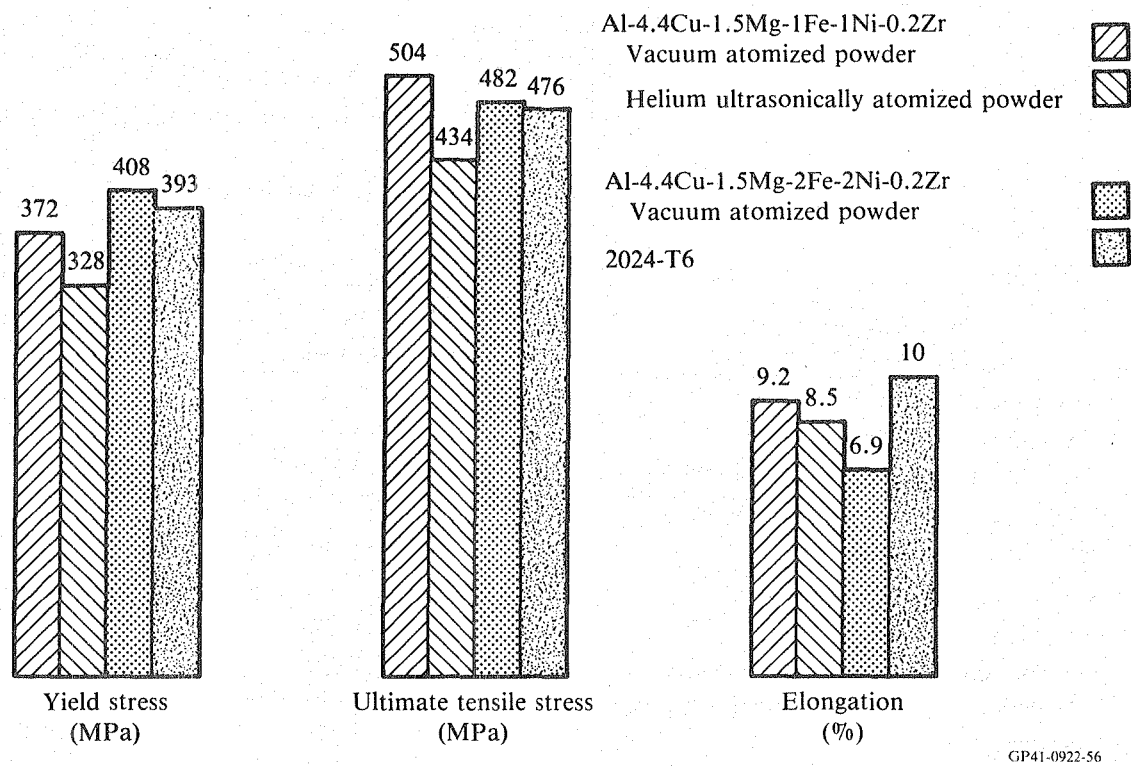

Figure 41. Ambient temperature tensile properties of non-Li-containing alloys: T6 temper (solution treated 530°C/1 h + aged 190°C/8 h).

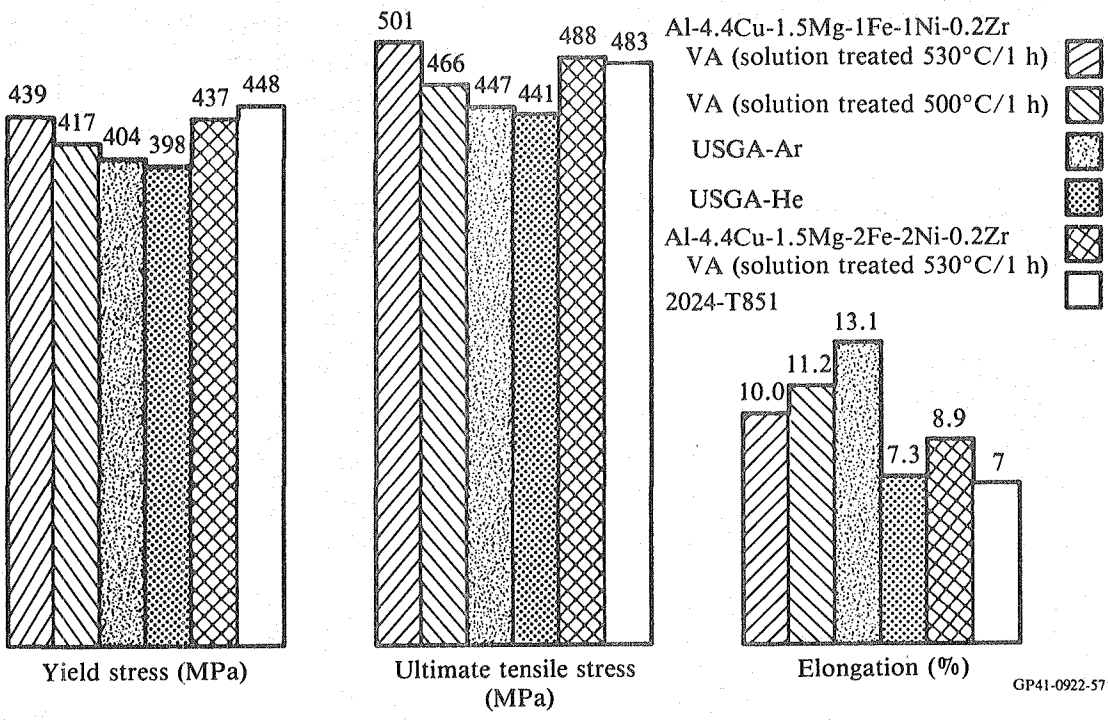

Figure 42. Ambient temperature tensile properties of non-Li-containing alloy extrusions: T851 temper (solution treated 530°C/1 h [except as shown] + 2% stretch + 190°C/8 h).

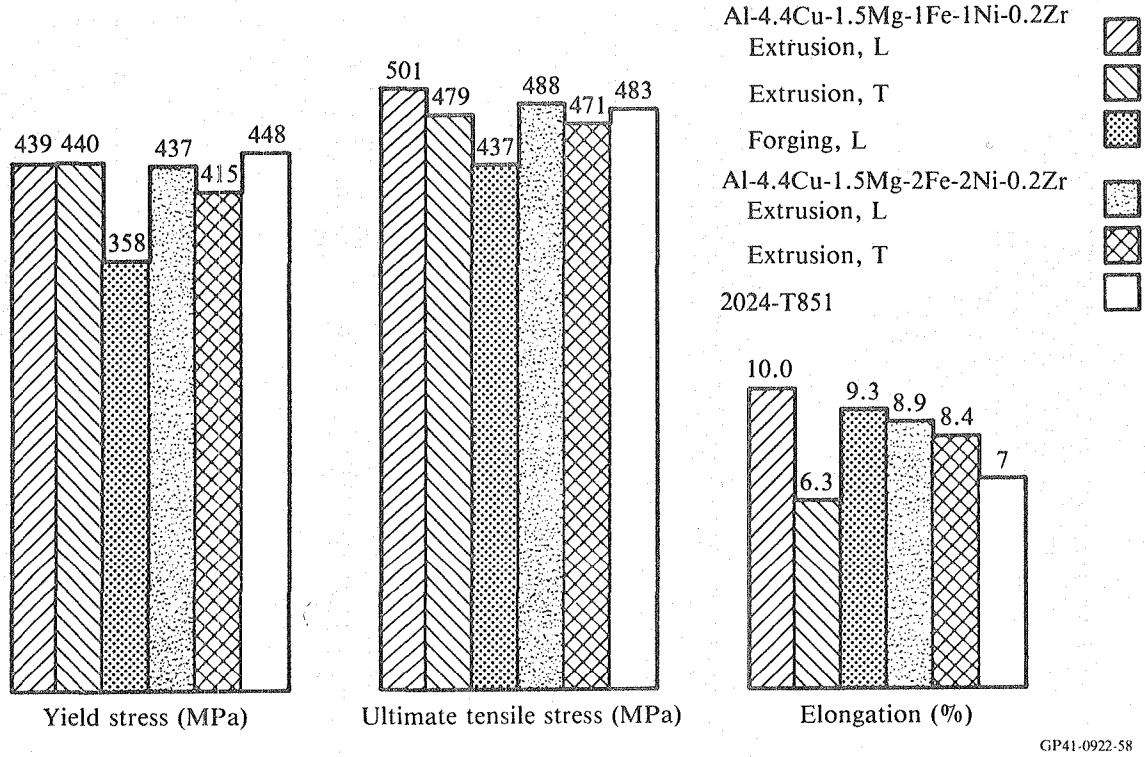

Figure 43. Ambient temperature tensile properties of non-Li containing alloy extrusions and forgings: T851 temper.

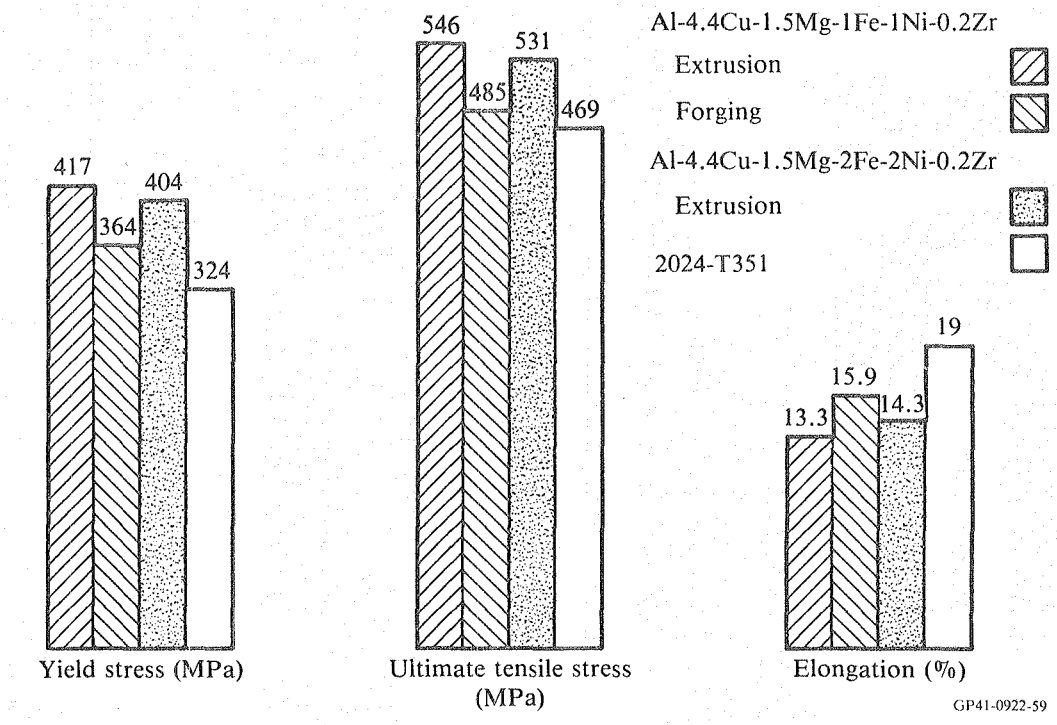

Figure 44. Ambient temperature tensile properties of non-Li -containing alloy VA extrusions and forgings: T351 temper (solution treated 530°C/1 h + 2% stretch + aged 25°C/168 h).

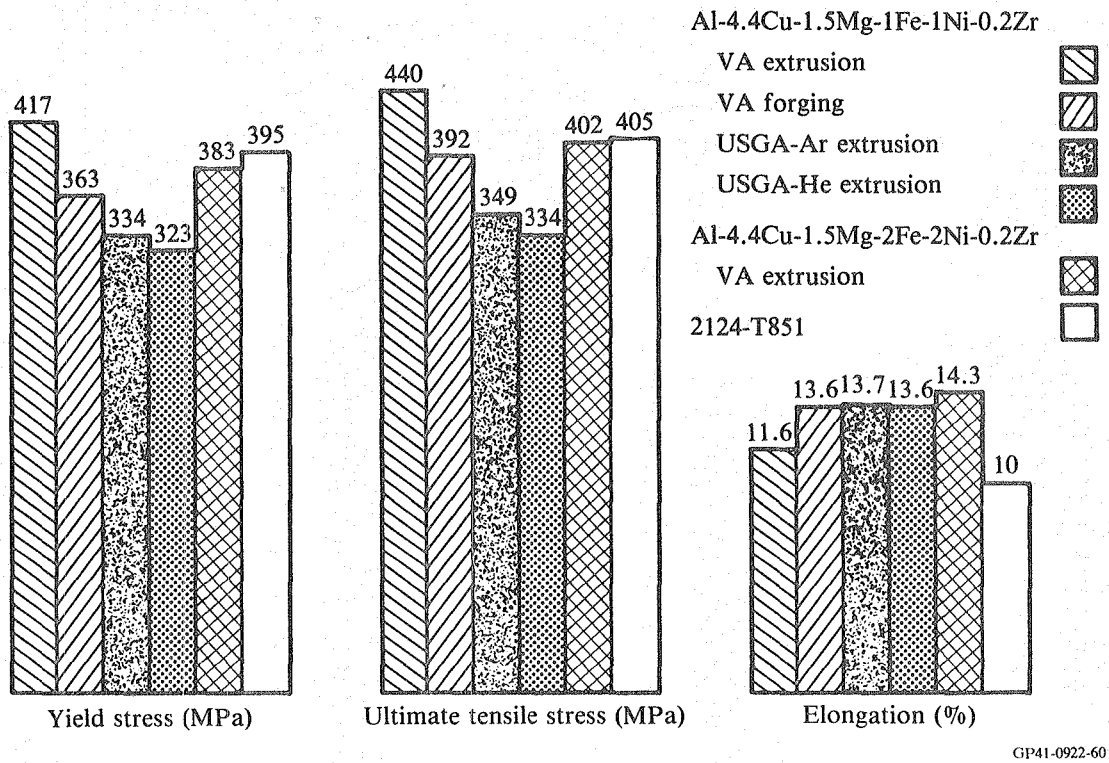

Figure 45. Tensile properties of non-Li-containing alloy extrusions and forgings: T851 temper, at 150°C following 100 h exposure at 150°C.

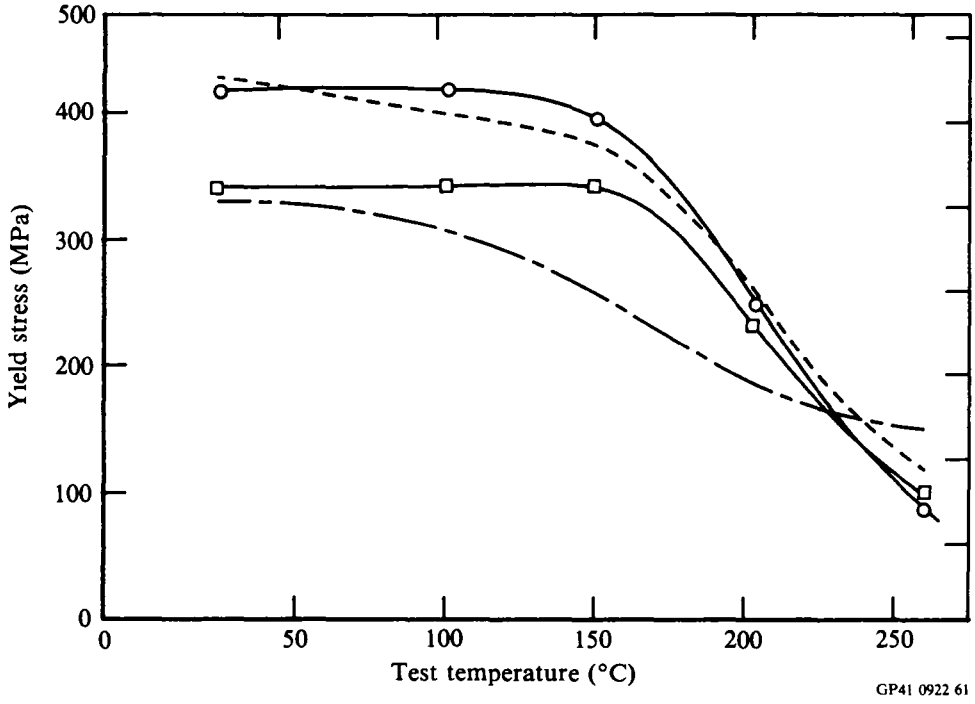

Figure 46. Variation with temperature of the yield stress after 100 h exposure at temperature of (○) Al-4.4Cu-1.5Mg-1Fe-1Ni-0.2Zr VA extrusion, (□) Al-4.4Cu-1.5Mg-1Fe-1Ni-0.2Zr forging, (- - -) 2124-Al plate, and (— - —) 2219-Al(23). Original temper T851.

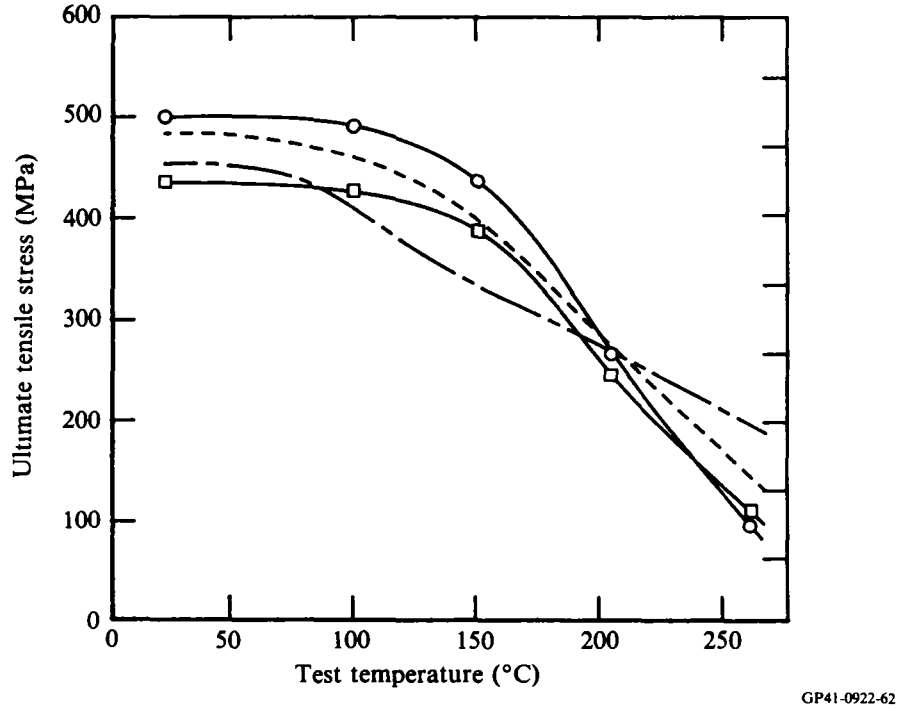

Figure 47. Variation with temperature of the ultimate tensile stress after 100 h exposure at temperature of (○) Al-4.4Cu-1.5Mg-1Fe-1Ni-0.2Zr VA extrusion, (□) Al-4.4Cu-1.5Mg-1Fe-1Ni-0.2Zr VA forging, (- - -) 2124-Al plate, and (— - —) 2219-Al(23). Original temper T851.

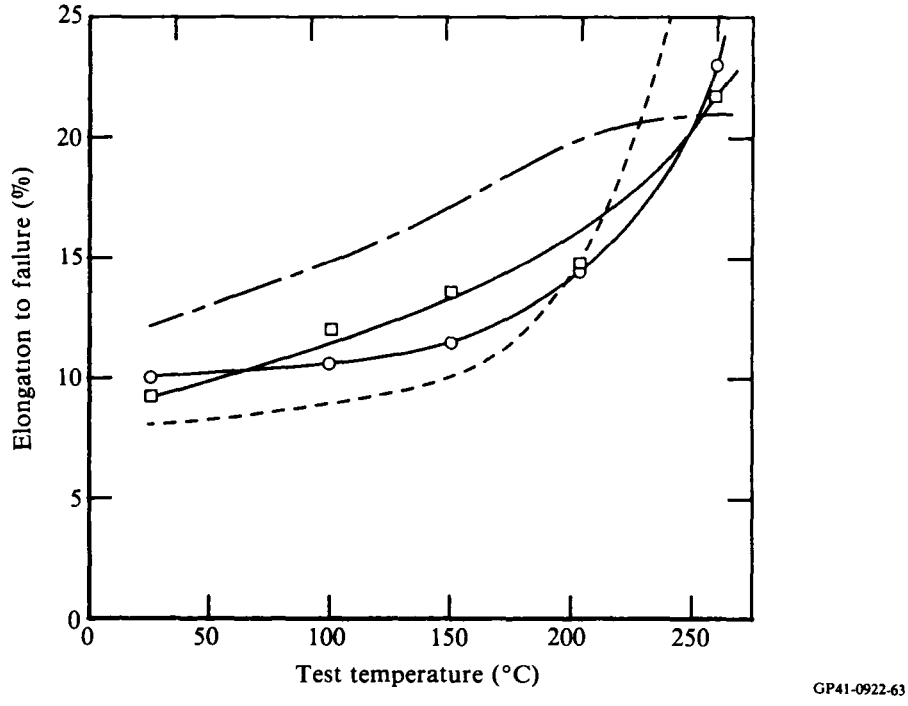

Figure 48. Variation with temperature of the ductility after 100 h exposure at temperature of (○) Al-4.4Cu-1.5Mg-1Fe-1Ni-0.2Zr VA extrusion, (□) Al-4.4Cu-1.5Mg-1Fe-1Ni-0.2Zr VA forging, (- - -) 2124-Al plate, and (——) 2219-Al(23). Original temper T851.

Results of a preliminary study on extrusions in the T6 temper (Figure 41) show that properties of the VA extrusions are similar to those of 2024-Al, while the properties of the USGA-He extrusion are significantly lower, probably as a result of the smaller (Cu+Mg) concentration available for precipitation. The effect of adding 2Fe-2Ni instead of 1Fe-1Ni is to increase the yield stress about 35 MPa and slightly reduce the ductility.

As expected from the microstructures (compare Figure 37 with Figure 38), yield stresses of 1Fe-1Ni extrusions in the T851 temper are 70-90 MPa larger than in the T6 temper, with little change in tensile strength or ductility. Changes in the properties of the 2Fe-2Ni alloy are smaller and result in properties similar to those of the 1Fe-1Ni alloy in the T851 temper. Variations in properties from the T6 to the T851 tempers for the VA extrusions strongly resemble those of 2024-Al, and no advantages resulting specifically from RSP are observed.

The T851 properties of 1Fe-1Ni extrusions from various particulate types follow compositional differences (Figure 42). In particular, the USGA-He extrusion has lower strength than the VA extrusion, in keeping with its lower Mg level, but the strength is independent of the high solidification rate of He-atomized powder. These observations are consistent with the microstructures (Figures 37 and 38), which show little difference among VA and USGA extrusions.

The quality of consolidation processing and differences in consolidation processing between forgings and extrusions are reflected in the mechanical properties results shown in Figure 43. Transverse yield and tensile strengths of 1Fe-1Ni extrusions are 95-100% of the corresponding longitudinal properties, indicating that the extrusion processing (Section 3.3.2) was effective in disintegrating particulate oxide layers and obtaining good interparticulate bonding. Yield and tensile strengths of the VA forging are 70 to 80 MPa lower than in the corresponding extrusion; however, the ductilities are similar, suggesting that the lower properties of the forging result from its weaker texture (compare Figures 26b and 28b), rather than deficient consolidation processing.

Yield and ultimate tensile strengths of non-Li-containing alloy extrusions in the T351 (stretched and naturally aged) temper are 70 to 100 MPa larger than in 2024-T351, with reasonable ductilities (Figure 44). The near-equivalence of properties of the 1Fe-1Ni and 2Fe-2Ni extrusions indicates that the source of higher strength is substructural refinement or texture effects, rather than dispersion strengthening.

Differences in tensile properties among extrusions from various particulate types, tested at 150°C, generally follow differences in Mg concentration (Figure 45), except that the penalty for a shortage of Mg is more pronounced than at 25°C. For instance, the T851 yield strength of the USGA-He extrusion at 25°C is 91% of that of the VA extrusion (Figure 43), but only 77% as large at 150°C (Figure 45). The larger dispersoid concentration in the 2Fe-2Ni alloy is no more important at 150°C than at 25°C, and the 1.1Mg level in this extrusion (compared with 1.5Mg in the 1Fe-1Ni extrusion) causes yield and tensile stresses to be 30-40 MPa lower.

The variation in T851 tensile properties of VA extrusions and forgings with temperature, 25 to 260°C, is shown in Figures 46-48. The RSP materials

have yield strength retention at 150°C superior to those of 2124-Al or 2219-Al (96 and 100% of room temperature strength at 150°C for VA extrusions and forgings, respectively, compared with 88% for 2124-Al and 79% for 2219-Al). The absolute yield and tensile strengths of the 1Fe-1Ni extrusion are 5-8% larger than those of 2124-Al at 100 to 150°C, but the strength advantages vanish above about 180°C, and 2124-Al is stronger at 260°C. Extrusion and forging properties above 200°C are similar, probably as the result of the disappearance of texture strengthening as a major contributor to overall strength above ~ 175°C. Finally, ductilities of the RSP materials are superior to those of 2124-Al up to about 200°C. This improvement is most probably connected with the absence in RSP materials of coarse (20-μm diameter), impurity-containing particles which can act as crack initiation sites.

SEM micrographs of typical fracture surfaces are shown in Figure 49. Most fractures are at 45° to the tensile axis, following the direction of maximum resolved shear stress (Figure 49a). Ductile tearing is the universal fracture mode, as evinced by the presence of 0.5- to 2-μm diameter dimples on all fracture surfaces (Figures 49b-f). Transverse and longitudinal specimens have similar fracture surfaces, except for striations on transverse specimen surfaces which reflect the extrusion texture (Figures 49b-c). Occasional coarse inclusions on the fracture surface (Figure 49d) contain Al and Cu, and thus are not foreign particles. The sample-to-sample consistency of ductility is good, suggesting that the presence of coarse inclusions in some samples does not significantly affect mechanical properties. As the test temperature is raised, the average dimple size increases and plastic tearing becomes more evident, but the fracture mode does not change (Figures 49e-f). The fracture behavior of the forgings is similar to that of the extrusions.

6.2.3.2 Li-Containing Alloy

Properties of Li-containing extrusions are largely independent of particulate type (Figure 50). T6 yield stresses of RQ extrusions are, however, 40 to 60 MPa lower than those of VA extrusions of similar composition, and tensile stresses are 12-20 MPa lower (Figures 50 and 52). T6 ductilities of extrusions are uniformly 3 to 4%, regardless of yield stress level. Increasing the solution-treatment temperature to 560°C to solutionize larger amounts of Li, Cu, and Mg and provide a larger density of precipitates

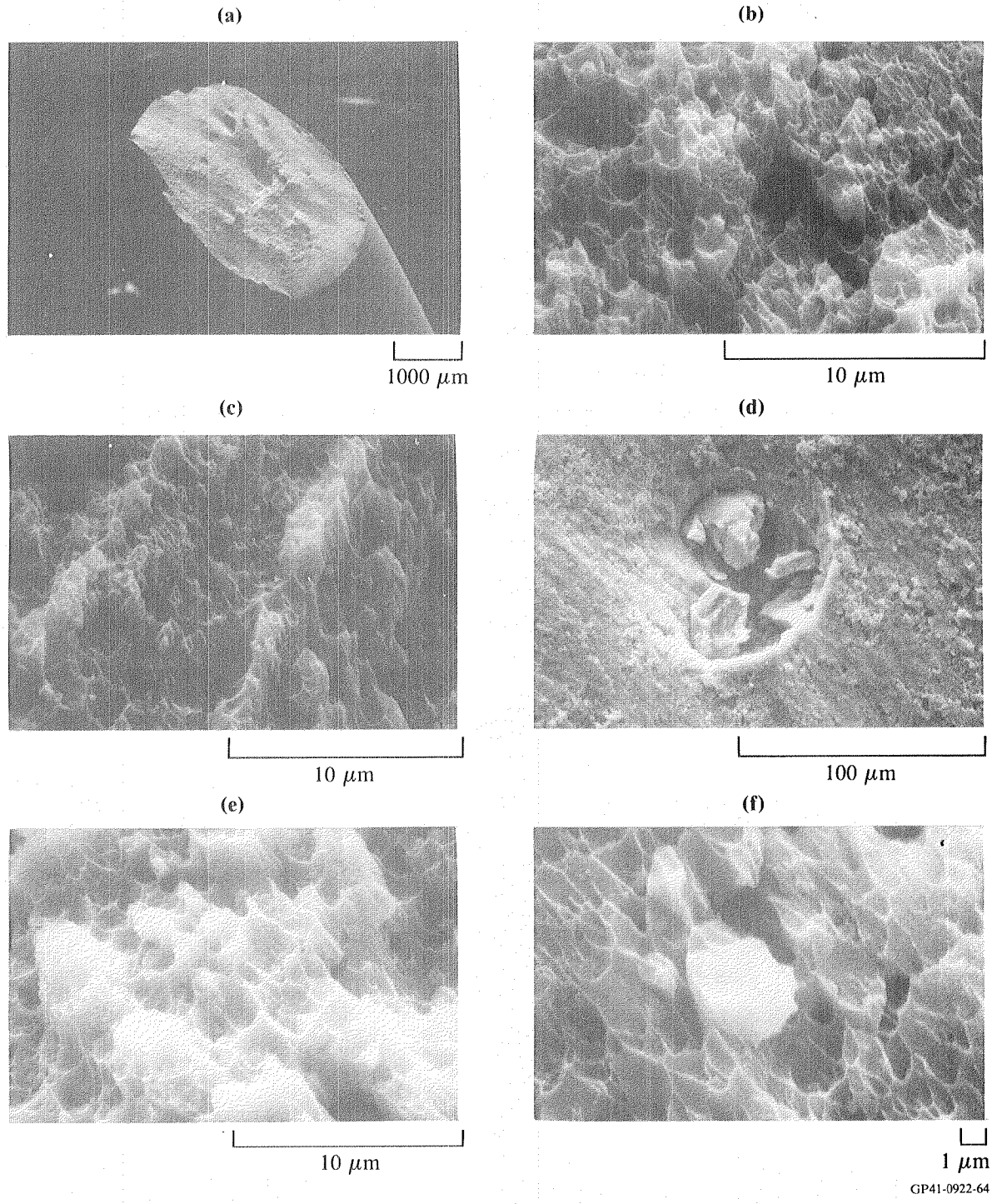

Figure 49. SEM micrographs of Al-4.4Cu-1.5Mg-1Fe-1Ni-0.2Zr VA extrusion fracture surfaces: (a) T851, general appearance; (b) T851, longitudinal, 25°C test; (c) T851, transverse, 25°C test; (d) large inclusion on fracture surface (T351, 25°C test); (e) T851, longitudinal, 150°C test; (f) T851, 204°C test.

results in a 20 to 30 MPa increase in T6 yield stress and a 30 to 50 MPa increase in ultimate tensile stress. T6 strengths of extrusions are generally equal to or greater than typical properties of 7075-T73, but ductilities fall well short of the 13% typical of the I/M alloy.

Figures 50 and 51 reveal deficiencies in consolidation processing of Li-containing extrusions and forgings. T6 yield and ultimate tensile stresses of forgings are 70 to 90 MPa lower than those of VA extrusions, and the ductility of the forging is significantly lower than that of extrusions, showing that interparticle bonding was not adequately achieved in the forging (Figure 50). Both T6 transverse strengths and ductilities are considerably lower than the corresponding longitudinal properties (Figure 51), reflecting imperfections in consolidation processing for the extrusions as well as for the forging.

T851 strengths of extrusions are generally superior to those in the T6/530 temper, and approximately equal to strengths in the T6/560 temper (Figures 51, 52 and 53), combined with 3 to 5% ductility. The 2% stretch introduces defects which homogenize the precipitation of plate-like phases such as

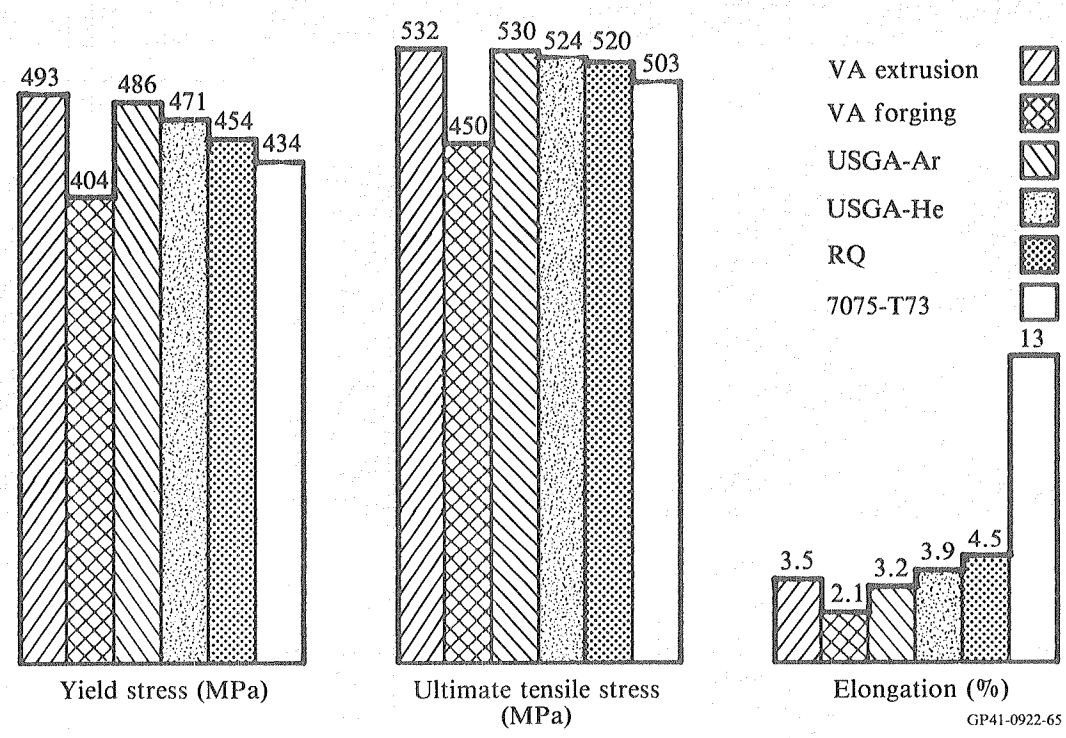

Figure 50. Ambient temperature tensile properties of Al-3Li-1.5Cu-1Mg-0.5Co-0.2Zr extrusions and forgings: T6/530 temper (solution treated 530°C/1 h + aged 177°C/8 h).

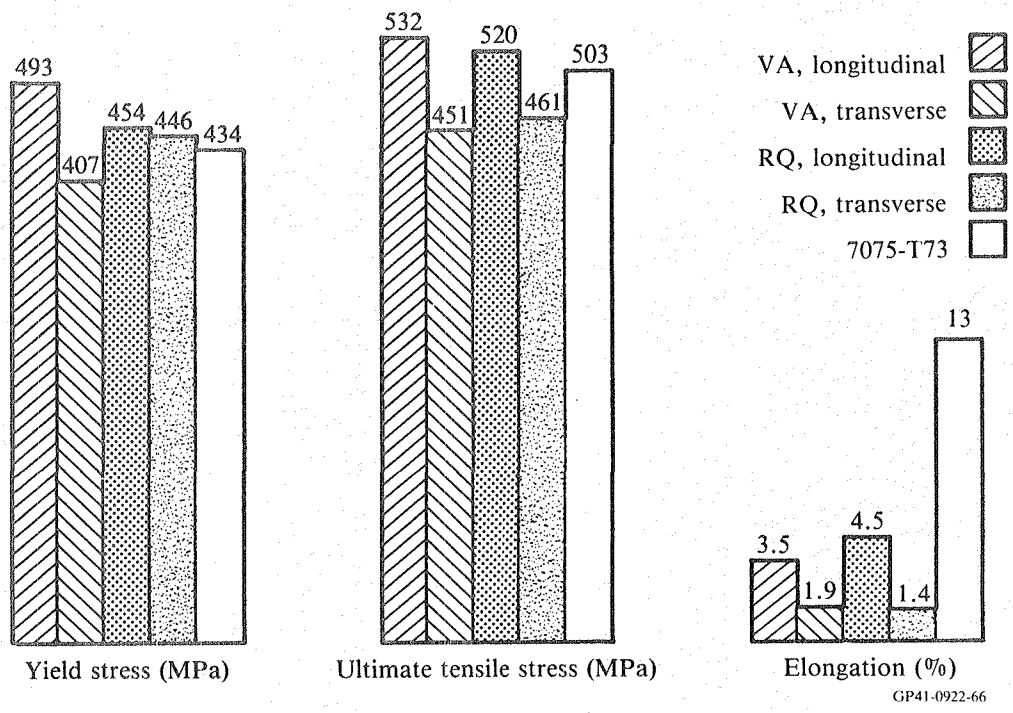

Figure 51. Longitudinal and transverse ambient temperature properties of Al-3Li-1.5Cu-1Mg-0.5Co-0.2Zr extrusions: T6/530 temper.

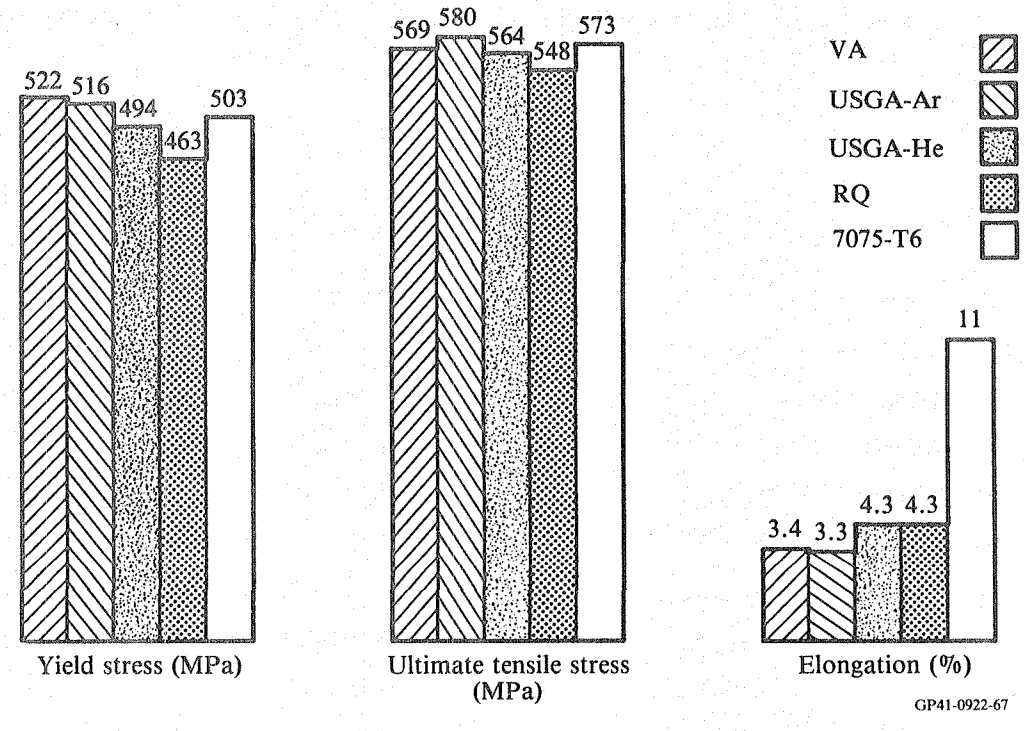

Figure 52. Ambient temperature tensile properties of Al-3Li-1.5Cu-1Mg-0.5Co-0.2Zr extrusions: T6/560 temper (solution treated 560°C/1 h + aged 177°C/8 h).

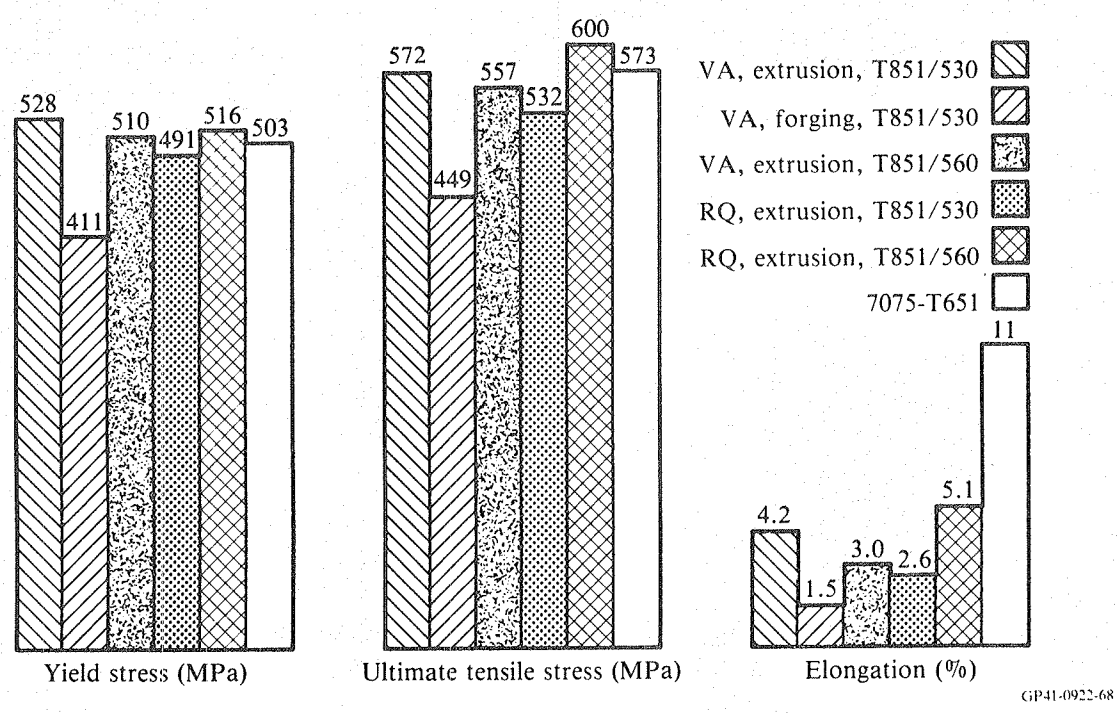

Figure 53. Ambient temperature tensile properties of Al-3Li-1.5Cu-1Mg-0.5Co-0.2Zr extrusions and forgings: T851 temper (solution treated 530 or 560°C/1 h + 2% stretch + aged 177°C/8 h).

T1(Al_2CuLi). As in the case of Al-Cu-Mg alloys, the increased density of precipitation increases the yield stress, but does not affect the ultimate tensile stress. The T6/560 and T851 strengths of the Li-containing alloy are similar to those of 7075-T6, but ductilities fall well short of the 11% characteristic of the I/M alloy.

The 150°C tensile curves of the Li-containing alloys exhibit flow softening beyond the yield point, so that only yield stresses are meaningful (Figure 54). The Li-containing alloy retains its strength at 150°C (94-100% of 25°C yield strength), with a modest increase in ductility.

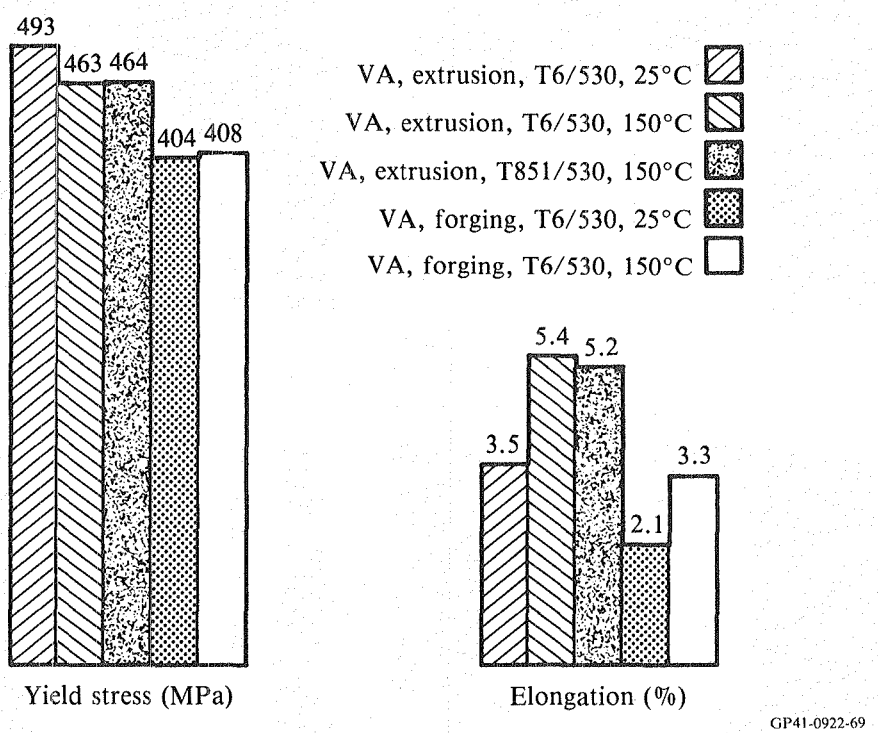

Figure 54. Tensile properties at indicated temperatures of Al-3Li-1.5Cu-1Mg-0.5Co-0.2Zr extrusions and forgings.

Fracture surfaces of Al-3Li-1.5Cu-1Mg-0.5Co-0.2Zr extrusion tensile samples show features on the scale of the subgrains (Figure 55a). At higher magnification, the T6/530 fracture surface shows shallow dimples (Figure 55b), but dimpling is less pronounced than in the non-Li-containing alloy. The microcrack at the right of Figure 55b is in an Al-Li-Cu-(Mg) constituent particle. Fracture of the RQ extrusion is more explicitly inter-subgranular, with less evidence of dimpling, and becomes strongly faceted in the high-strength T851/560 temper (Figures 55c-d). Fracture surfaces of the forgings are similar to those of the extrusions.

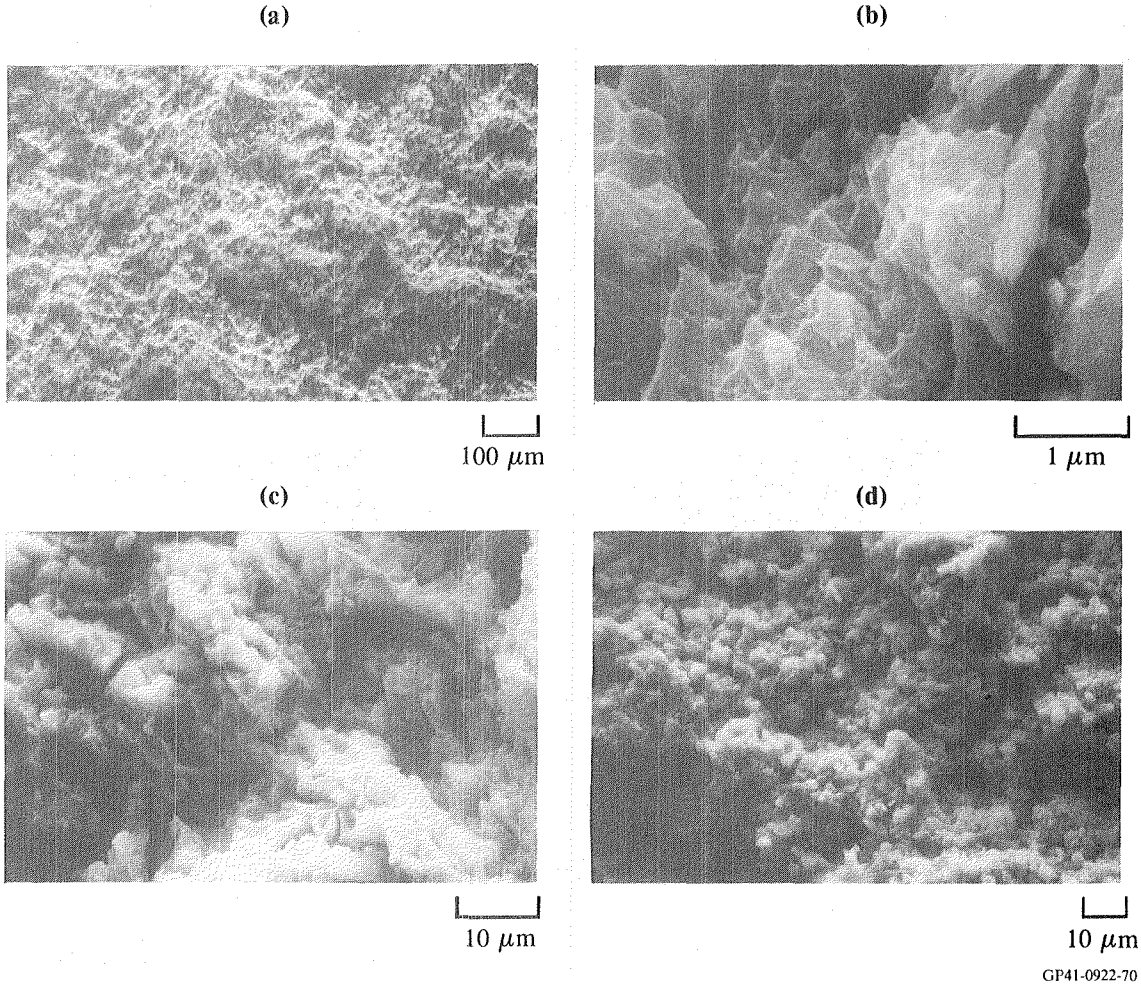

Figure 55. Fractographs of Al-3Li-1.5Cu-1Mg-0.5Co-0.2Zr extrusions: (a) VA, T6/530, longitudinal, 25°C test, general appearance; (b) VA, T6/530, longitudinal, 25°C test, microscopic appearance; (c) RQ, T6/530, longitudinal, 25°C test; (d) RQ, T851/560, longitudinal, 25°C test.

6.2.4 Fracture Toughness

Fracture toughness values for extrusions and forgings in the T851 temper and TL and LT orientations are listed in Table 9. As expected, K_Q values for the extrusions are larger in the LT than in the TL orientation, but K_Q for the TL orientation in the forgings is, surprisingly, larger than for the geometrically equivalent LT orientation. Although K_Q for the non-Li-containing extrusions and forgings does not meet the plane-strain criterion owing to insufficiently thick samples, the reported values are qualitatively consistent with a typical K_{IC} for 2024-Al of 30 $MPa \cdot m^{1/2}$. Toughnesses of the Li-containing alloys are low as a result of consolidation deficiencies revealed by the tensile properties data in Section 6.2.3.

TABLE 9. FRACTURE TOUGHNESSES OF EXTRUSIONS AND FORGINGS.

	K_Q [MPa·m$^{1/2}$ (ksi·in$^{1/2}$)]			
	Extrusion		Forging	
Alloy	LT	TL	LT	TL
Al-4.4Cu-1.5Mg-1Fe-1Ni-0.2Zr	45 7	28 2	31 7	36 7
VA powder, T851 temper	(41 5)	(25 6)	(28 8)	(33 4)
Al-3Li-1.5Cu-1Mg-0.5Co-0.2Zr	11 2	8 9	10 6	11 1
VA powder, T851 temper	(10 2)	(8 1)	(9 6)	(10 1)

GP41-0922 9

6.2.5 Fatigue-Crack-Growth Rate

Fatigue-crack-growth-rate (FCGR) data for extrusions and forgings in the T851 temper and TL and LT orientations are shown in Figures 56-59. The 2% stretch required for the T851 temper also has the effect of relieving compressive stresses introduced during quenching, thus permitting a valid FCGR determination **(23)**.

FCGR results on Al-4.4Cu-1.5Mg-1Fe-1Ni-0.2Zr VA extrusions show a 50 to 60% larger crack-growth rate for the TL than for the LT orientation (Figure 56). This result is reasonable in view of the unrecrystallized "pancake" grain microstructure and strong extrusion texture. Conversely, the FCGR for the LT orientation in the VA forging is 35 to 60% larger than for the TL orientation (Figure 57). Since the forging has a symmetrical fiber texture, the LT and TL orientations should be equivalent and the FCGR results should be similar; thus the observed behavior is not well understood. For equivalent orientations, the FCGR in the forging is 40 to 90% larger than that in the extrusion, owing to the difference in strength between the two product forms. Crack-growth rates in the RSP extrusions and forgings are a factor of 1.7 to 5 larger than in 2124-T851. A similar effect has been observed in comparing the FCGR of P/M 2024-T851 with that of I/M 2024-T851 and has been attributed to the decreased tortuosity of the crack path and increased accumulation of plastic zone damage at grain boundaries as the result of the finer grain size in the P/M material **(24)**.

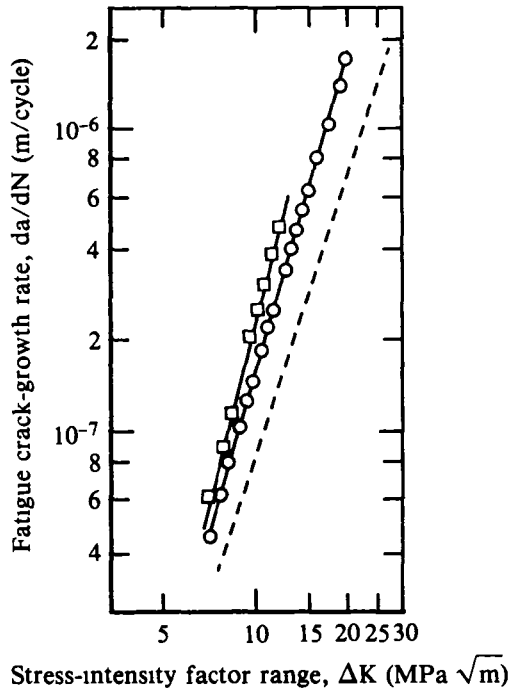

Figure 56. FCGR results on Al-4.4Cu-1.5Mg-1Fe-1Ni-0.2Zr VA extrusions, T851 temper: (○) LT orientation, (□) TL orientation, and (- - -)typical results for 2124-T851 (23).

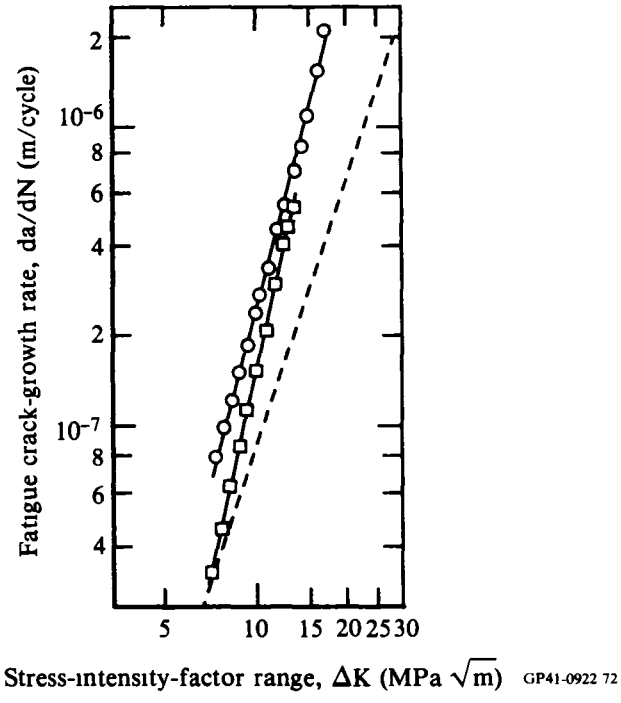

Figure 57. FCGR results on Al-4.4Cu-1.5Mg-1Fe-1Ni-0.2Zr VA forgings, T851 temper: (○) LT orientation, (□) TL orientation, and (- - -) typical results for 2124-T851 (23).

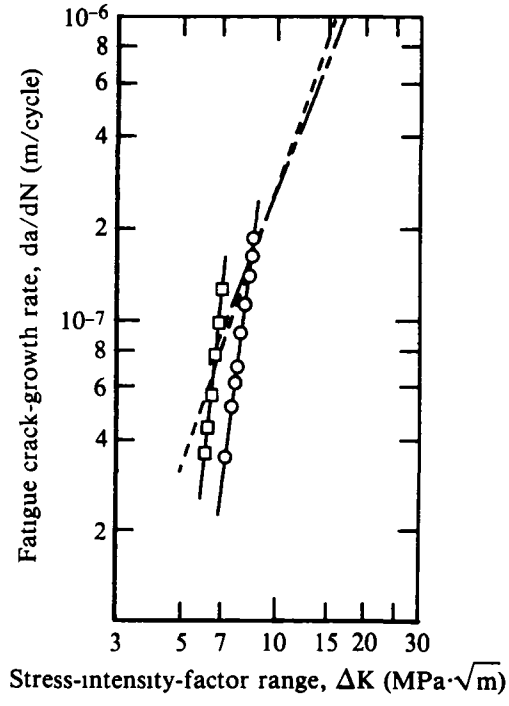

Figure 58. FCGR results on Al-3Li-1.5Cu-1Mg-0.5Co-0.2Zr VA extrusions, T851/530 temper: (○) LT orientation, (□) TL orientation, (- - -) typical results for 7075-T651 (24), and (— - —) typical results for 7091-T7E69(24).

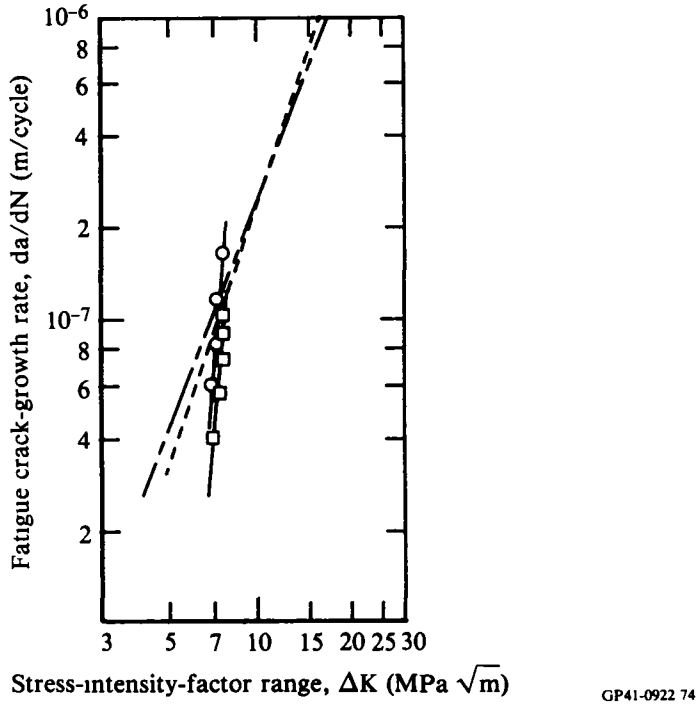

Figure 59. FCGR results on Al-3Li-1.5Cu-1Mg-0.5Co-0.2Zr VA forgings, T851/530 temper: (○) LT orientation, (□) TL orientation, (- - -) typical results for 7075-T651 (24), and (— - —) typical results for 7091-T7E69(24).

Similar orientation effects are seen in FCGR results on the Al-3Li-1.5Cu-1Mg-0.5Co-0.2Zr extrusions and forgings (Figures 58 and 59). The stress intensity factor required to produce a crack-growth rate of 10^{-7} is about 7 to 8 MPa•$m^{1/2}$ for all alloy extrusions and forgings, but the slope of the da/dN-vs.-ΔK curve for the Li-containing alloy is much larger than that for the non-Li-containing alloy, indicating higher growth rates at larger ΔK values. This susceptibility of crack-growth rate to increased load for the Li-containing alloy may be related to the imperfect consolidation processing, which is also reflected in degraded transverse tensile properties. Crack-growth rates for the Li-containing alloy extrusions and forgings are smaller than those for I/M 7075-Al and P/M 7091-Al at ΔK values less than about 7 MPa•$m^{1/2}$, but increase rapidly, and greatly exceed crack growth rates for the commercial alloys at higher ΔK.

6.2.6 Creep Resistance

Results of creep experiments on Al-4.4Cu-1.5Mg-1Fe-1Ni-0.2Zr T851 extrusions and forgings at 150°C are shown in Figure 60. On an absolute rupture stress basis, the extrusions perform better than the forgings, but the performance of the forgings is superior when normalized to yield strength.

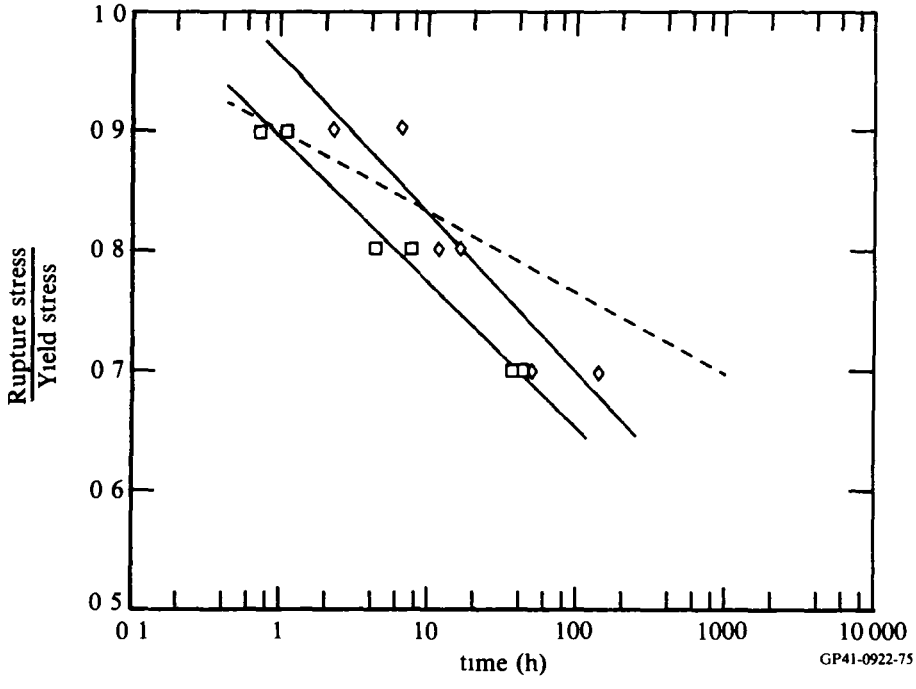

Figure 60. 150°C creep-test results for T851 temper Al-4.4Cu-1.5Mg-1Fe-1Ni-0.2Zr: (□) VA extrusions and (◊) VA forgings, normalized to yield stress; (– – –) typical results for 2124-T851.

The rupture time of extrusions and forgings is comparable to that of 2124-Al at high loads, but increases slowly with decreasing load and is a factor of 20 to 50 smaller than that of 2124-T851 at 60% of the yield stress.

6.2.7 Stress-Corrosion-Cracking Resistance

Results of C-ring tests on Al-3Li-1.5Cu-1Mg-0.5Co-0.2Zr T851 extrusions and forgings are shown in Figures 61 and 62. Because of differing geometries of the extrusions and forgings, the extrusions were tested in the T orientation while the forgings were tested in the more-susceptible S orientation. Failure times were relatively short for both product forms and particularly so for forgings, where failure at 50% of the yield stress occurred in all samples in less than 100 h. None of the non-Li-containing alloy C-rings, tested under the same relative loads, failed in 1000 h. The relative performances of non-Li- and Li-containing alloys and Li-containing alloy extrusions and forgings are similar to relative performances of the same alloys and product forms in longitudinal and transverse tensile tests, suggesting that the effectiveness of consolidation processing and interparticle bonding largely determines the stress-corrosion-cracking (SCC) resistance of the alloys.

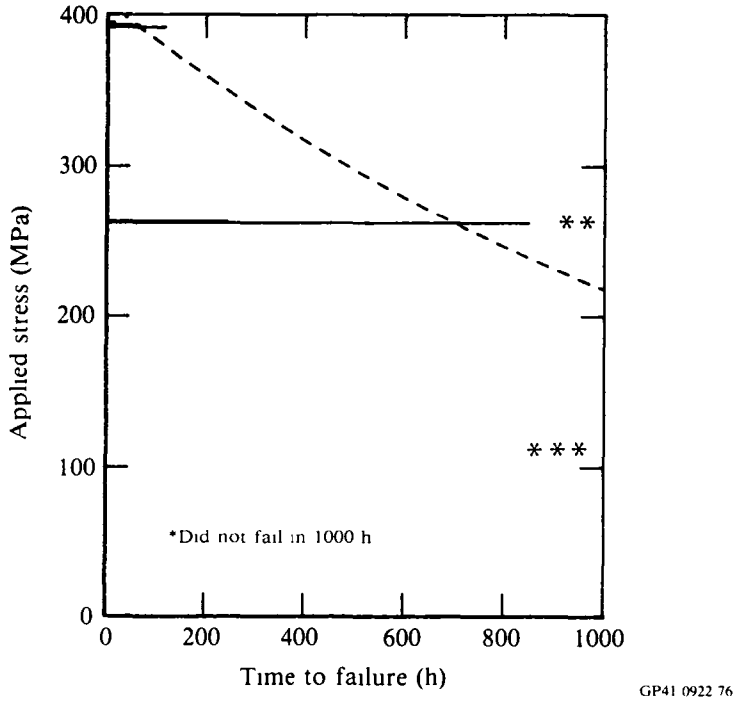

Figure 61. Time-to-failure in alternate immersion C-ring tests of Al-3Li-1.5Cu-1Mg-0.5Co-0.2Zr VA extrusions· T851/530 temper, T orientation

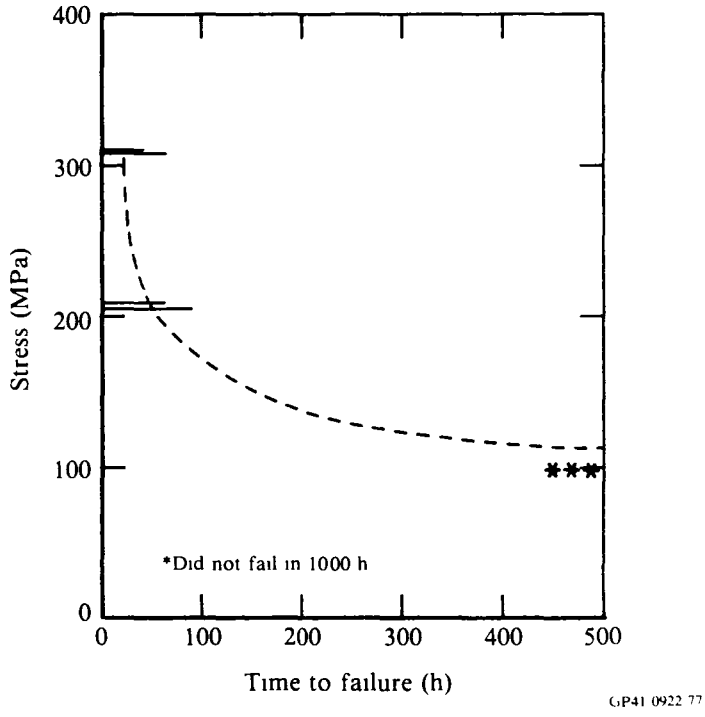

Figure 62. Time-to-failure in alternate immersion C-ring tests of Al-3Li-1.5Cu-1Mg-0 5Co-0 2Zr VA forgings: T851/530 temper, S orientation.

7. TASK 4: CORRELATION OF PROCESS/STRUCTURE/PROPERTIES RELATIONS

7.1 Effect of Particulate Type on Properties

Results presented in Figures 41, 42, 45, and 50-53 show that the additional microstructural refinement achieved by increasing the particulate solidification rate from 2000-5000 K/s (typical of VA and USGA-Ar powders) to 50 000-120 000 K/s (typical of USGA-He powders) or 400 000-500 000 K/s (typical of RQ flakes) does not improve the tensile properties of consolidated forms. The observed variations in tensile properties among VA, USGA-Ar, and USGA-He extrusions can safely be attributed to differences in Mg concentrations in the non-Li-containing alloys, and to differences in Li and Mg concentrations in the Li-containing alloy (Tables 2 and 3). Tensile properties of the Li-containing RQ extrusion fall significantly short of those of the VA extrusion, despite the larger solidification rate of the RQ flakes.

Examination of extrusion micrographs, particularly Figures 32, 33, 35, 36, 37, 38, and 40, reveals little difference in microstructure among extrusions made from different particulate types. Subgrain diameters, sizes and spacings of incoherent dispersoids, and morphologies and distributions of precipitates are similar among all extrusions and virtually identical among powder extrusions. The RQ extrusion has fewer oxide particles than the powder extrusions owing to the larger particulate size (Figures 35d and 36d), and it also has a more uniform distribution of Al_9Co_2 dispersoids (compare Figures 40a, d, e, and f). The volume fractions of oxides and dispersoids are too small to affect tensile properties, however, and the comparable ductilities of VA and RQ extrusions indicate that Al_9Co_2 dispersoids are not spaced closely enough to affect ductility.

Within the range of particulate solidification rates covered in this study, microstructures of consolidated forms are determined primarily by consolidation details such as degassing conditions, presence or absence of hot pressing, extrusion temperature, and extrusion ratio. Provided that a minimum solidification rate, which must lie below 2000 K/s, is attained, the scale of segregation of major alloying elements is sufficiently fine as to be completely relieved during consolidation processing. Further increases in solidification rate, which result in finer micro-segregation, decrease the time required for segregation to be relieved, but cannot further homogenize the soluble

alloying elements. Times and temperatures involved in conventional consolidation processing are sufficiently long that incoherent dispersoids coarsen to about the same size and spacing, regardless of the initial distribution of the dispersoid-forming elements Fe, Ni, or Co. The distribution of incoherent dispersoids is altered when the original solidification is non-dendritic, as in the case of the RQ Li-containing alloy. This change in solidification mode with increasing solidification rate promises a more uniform distribution of dispersoids and suggests that chill-block-quenched splats are superior to powders for alloys containing large volume fractions of dispersoids.

The substructure of RSP Zr-containing alloys is primarily fixed by the extrusion process, not by particulate type or solidification rate. The coherent, cubic Al_3Zr dispersoids responsible for substructure stabilization are formed during consolidation rather than during solidification, and hence their distribution is not affected by increases in the solidification rate above the threshold required to place 0.2 wt% Zr in metastable solid solution. Extrusion pole figures (Figures 26 and 27) show domination of crystallographic texture by the extrusion process and exceptional microstructural stability during subsequent solution annealing. The final substructure might be sensitive to particulate type if the substructure refining or stabilizing element were weaker in its effect, e.g., Cr or Mn.

7.2 Effect of Processing Variables on Properties

7.2.1 Processing Sequence

To obtain satisfactory properties in forms consolidated from aluminum alloy particulates, the 1.5- to 3-nm thick pre-existing oxide layers must be effectively disintegrated to allow the aluminum substrates to bond to one another during billet formation and extrusion or forging. Oxide disintegration depends on effective removal of adsorbed oxygen and water vapor during degassing and on the time, temperature, and amount of deformation during billet making and final consolidation. Although this study was not primarily directed towards examination of processing variables, some conclusions can be drawn regarding the influence of degassing practice and presence or absence of a hot pressing step on properties of consolidated forms.

The results presented in Section 5.1 indicate that the degassing cycle is much more critical for Li-containing alloy powders than for non-Li-containing alloy powders. If degassing is performed primarily at high temperatures, oxygen-bearing gases react with the powders rather than being removed, and oxide layer thicknesses can increase by as much as a factor of 9 (Figures 18b and 22b). The relatively slow degassing cycle used during production of extrusions or forgings in this study resulted in roughly comparable increases in oxygen concentrations in consolidated forms vis-a-vis loose powders in both alloys. Oxide layers in the Li-containing alloy extrusions appear to have been well disintegrated (Figure 40), and it is considered that the poor transverse tensile properties observed in Li-containing extrusions are not the result of inadequate degassing practice. Superior longitudinal and transverse ductilities at strength levels comparable to those reported in Figures 50 and 51, for example, have been reported (20,21) in RSP Al-3Li-Mg-Zr and Al-3Li-Cu-Zr extrusions which had oxygen levels comparable to those in this study. Oxygen levels $\leq$0.1% in RSP Li-containing alloy extrusions are probably acceptable, provided consolidation processing is efficient enough to disintegrate the oxide layers.

Comparison of mechanical properties strongly suggests that the consolidation processing sequence which was effective for the non-Li-containing alloys did not result in effective consolidation for the Li-containing alloy. For instance, transverse tensile properties for the Al-4.4Cu-1.5Mg-1Fe-1Ni-0.2Zr VA extrusions were only slightly lower than the longitudinal properties (Figure 43), while transverse properties of the Al-3Li-1.5Cu-1Mg-0.5Co-0.2Zr extrusions were degraded by 20% or more in strength and by 50% in ductility (Figure 51). Ductilities of Li-containing alloy forgings were much lower than those of non-Li-containing forgings (compare Figure 43 with Figure 50). Fracture toughnesses (Table 9), the variation of FCGR with ΔK (compare Figures 58 and 59 with 56 and 57), and SCC data (Figures 61 and 62) were all worse for the Li-containing than for the non-Li-containing alloy.

An alternative to adducing consolidation deficiencies to explain inadequate properties in the Li-containing alloy is to suppose that RSP Al-3Li alloys merely have intrinsically poor properties. However, recent IRAD work at MDRL on RSP Al-3Li-Zr, Al-3Li-Mg-Zr, and Al-3Li-Cu-Zr alloy extrusions has shown near-equality of longitudinal and transverse properties at a yield

stress level of 440 MPa **(21)**, and only a 10% loss of yield strength in transverse compared with longitudinal properties at a yield stress level of 510 MPa **(20)**. No failures of T-orientation SCC C-ring specimens were noted in tests lasting several months **(20)**. The extrusions were made from VA powders, and compositions were similar to that of the Li-containing alloy tested in this study. The major difference between the two materials was insertion of a vacuum hot-pressing step prior to extrusion in the MDRL IRAD alloys **(20)**, a step which was omitted in the extrusions for this study.

It is likely that more careful consolidation processing of Li-containing extrusions and forgings would improve properties, particularly notch-sensitive properties such as toughness, FCGR, and SCC resistance. In extrusions, vacuum hot pressing to 100% density polygonizes powder particles and starts the oxide disintegration process. Extrusion of a 100% dense compact produces more plastic flow in the neighborhood of interparticle boundaries than does extrusion of a 70% dense cold-pressed compact, in which densification and plastic flow must occur simultaneously. The process of disintegrating oxide layers into discrete particles, with concomitant bonding of fresh aluminum alloy surfaces, can proceed farther in the limited time available for extrusion if the starting form is a 100% dense billet. Kinetics of plastic flow and disintegration of oxides are more important in Li-containing than in non-Li-containing alloys owing to the thicker and possibly more adherent oxide layers present in the former after degassing.

In forgings, an upset of 55%, sufficient to ensure good properties in the Al-4.4Cu-1.5Mg-1Fe-1Ni-0.2Zr alloys, and larger than that successfully used for Al-Fe-Ce alloys **(2)**, was insufficient for adequate interparticle bonding in the Li-containing alloy. In this case, the alloy was hot pressed before final forging, but the Li-containing oxide layer was more resistant to disintegration. Multiaxial working is probably necessary to produce Li-containing forgings with good properties. For instance, ABC (multiaxial) forging of an RSP Al-3Li-1.5Cu-1Mg-0.5Co-0.2Zr alloy resulted in a consolidated form with properties equivalent to those of an extrusion of 20:1 extrusion ratio **(26)**.

7.2.2 Texture Effects

The difference in strength between VA extrusions and forgings is 80 to 90 MPa for both alloy compositions (Figures 43 and 50). This difference is correlated with the difference between the strong texture of the extrusions and the weak, axisymmetric texture of the forgings. Since both extrusions and forgings have a fine subgrain microstructure, the difference is primarily one of subgrain orientation rather than subgrain size. As the test temperature is raised, the subgrain boundaries cease to be effective barriers to slip, Hall-Petch and texture effects disappear, and the strength of extrusions approaches that of forgings (Figures 46 and 47). To increase the strength of forgings, the forging strain must be increased to permit development of a more marked texture. This can be accomplished by increasing the upset in a uniaxial forging, or by performing multiaxial forging.

7.3 Effect of Alloy Chemistry and Microstructure on Properties

7.3.1 Non-Li-Containing Alloys

The alloy Al-4.4Cu-1.5Mg-1Fe-1Ni-0.2Zr was designed to improve 150°C ultimate tensile strength from 405 MPa, typical of I/M 2124-Al, to 480 MPa, which would be required for density-normalized equivalence to Ti-6Al-4V, by a combination of dispersoid and substructure strengthening. Examination of strength as a function of test temperature (Figure 46) shows that the tensile strength was increased to 440 MPa at 150°C and the temperature stability of strength was improved below 180°C; however, the goal of equivalence to Ti-6Al-4V was not reached.

The yield stress increments resulting from dispersion strengthening and substructure refinement can be estimated using the Orowan and Hall-Petch relations, respectively. The Orowan bypassing shear stress in a polycrystalline aluminum alloy is given by

$$\tau = 3.39 \frac{Gb}{2\pi\overline{D}} \ell n \frac{\overline{x}}{4b} , \qquad (1)$$

where G = shear modulus of matrix, b = Burgers vector length, $\overline{D}$ = average interparticle spacing, and $\overline{x}$ = average particle diameter. For Al-4.4Cu-1.5Mg-1Fe-1Ni-0.2Zr at 150°C, G is assumed to be the same as for 2024-Al, e.g., 26.4

GPa **(22)** (corrected for temperature), and b = $a\sqrt{2}$ = 0.286 nm for Al. From Figure 37a, $\bar{x}$ = 0.46 x 10^{-6} m. The VA extrusion has 0.94 wt% Fe and 0.92 wt% Ni, equivalent to 4.4 vol% Al_9FeNi dispersoids. Assuming a cubical array of evenly spaced particles, the average interparticle spacing $\bar{D}$ is 1.04 x 10^{-6} m. Substituting these values into equation **(1)**, the calculated yield stress increment is 23.6 MPa.

The Hall-Petch strengthening is given by

$$\sigma = \sigma_o + kd^{1/2} \qquad (2)$$

where for Al, σ_o = frictional stress = 1.6 kg/$(mm)^2$, k = Hall-Petch slope = 0.22 kg/$(mm)^{3/2}$ **(27)**, and d = grain or subgrain diameter. Assuming a subgrain diameter of 2 μm in the Al-4.4Cu-1.5Mg-1Fe-1Ni-0.2Zr VA extrusion (Figure 37a), the substructure strengthening is 64 MPa at room temperature, and probably somewhat less at 150°C.

The contributions of substructure and dispersoids are not additive, particularly in the presence of an array of fine, semi-coherent θ′ precipitates, as in the T851 temper. The yield stress increment at 150°C resulting from θ′ precipitation corresponds approximately to the difference in yield stress between 2024-T351 and -T851 at that temperature, or about 90 MPa. Assuming that subgrain boundaries, dispersoids, and precipitates are all strong barriers, their overall strengthening effect as a first approximation is the square root of the sum of squares of the individual contributions, or 113 MPa. In the presence of precipitates, the additional strengthening effect of substructure and dispersoids is calculated to be about 23 MPa. The observed strengthening at 150°C is 22 MPa. At room temperature the effects of substructure and dispersoids are absent, suggesting that the precipitates are stronger barriers at 25°C than at 150°C. Differences in texture between I/M and P/M materials are not included in the above calculation.

This discussion suggests that the effect of refined substructure and dispersoids should be greater in the absence of precipitates, i.e., in the T351 (naturally aged) temper. Indeed, the yield strength of VA Al-4.4Cu-1.5Mg-1Fe-1Ni-0.2Zr-T351 is 417 MPa, compared to 324 MPa for 2024-Al. The increment here is close to the sum of the individual contributions, suggesting

that both substructure refinement and dispersoids contribute significantly to strength improvement in the T351 temper.

At temperatures above 150°C, the grain or subgrain boundaries cease to be effective barriers, and Hall-Petch and texture effects cease to contribute to strength. This effect has been observed in RSP Al-Li alloys by Sastry and O'Neal **(28)**. The relatively small effect of dispersion strengthening is offset by the lower Cu content of the RSP alloy. The overall analysis of strengthening contributions strongly suggests that the intermediate-to-high temperature properties of RSP Al alloys can be improved by dispersion strengthening only if the dispersoids are significantly finer and more closely spaced than was the case in this study. This can be accomplished by solidifying at larger rates than used here, or by selecting elemental additives to form dispersoids which coarsen at a slower rate than does Al_9FeNi.

7.3.2 Li-Containing Alloy

The microstructures of RSP Al-3Li-1.5Cu-1Mg-0.5Co-0.2Zr alloys in the solution-treated and aged conditions were generally satisfactory. The (Li+Cu+Mg) content of the alloys only slightly exceeded the solubility limit at the highest safe solution-treatment temperature of 560°C (Figure 36). Thus, few hard constituent particles were available to promote fracture and reduce ductility. Oxide layers on the particulates appeared to be well disintegrated, at least in the extrusions (for instance, Figure 40a), suggesting that oxygen levels were not excessive. The substructure was thermally stable and fine. However, the spacing and distribution of Al_9Co_2 dispersoids were not sufficient, except perhaps in the RQ extrusion, to significantly increase ductility by relieving planar slip.

In view of the favorable microstructures of the Li-containing alloy extrusions and the high strength obtained on a similar alloy in another study **(29)**, the deficiencies in properties of the Li-containing alloy are attributed to problems in consolidation processing rather than deficiencies in alloy chemistry or microstructure per se. It appears that the addition of Co to this alloy was superfluous. Also, while the addition of 1Mg to an Al-3Li-1.5Cu-0.2Zr matrix may result in a significant increase in strength, the reduction in ductility to 2 to 4% is a serious offsetting problem. If alternative solution and aging treatments of Al-Li-Cu-Mg-Zr alloys do not produce

significant ductility improvements with compensating strength reductions, reversion to Al-Li-Cu-Zr alloys may be required to optimize properties.

7.4 Effect of Heat Treatment Variables on Properties

The effect of heat treatment on properties was not studied extensively for the non-Li-containing alloys. Solution treating the Al-4.4Cu-1.5Mg-1Fe-1Ni-0.2Zr VA extrusion at 500°C rather than 530°C resulted in 20 to 40 MPa decreases in yield and ultimate tensile strengths owing to less complete solutionizing of Cu and Mg, which resulted in smaller volume fractions of θ' precipitates. As discussed in Section 7.3.1, the effect of RSP on this alloy was more pronounced in the naturally aged than in the peak-aged condition because of the larger effects of substructure refinement and dispersion strengthening when not combined with precipitation strengthening.

The strength increments in the peak-aged Li-containing extrusions caused by increasing the prior solution-treatment temperature from 530 to 560°C were 25 to 30 MPa in yield strength and 40 to 50 MPa in ultimate tensile strength, without a noticeable change in ductility. This result is also the effect of increased solutionizing of Li, Cu, and Mg. The effect of a 2% stretch between solution treating and aging is similar to that of increasing the solution-annealing temperature (Figure 53), and is the result of increased volume fraction and homogeneity of precipitation of the $T_1(Al_2CuLi)$ and similar phases **(30)**. The effects of stretch and increasing solution temperature are not additive, possibly as a result of deficiencies in consolidation processing. These two effects were found to be additive in Al-3Li-2Cu-0.2Zr, where processing had included a vacuum hot pressing step **(21)**.

7.5 Recommendations for Optimal Composition/Processing/Structure Combinations in RSP Aluminum Alloys

Based on the results of this study, the following recommendations on optimal chemistry and processing of RSP Al alloys are:

1. For Li-containing alloys intended primarily for ambient-temperature applications, choose a composition such that the combined major alloying element additions do not exceed the solubility limit at the solution-annealing temperature. The alloy should contain Zr for substructure

refinement, but dispersoid-forming element additions to promote ductility through slip dispersal are redundant in a fine-grained material.

2. For alloys intended for intermediate-to-high temperature service, dispersion strengthening is a valid mechanism for providing a temperature-insensitive strength contribution. However, the spacing of dispersoids must be smaller than the approximately 1 μm attained in this study to provide a sufficient strength increment.

3. RSP particulates should be produced by a method which is easy to apply and yields clean, easily handled particulates. The absolute solidification rate is not important for Al alloys not containing dispersoids, provided that it exceeds ~ 10^3 K/s.

4. Large amounts of hot work during the consolidation process are required to effectively disintegrate oxide layers and promote interparticle bonding. Li-containing alloys are more sensitive than non-Li-containing alloys in this respect. Vacuum hot pressing appears to be a necessary preliminary to extrusion or forging. Forgings of Li-containing alloys require more deformation to achieve a well-bonded consolidated form than forgings of non-Li-containing alloys.

5. Suitable variations of solution-treatment temperature, process stretch, and aging temperature and time can result in controlled variation of properties in RSP aluminum alloys, as in I/M alloys. The variation of properties with heat treatment depends upon the various strength contributions and may be different for RSP than for I/M alloys.

8. CONCLUSIONS

1. RSP particulates of Al-4.4Cu-1.5Mg-1Fe-1Ni-0.2Zr and Al-3Li-1.5Cu-1Mg-0.5Co-0.2Zr alloys can be produced by vacuum atomization, ultrasonic atomization in argon or helium, or twin roller-quenching at solidification rates ranging from 2×10^3 to 4×10^5 K/s.

2. Oxide layers on as-solidified particulates are 1.5- to 2-nm thick, regardless of chemistry or particulate production method.

3. Vacuum degassing of Al-4.4Cu-1.5Mg-1Fe-1Ni-0.2Zr becomes continuously more efficient as the temperature is raised. Degassing of Al-3Li-1.5Cu-1Mg-0.5Co-0.2Zr becomes less efficient above 450°C owing to chemical fixing of H and O by Li. Degassing of RSP Li-containing aluminum alloy powders should be carried out at the lowest practical temperature to assure removal rather than chemical fixing of H and O, and prevent large increases in oxide layer thickness on degassed powder particles.

4. Consolidation processing by canning, cold compaction, degassing, and hot extrusion is sufficient to yield good mechanical properties in non-Li-containing alloys. Li-containing alloys have thicker particulate oxide layers, more adherent layers, or both, and require a vacuum hot pressing step before extrusion to achieve adequate interparticle bonding and good mechanical properties.

5. Uniaxial forging of non-Li-containing alloys to 50 to 60% upset is sufficient to assure good mechanical properties. The same process is not adequate for Li-containing alloys, and larger upsets or multiaxial forging are required to produce good properties in Li-containing alloy powder forgings.

6. Differences in particulate type have little influence on properties of consolidated forms in either Al-4.4Cu-1.5Mg-1Fe-1Ni-0.2Zr or Al-3Li-1.5Cu-1Mg-0.5Co-0.2Zr extrusions or forgings. In both alloys, the final microstructures and properties are dominated by the effects of consolidation processing.

7. Deficiencies in consolidation processing of the Li-containing alloy are reflected most strongly in the transverse tensile properties and in notch-

sensitive properties such as fracture toughness, fatigue-crack-growth rate, and stress-corrosion-cracking resistance.

8. Differences in strength between extrusions and forgings are largely the result of differences in texture caused by differences in degree of hot work during consolidation. Strengths of the two product forms approach one another in testing above 150°C owing to the ineffectiveness of grain boundaries as barriers to slip at high temperatures.

9. Strength/ductility combinations in both non-Li- and Li-containing alloys are strongly affected by combinations of solution treatment, process stretch, and aging treatment variables.

10. The dispersoid-forming system Fe+Ni is readily added to an Al-4.4Cu-1.5Mg base composition by RSP, but the resulting dispersoids are too coarse and too widely spaced to contribute significantly to intermediate-temperature strength in conventionally processed consolidated forms. Alternative processing or a more effective dispersoid-forming system are required to achieve significant dispersion strengthening in this alloy system.

11. The combined effects of refined substructure and.fine, incoherent dispersoids in Al-4.4Cu-1.5Mg-1Fe-1Ni-0.2Zr-T851 raise the 150°C ultimate tensile stress relative to I/M 2124-T851 by about 10%, compared with the 20% increase in strength which would be required for density-normalized strength equivalency to Ti-6Al-4V. The effect of substructural refinement is more significant (110 MPa increase in yield strength) in the T351 temper.

12. Both substructure refinement by Zr additions, and solution or dispersion strengthening by Mg addition, contribute significantly to the strength of Al-3Li-1.5Cu-1Mg-0.5Co-0.2Zr. However, Mg additions also decrease the ductility and fracture toughness, and better strength/ductility combinations may be available from Al-3Li-Cu-Zr rather than Al-3Li-Cu-Mg-Zr alloys.

13. The addition of 0.5Co to Al-3Li-1.5Cu-1Mg-0.2Zr does not produce a sufficient volume fraction of fine, even dispersoids to provide a significant ductility increase by Orowan bypassing. Dispersoid-forming element additions to a fine-grained alloy are superfluous for ductility enhancement.

14. RSP non-Li- and Li-containing alloys are promising substitutes for commercial 2XXX and 7XXX alloys in both ambient- and elevated-temperature applications. However, further improvements in alloy chemistry and consolidation processing are required for these alloys to fully realize their potential.

9. REFERENCES

1. S. L. Langenbeck et al., Elevated Temperature Alloy Development, Interim Technical Report, Lockheed California Co., Rpt. No. LR29977, AFML Contract No. F33615-81-C-5096 (September 1981).

2. R. E. Sanders, Jr. and G. J. Hildeman, Elevated Temperature Aluminum Alloy Development, Report No. AFWAL-TR-81-4076 on Air Force Contract No. F33615-77-C-5086 (September 1981).

3. J. P. Durand, R. M. Pelloux, and N. J. Grant, Materials Science and Engineering 23, 247 (1976).

4. E. R. Slaughter and S. K. Das, Iron-Aluminum Alloys with Titanium Diboride Dispersions by Rapid Solidification, in Rapid Solidification Processing: Principles and Technologies II, R. Mehrabian, B. H. Kear, and M. Cohen, eds. (Claitor's, Baton Rouge, LA, 1980), p. 354.

5. C. Dresser, Air-to-Surface (ATS) Technology Evaluation and Integration Study, McDonnell Douglas Report MDC A49941, AFWAL-FD Contract No. F33615-76-C-3101 (January 1978).

6. R. E. Lewis, Development of Advanced Aluminum Alloys from Rapidly Solidified Powders for Aerospace Structural Applications, Lockheed Missiles and Space Co. Report LMSC-D674504, DARPA/AFML Contract No. F33615-78-C-5203 (March 1979).

7. S. M. L. Sastry, P. J. Meschter, J. E. O'Neal, and K. K. Sankaran, Microstructure and Properties of Powder-Processed Aluminum-Lithium Alloys, McDonnell Douglas Report MDC Q0778, AFOSR Contract No. F49620-79-C-0039 (May 1982).

8. K. K. Sankaran, J. E. O'Neal, and S. M. L. Sastry, Effects of Second-Phase Dispersoids on Deformation Behavior of Al-Li Alloys, Metallurgical Transactions 14A, 2174 (1983).

9. N. J. Grant, A Review of Various Atomization Processes, in Rapid Solidification Processing: Principles and Technologies, R. Mehrabian, B. H. Kear, and M. Cohen, eds. (Claitor's, Baton Rouge, LA, 1978), p. 230.

10. N. J. Grant, Rapid Solidification of Metallic Particulates, Journal of Metals 35, 20 (1983).

11. A. Lawley, An Overview of Powder Atomization Processes and Principles, The International Journal of Powder Metallurgy and Powder Technology 13, 169 (1977).

12. V. Anand, A. J. Kaufman, and N. J. Grant, Rapid Solidification of a Modified 7075 Aluminum Alloy by Ultrasonic Atomization, Report No. AD-A085141 on Office of Naval Research Contract No. N00014-78-C-0385 (March 1980).

13. N. J. Grant, S. Kang, and W. Wang, Structure and Properties of Rapidly Solidified 2000 Series Al-Li Alloys, in Aluminum-Lithium Alloys, T. H. Sanders, Jr. and E. A. Starke, Jr., eds. (TMS-AIME, Warrendale, PA, 1981), p. 171.

14. K. K. Sankaran, S. M. L. Sastry, and J. E. O'Neal, Microstructure and Deformation of Rapidly Solidified Al-3Li Alloys Containing Incoherent Dispersoids, in Aluminum-Lithium Alloys, T. H. Sanders, Jr. and E. A. Starke, Jr., eds. (TMS-AIME, Warrendale, PA, 1981), p. 189.

15. D. P. Ames, R. R. Irani, and C. F. Callis, The Agreement Between Independent Methods for Particle Size Distribution Measurements on Finely Divided Powders Including Phosphates, Journal of Physical Chemistry 63, 531 (1959).

16. R. R. Irani and C. F. Callis, Accurate Particle Size Distribution with Electroformed Sieves, Analytical Chemistry 31, 2026 (1959).

17. L. F. Mondolfo, Aluminum Alloys: Structure and Properties (Butterworths, Boston, 1976).

18. M. W. Mahoney and C. H. Hamilton, Superplastic Aluminum Evaluation, Report No. AFWAL-TR-81-3051 (AD-A107760) on Air Force Contract No. F33615-79-C-3218 (June 1981).

19. H. Matyja, B. C. Giessen, and N. J. Grant, Effect of the Cooling Rate on the Dendrite Spacing in Splatcooled Aluminum Alloys, Journal of the Institute of Metals 96, 30 (1968).

20. MDRL Independent Research and Development, Report No. MDC Q0871-4, 15 March 1984 (proprietary).

21. P. M. Meschter, P. S. Pao, R. J. Lederich, and J. E. O'Neal, Effect of Compositional Variations on the Microstructures and Properties of Rapidly Solidified Al-3Li Alloys, in Proceedings ASTM Symposium on Rapidly Solidified Powder Aluminum Alloys (ASTM STP in press).

22. ASM Metals Handbook, 8th Edition, Volume 7: Atlas of Microstructures of Industrial Alloys (American Society for Metals, Metals Park, OH, 1972), p. 241.

23. P. S. Pao, K. K. Sankaran, and J. E. O'Neal, Microstructure, Deformation, and Corrosion-Fatigue Behavior of a Rapidly Solidified Al-Li-Cu-Mn Alloy, in Aluminum-Lithium Alloys, T. H. Sanders, Jr. and E. A. Starke, Jr., eds. (TMS-AIME, Warrendale, PA, 1981), p. 307.

24. D. Voss, Correlation of Processing Parameters, Microstructure, and Mechanical Properties of High-Strength Powder Metallurgically Produced Aluminum Alloys, Report No. DFVLR-FB 79-34, Deutsche Forschungs- und Versuchsanstalt fuer Luft- und Raumfahrt, Cologne (1979).

25. R. P. Wei and P. S. Pao, Mechanisms of Corrosion Fatigue in High-Strength I/M and P/M Aluminum Alloys, Technical Report No. 2 on Air Force Office of Scientific Research Contract No. F49620-81-K-0004 (February 1983).

26. I. G. Palmer, R. E. Lewis, and D. D. Crooks, The Design and Mechanical Properties of Rapidly Solidified Al-Li-X Alloys, in Aluminum-Lithium Alloys, T. H. Sanders, Jr. and E. A. Starke, Jr., eds. (TMS-AIME, Warrendale, PA), p. 241.

27. J. D. Embury, Strengthening by Dislocation Substructures, in Strengthening Mechanisms in Crystals, A. Kelley and R. B. Nicholson, eds. (Applied Science Publishers, London, 1971), p. 342.

28. S. M. L. Sastry and J. E. O'Neal, High-Temperature Deformation Behavior and Mechanical Properties of Rapidly Solidified Al-Li-Co and Al-Li-Zr Alloys, in Aluminum-Lithium Alloys II, T. H. Sanders, Jr. and E. A. Starke, Jr., eds. (TMS-AIME, Warrendale, PA, 1984), p. 79.

29. I. G. Palmer, R. E. Lewis, D. D. Crooks, E. A. Starke, Jr. and R. E. Crooks, Effect of Processing Variables on Microstructure and Properties of Two Al-Li-Cu-Mg-Zr Alloys, in Aluminum-Lithium Alloys II, T. H. Sanders, Jr. and E. A. Starke, Jr., eds. (TMS-AIME, Warrendale, PA, 1984), p. 91.

30. E. A. Starke, Jr., T. H. Sanders, Jr., and I. G. Palmer, New Approaches to Alloy Development in the Al-Li System, Journal of Metals 33(8), 24 (1981).

Standard Bibliographic Page

1 Report No	2 Government Accession No	3 Recipient's Catalog No
NASA CR-177946		

4 Title and Subtitle	5 Report Date
Study on Effects of Powder and Flake Chemistry and Morphology on the Properties of Al-Cu-Mg-X-X-X Powder Metallurgy Advanced Aluminum Alloys	November 1985
	6 Performing Organization Code
7 Author(s)	8 Performing Organization Report No
P. J. Meschter, R. J. Lederich, J. E. O'Neal and P. S. Pao	MDC 01227
9 Performing Organization Name and Address	10 Work Unit No
McDonnell Douglas Research Laboratories P.O. Box 516 St. Louis, MO 63166	11 Contract or Grant No NAS1-17107
12 Sponsoring Agency Name and Address	13 Type of Report and Period Covered
National Aeronautics and Space Administration Langley Research Center Hampton, VA 23665	Contractor Report
	14 Sponsoring Agency Code

15 Supplementary Notes

Langley Technical Monitor: W. Barry Lisagor

Final Report

16 Abstract

A study was conducted to determine the effects of alloy chemistry and particulate morphology on consolidation behavior and consolidated product properties in rapid solidification processed, powder-metallurgical Al-3Li-1.5Cu-1Mg-0.5Co-0.2Zr and Al-4.4Cu-1.5Mg-Fe-Ni-0.2Zr extrusions and forgings. Microstructures and mechanical properties of both alloys were largely unaffected by particulate production method (vacuum atomization, ultrasonic atomization, or twin-roller quenching) and by particulate solidification rates between 10^3 and 10^5 K/s. Consolidation processing by canning, cold compaction, degassing, and hot extrusion was sufficient to yield mechanical properties in the non-Li-containing alloy extrusions which were similar to those of 7075-Al, but ductilities and fracture toughnesses were inferior owing to poor interparticle bonding caused by lack of a vacuum-hot-pressing step during consolidation. Mechanical properties of extrusions were superior to those of forgings owing to the stronger textures produced by the more severe hot working during extrusion. The effects on mechanical properties of dispersoid size and volume fraction, substructural refinement, solid solution strengthening by Mg, and precipitate size and distribution were elucidated for both alloy types. RSP non-Li- and Li-containing alloys were found to be promising substitutes for commercial 2XXX and 7XXX alloys in both ambient-temperature and elevated-temperature applications. Further improvements in alloy chemistry and consolidation processing were recommended for the RSP alloys to fully realize their potential.

17 Key Words (Suggested by Authors(s))	18 Distribution Statement
Rapid solidification Aluminum-lithium alloys Consolidation Powder metallurgy Extrusion	Unclassified - Unlimited

19 Security Classif (of this report)	20 Security Classif (of this page)	21 No of Pages	22 Price
Unclassified	Unclassified	105	

For sale by the National Technical Information Service, Springfield, Virginia 22161

NASA Langley Form 63 (June 1985)

End of Document